

VRIJE UNIVERSITEIT

Hypervalence and Aromaticity

ACADEMISCH PROEFSCHRIFT

ter verkrijging van de graad Doctor aan
de Vrije Universiteit Amsterdam,
op gezag van de rector magnificus
prof.dr. L.M. Bouter,
in het openbaar te verdedigen
ten overstaan van de promotiecommissie
van de faculteit der Exacte Wetenschappen
op maandag 2 juni 2008 om 10.45 uur
in de aula van de universiteit,
De Boelelaan 1105

door

Simon Christian André Henri Pierrefixe

geboren te Vannes, Frankrijk

promotor: prof.dr. E. J. Baerends
copromotor: dr. F. M. Bickelhaupt

Hypervalence & Aromaticity

Simon C. A. H. PIERREFIXE

Cover designed by wrinkly pea: www.wrinklypea.com

ISBN: 978-90-8891-0432

Contents

1 General Introduction	1
1.1 Hypervalence	2
1.2 Aromaticity	3
2 Theory and Methods	7
2.1 The Schrödinger equation	7
2.2 Electronic-structure calculations	8
2.3 Density functional theory	9
2.4 Kohn-Sham Molecular Orbital model	10
Part I HYPERVALENCE	13
3 Hypervalence and the Delocalizing <i>versus</i> Localizing Propensities of H_3^-, Li_3^-, CH_5^- and SiH_5^-	15
3.1 Introduction	16
3.2 Theoretical Methods	18
3.3 Results and Discussions	19
3.4 Conclusions	25
4 Hypervalent Silicon <i>versus</i> Carbon: Ball-in-a-Box Model	27
4.1 Introduction	28
4.2 Theoretical Methods	31
4.3 Results and Discussions	31
4.4 Conclusions	44

5 Hypervalent <i>versus</i> Nonhypervalent Carbon in Noble-Gas Complexes	47
5.1 Introduction	48
5.2 Theoretical Methods	49
5.3 Results and Discussions	51
5.4 Conclusions	64
Part II AROMATICITY	67
6 Aromaticity. Molecular Orbital Picture of an Intuitive Concept	69
6.1 Introduction	70
6.2 Theoretical Methods	72
6.3 Results and Discussions	74
6.4 Conclusions	81
7 Aromaticity and Antiaromaticity in 4-, 6-, 8- and 10-Membered Conjugated Hydrocarbon Rings	83
7.1 Introduction	84
7.2 Theoretical Methods	86
7.3 Results and Discussions	88
7.4 Conclusions	94
8 Aromaticity in Heterocyclic and Inorganic Benzene Analogs	97
8.1 Introduction	98
8.2 Theoretical Methods	99
8.3 Results and Discussions	101
8.4 Conclusions	108
9 Summary	111
10 Samenvatting	117
Acknowledgements / Dankwoord / Remerciements	122
List of Publications	124

1 General Introduction

Chemistry is substances and their transformations.^[1] Originally chemistry was an experimental science but chemists have always proposed and developed theoretical models and concepts to account for their observations and ease the spreading of new ideas. Nowadays these models can be further tested by theoretical chemistry, thanks to the development of quantum mechanics and of computing power along the twentieth century. Hypervalence and aromaticity are two such concepts of fundamental importance within chemistry.^[2-4] Consequently numerous hypervalent and aromatic systems have been intensively studied, experimentally and theoretically, over the decades.^[5-7] But despite many contributions on these issues, the definitions of the concepts themselves are still the subject of discussion.^[8-9]

This thesis will not focus on these discussions but we rather wish to tackle hypervalence and aromaticity from a different perspective. Both concepts deal with the propensity of chemical systems to delocalize or localize bonds. More precisely, hypervalent and aromatic molecules usually present highly symmetrical structures with equal bonds while the geometries of non-hypervalent and antiaromatic species are asymmetric with alternating short and long bonds. The main purpose of this thesis is to gain more insight into the origin of the choice of nature between delocalized structures with equal bonds and localized structures with short and long bonds for some well-known (non)hypervalent and (anti)aromatic systems.

We want to obtain these insights from electronic structure theory by developing simple qualitative models based on Molecular Orbital (MO) theory. MO theory is a powerful tool to understand and interpret chemistry and has indeed proved over the years to be successful in clarifying chemistry in general.^[10-11] The MO models developed in this thesis are supported by accurate calculations obtained within the Density Functional Theory (DFT) framework. The establishment of DFT in the recent decades as an alternative to conventional *ab initio*

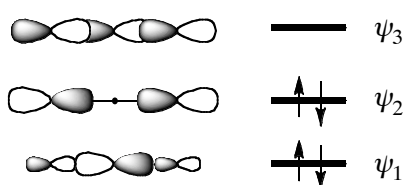
(wavefunction based) calculations is one of the most important steps in theoretical chemistry since the development of quantum mechanics and the progress made in computing possibilities.^[12] A brief overview of the theoretical background and of the methods used in this thesis will be given in the Chapter 2. The thesis will be further separated into two parts dedicated to hypervalence and aromaticity, respectively.

1.1 Hypervalence

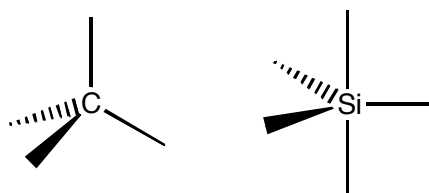
Part 1 of this thesis deals with the concept of hypervalence. Ever since Lewis published his seminal paper that paved the way for the octet rule in 1916, hypervalence has been a challenging notion in chemistry.^[13] Since hypervalent molecules do not seem to follow the octet rule, different models have been proposed to account for their bonding mechanisms. Based on the fact that, at the time, most hypervalent molecules involve third-row atoms like silicon, phosphorus or sulfur as central atoms, Pauling suggested that the hypervalence of maingroup atoms derives from the availability of low-energy *d* Atomic Orbitals (AOs): the valence shell of the central atom can be expanded to *d* orbitals and the bonding in these molecules is then explained by using hybrid orbitals composed of *s*, *p* and *d* AOs.^[6] But this model has been dismissed by recent calculations showing that the central atom in hypervalent species predominantly invokes its *s* and *p* AOs for bonding and that the *d* AOs merely act as corrective polarization functions but not as valence orbitals.^[14]

Alternatively, Pimentel and Rundle proposed simultaneously in 1951 a qualitative MO model to account for the hypervalency of the central atom in species such as F_3^- and XeF_2 : the 3-center-4-electron (3c-4e) bond model.^[15] Originally, the 3c-4e bond was formulated in terms of the valence p_{σ} AOs of a linear arrangement of three atoms that yields a well-known pattern of three MOs: ψ_1 , ψ_2 and ψ_3 , shown in Scheme 1.1. These MOs are bonding, nonbonding and antibonding, respectively, with four electrons occupying together ψ_1 and ψ_2 .^[10,16] Although the 3c-4e model is widely accepted as a good description of the bonding in hypervalent species, it does not explain *why* such a bonding mechanism leads to stable hypervalent species in some cases and to transition states in others.^[14d,17] On the other hand, qualitative explanations on the relative stability of archetypal hypervalent systems were provided by recent valence bond (VB) studies conducted by Shaik, Hiberty and coworkers as will be pointed out in Chapters 3-4.^[18]

Scheme 1.1 MOs involved in 3c-4e bonding



In this part of this thesis, we will address the hypervalency of some well studied systems with MO theory in order to catch up with VB theory regarding the treatment and understanding of why certain atoms can form stable hypervalent molecules and others cannot. For example, carbon, as illustrated below, bind usually not more than four ligands^[3,4] while silicon, despite being isoelectronic, can bind five or even more substituents.^[5] The results of our investigations are presented in the Chapters 3 to 5.

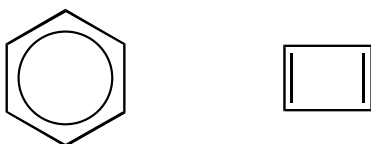


In Chapter 3, we studied the localizing versus delocalizing propensities of H_3^- , Li_3^- , CH_5^- and SiH_5^- with a focus on the different bonding capabilities of the central atom in these species. Lithium and silicon have indeed the capability to form hypervalent structures, such as Li_3^- and SiH_5^- , which is contrasted by the absence of this capability of hydrogen and carbon, as exemplified by H_3^- and CH_5^- . These findings obtained are further elaborated upon in Chapter 4 where the “Ball-in-a-box” model is unveiled. This model accounts for the nonhypervalency of carbon in ClCH_3Cl^- compared to the hypervalency of silicon in the isoelectronic $\text{ClSiH}_3\text{Cl}^-$. In Chapter 5, we studied the noble-gas complexes Ng_nCH_3^+ ($n = 1$ and 2 and $\text{Ng} = \text{He}, \text{Ne}, \text{Ar}, \text{Kr}, \text{Xe}, \text{Rn}$) with a focus on the relative stability of $\text{Ng}-\text{CH}_3-\text{Ng}^+$. In fact, the symmetric pentacoordinated $\text{Ng}-\text{CH}_3-\text{Ng}^+$ is a stable complex for $\text{Ng} = \text{He}$ and Ne while it is a transition state for $\text{Ar}, \text{Kr}, \text{Xe}$ and Rn .

1.2 Aromaticity

Part 2 of this thesis deals with the intuitive, maybe somewhat vague yet powerful concept of aromaticity. This concept has consequently aroused the interest of generations of chemists and physicists and it remains the subject of many experimental and theoretical studies associated with its relevance in chemistry, biology and technology.^[3,4,7] Despite many studies, the physical nature of aromaticity is still not completely understood and the concept itself continues to be the topic of many studies.^[7,9] However, the primary indicators of aromaticity are: (i) a regular geometry with delocalized bonds, (ii) an enhanced thermodynamic stability and (iii) a kinetic inertness. In contrast, antiaromatic compounds are highly reactive species that present irregular geometries with localized bonds.^[7,19] Others properties have been proposed as symptoms of aromatic character like for example the downfield shift in proton NMR spectra but they are secondary symptoms that are somehow still vague. Benzene and its cyclic delocalized structure is the archetypal example of aromaticity and has consequently been the subject of many studies since its synthesis by Faraday.^[20] On the other hand,

cyclobutadiene with its distorted geometry showing localized double bonds is the antiaromatic counterpart of benzene.



The regular hexagon shape of benzene with alternating single and double C–C bonds was initially proposed by Kekulé in 1865.^[21] In the early 20th century, Pauling and Hückel were the first to quantum chemically address the issue of benzene's structure and enhanced stability by using VB and MO theory.^[6,22,23] In a VB-type approach, used by both Pauling and Hückel, the circular topology of benzene enables a resonance between the wavefunctions of two complementary sets of localized bonds, leading to an additional stabilization. In parallel, Hückel applied an MO approach to benzene and other planar conjugated hydrocarbons during the 1930s. This approach that would be later called the Hückel Molecular Orbital (HMO) theory, is the basis for the Hückel rules.^[4] The enhanced stability of benzene relative, for example, to isolated or linearly conjugated double bonds, is attributed to an extra bonding contact (or resonance integral or interaction matrix element) in circularly conjugated hydrocarbons with $4n+2 \pi$ electrons.^[23] The π -electron system was therefore originally considered to be the driving force for delocalization in circularly conjugated $4n+2 \pi$ -electron species and for localization in circularly conjugated $4n \pi$ -electron systems ($n = 1$ for benzene and cyclobutadiene).^[4]

On the other hand, the idea that benzene's D_{6h} symmetric structure originates from a delocalizing propensity of its π -electron system has been challenged as soon as the late 1950s and early 1960s.^[24] This led to the somewhat contradictory notion, nicely sketched by Kutzelnigg,^[25] that, on one hand, benzene's regular, delocalized structure is only possible due to the π electron's capability to form delocalized bonds and, on the other hand, the very same π electrons do favor a structure with localized double bonds. The distortive propensity of the π electrons has been confirmed in various studies during the last two decades.^[26]

Shaik, Hiberty, and co-workers showed,^[27] in terms of an elegant VB model, that it is the σ system that enforces the delocalized, D_{6h} symmetric structure of benzene upon the π system, which intrinsically strives for localized double bonds. These conclusions initiated a debate,^[28] but were eventually reconfirmed by others.^[29] One factor that promoted a controversy is that, whereas in VB theory there is a clear model to explain why, for example, in benzene σ delocalization overrules π localization, such a clear model is missing in MO theory.

In order to fill the gap in the MO treatment of this issue, we will address in this part of the thesis the bond delocalization problem in some planar organic and inorganic molecules with MO theory. In Chapter 6, we will develop a simple MO model that explains why benzene shows delocalized double bonds whereas 1,3-cyclobutadiene features localized

double bonds. In Chapter 7, this model will be further extended to planar cyclooctatetraene (C_8H_8) and cyclodecapentaene ($C_{10}H_{10}$). Finally in Chapter 8, we will compare the (de)localization mechanisms in benzene and in various heterocyclic and inorganic benzene analogs.

References

- [1] R. Hoffmann, *The tense middle* **2006**, Essay (<http://thisibelieve.org/>).
- [2] R. J. Gillespie, P. L. A. Popelier, *Chemical Bonding and Molecular Geometry: From Lewis to Electron Densities*; Oxford University Press, New York, **2001**.
- [3] M. B. Smith, J. March, *Advanced Organic Chemistry: Reactions, Mechanisms and Structure*; Wiley-Interscience, New York, **2001**.
- [4] F. A. Carey, R. J. Sundberg, *Advanced Organic Chemistry: Structure And Mechanisms (Part A)*; Springer, New York, **2000**.
- [5] K. Y. Akiba, *Chemistry of Hypervalent Compounds*; Wiley-VCH, New York, **1998**.
- [6] L. Pauling, *The Nature of the Chemical Bond*; 3rd ed., Cornell University Press: Ithaca, New York, **1960**.
- [7] (a) P. J. Garratt, *Aromaticity*, John Wiley & Sons Inc, New York, **1986**; (b) V. I. Minkin, M. N. Glukhotsev, B. Y. Simkin, *Aromaticity and Antiaromaticity: Electronic and Structural Aspects*; John Wiley & Sons Inc, New York, **1994**.
- [8] (a) S. Noury, B. Silvi, R. J. Gillespie, *Inorg. Chem.* **2002**, *41*, 2164; (b) R. J. Gillespie, E. A. Robinson, *Inorg. Chem.* **1995**, *34*, 978; (c) J. Cioslowski, S. T. Mixon, *Inorg. Chem.* **1993**, *32*, 3209.
- [9] (a) P. v. R. Schleyer, H. J. Jiao, *Pure Appl. Chem.* **1996**, *68*, 209; (b) P. v. R. Schleyer, *Chem. Rev.* **2001**, *101*, 1115; (c) M. K. Cyranski, T. M. Krygowski, A. R. Katritzky, P. v. R. Schleyer, *J. Org. Chem.* **2002**, *67*, 1333.
- [10] T. A. Albright, J. K. Burdett, M.-H. Whangbo, *Orbital Interactions in Chemistry*; John Wiley & Sons Inc, New-York, **1985**.
- [11] R. Hoffmann, *Angew. Chem. Int. Ed. Engl.* **1982**, *21*, 711.
- [12] W. Koch, M. C. Holthausen, *A Chemist's Guide to Density Functional Theory*; Wiley-VCH, Weinheim **2001**.
- [13] G. N. Lewis, *J. Am. Chem. Soc.* **1916**, *38*, 762.
- [14] (a) F. M. Bickelhaupt, M. Sola, P. v. R. Schleyer, *J. Comput. Chem.* **1995**, *16*, 465; (b) A. E. Reed, P. v. R. Schleyer, *J. Am. Chem. Soc.* **1990**, *112*, 1434; (c) E. Magnusson, *J. Am. Chem. Soc.* **1990**, *112*, 7940; (d) W. Kutzelnigg, *Angew. Chem. Int. Ed. Engl.* **1984**, *23*, 272.
- [15] (a) G. C. Pimentel, *J. Chem. Phys.* **1951**, *19*, 446; (b) R. J. Hach, R. E. Rundle, *J. Am. Chem. Soc.* **1951**, *73*, 4321.
- [16] (a) G. A. Landrum, N. Goldberg, R. Hoffmann, *J. Chem. Soc., Dalton Trans.* **1997**, 3605; (b) C. A. Ramsden, *Chem. Soc. Rev.* **1994**, *23*, 111.
- [17] B. Braida, P. C. Hiberty, *J. Am. Chem. Soc.* **2004**, *126*, 14890.
- [18] (a) S. Shaik, A. Shurki, *Angew. Chem. Int. Ed. Engl.* **1999**, *38*, 587; (b) P. C. Hiberty, *J. Mol. Struct. (THEOCHEM)* **1998**, *451*, 237; (c) G. Sini, G. Ohanessian, P. C. Hiberty, S. S.; Shaik, *J. Am. Chem. Soc.* **1990**, *112*, 1407; (d) G. Sini, P. C. Hiberty, S. S.; Shaik, S. S. *J. Chem. Soc, Chem. Comm.* **1989**, 772.
- [19] R. Breslow, *Acc. Chem. Res.* **1973**, *6*, 393.
- [20] M. Faraday, *Phil. Trans. R. Soc. London* **1825**, 440.
- [21] A. Kekulé, *Bull. Soc. Chim. Paris* **1865**, *3*, 98.

- [22] L. Pauling, *J. Am. Chem. Soc.* **1926**, *48*, 1132.
- [23] E. Hückel, *Z. Phys.* **1931**, *70*, 204.
- [24] (a) Y. Ooshika, *J. Phys. Soc. Japan* **1957**, *12*, 1238; (b) H. Labhart, *J. Chem. Phys.* **1957**, *27*, 947; (c) H. C. Longuet-Higgins, L. Salem, *Proc. R. Soc. London, A* **1959**, *251*, 172; (d) M. Tsui, S. Huzinaga, T. Hasino, *Rev. Mod. Phys.* **1960**, *32*, 425; (e) R. S. Berry, *J. Chem. Phys.* **1961**, *35*, 2253.
- [25] W. Kutzelnigg, *Einführung in die Theoretische Chemie, Band 2, Die chemische Bindung*, Verlag Chemie, Weinheim, **1978**, Section 11.11.
- [26] (a) Y. Haas, S. Zilberg, *J. Am. Chem. Soc.* **1995**, *117*, 5387; (b) E. Heilbronner, *J. Chem. Educ.* **1989**, *66*, 471; (c) A. Stanger, K. P. C. Vollhardt, *J. Org. Chem.* **1988**, *53*, 4889; (d) N. D. Epiotis, *Pure Appl. Chem.* **1983**, *55*, 229.
- [27] (a) P. C. Hiberty, S. S. Shaik, J. M. Lefour, G. Ohanessian, *J. Org. Chem.* **1985**, *50*, 4657; (b) S. S. Shaik, P. C. Hiberty, *J. Am. Chem. Soc.* **1985**, *107*, 3089; (c) P. C. Hiberty, S. S. Shaik, G. Ohanessian, J. M. Lefour, *J. Org. Chem.* **1986**, *51*, 3908; (d) S. S. Shaik, P. C. Hiberty, J. M. Lefour, G. Ohanessian, *J. Am. Chem. Soc.* **1987**, *109*, 363; (e) S. S. Shaik, P. C. Hiberty, G. Ohanessian, J. M. Lefour, *J. Phys. Chem.* **1988**, *92*, 5086; (f) P. C. Hiberty, D. Danovich, A. Shurki, S. Shaik, *J. Am. Chem. Soc.* **1995**, *117*, 7760; (g) A. Shurki, S. Shaik, *Angew. Chem. Int. Ed. Engl.* **1997**, *36*, 2205; (h) S. Shaik, A. Shurki, D. Danovich, P. C. Hiberty, *Chem. Rev.* **2001**, *101*, 1501.
- [28] (a) N. C. Baird, *J. Org. Chem.* **1986**, *51*, 3907; (b) E. D. Glendening, R. Faust, A. Streitwieser, K. P. C. Vollhardt, F. Weinhold, *J. Am. Chem. Soc.* **1993**, *115*, 10952.
- [29] (a) K. Jug, A. M. Koster, *J. Am. Chem. Soc.* **1990**, *112*, 6772; (b) A. Gobbi, Y. Yamaguchi, G. Frenking, H. F. Schaefer III, *Chem. Phys. Lett.* **1995**, *244*, 27; (c) A. Rehaman, A. Datta, S. S. Mallajosyula, S. K. Pati, *J. Chem. Theory Comput.* **2006**, *2*, 30.

2 Theory and Methods

In this chapter, the theoretical background used in this thesis is discussed. First, the theoretical basis of quantum chemistry and the development of wavefunction-based calculations will be examined. Then an introduction to Density Functional Theory (DFT) will be given followed by explanations on the Molecular Orbital (MO) model contained in Kohn-Sham DFT. The purpose of this chapter is to give a brief overview of theoretical concepts used in this thesis rather than a detailed and complete description. For more details, the reader is advised to consult the various textbooks and reviews referred to in this section.

2.1 The Schrödinger equation

The purpose of theoretical chemistry is to solve the Schrödinger equation for chemically relevant systems:^[1-5]

$$H\Psi = i\hbar \partial\Psi/\partial t \quad (2.1)$$

In this equation, Ψ is the wavefunction and H is a differential operator representing the energy called the Hamilton operator. Since the state of a system is fully described by the wavefunction Ψ , solving this equation leads to information about all the molecular properties of the system. If the Hamilton operator does not depend on time, as is the case in the investigations described in this thesis, Eq. 2.1 reduces to the time-independent Schrödinger equation:

$$H\Psi = E\Psi \quad (2.2)$$

2 Theory and Methods

For a general system, the Hamilton operator contains kinetic (T) and potential (V) energy for all particles (nuclei N and electrons e):

$$H = T + V = T_e + T_N + V_{eN} + V_{ee} + V_{NN} \quad (2.3)$$

Since nuclei are much heavier than electrons, their velocities are much smaller and consequently the movement of the particles of one kind can be described independently of the movement of the other (Born-Oppenheimer approximation). The Schrödinger equation is accordingly split up into an electronic and a nuclear part. The nuclei are considered fixed and only the electronic part is actually solved. Thus, the Hamiltonian given in Eq. 2.3 reduces to the so-called electronic Hamiltonian:

$$H_{\text{elec}} = T + V_{eN} + V_{ee} \quad (2.4)$$

The solution of the Schrödinger equation with the electronic Hamiltonian is then the electronic wave function Ψ_{elec} and the electronic energy E_{elec} :

$$H_{\text{elec}} \Psi_{\text{elec}} = E_{\text{elec}} \Psi_{\text{elec}} \quad (2.5)$$

The total energy E_{tot} is then the sum of E_{elec} and the constant nuclear term E_{nuc} .

2.2 Electronic-structure calculations

Approaches aimed at solving the electronic Schrödinger equation are broadly referred to as electronic-structure or *ab initio* methods.^[1-5] However the electronic Schrödinger equation can exactly be solved only for one-electron systems. Therefore, more approximations are required for other, more complex systems. This is usually done by approximating the N-electron wave functions by an antisymmetrized product of N one-electrons wave function that is referred to as a Slater determinant, Φ_{SD} . The one-electron functions are called spin orbitals, and are composed of a spatial orbital and one of the two spin functions (α or β). The Hartree-Fock approximation, which is the corner stone of almost all wave function based quantum chemical methods, makes the assumption that the electronic wave function Ψ_{elec} consists of only one single Slater determinant. This implies that Coulomb correlation between electrons is neglected or, equivalently, the electron-electron repulsion is only included as an average effect. The variational principle is then used in order to find the Slater determinant that yields the lowest energy by varying the spin orbitals. The HF energy is then obtained by solving iteratively the resulting pseudo-eigenvalue problem by a technique designated self-consistent field (SCF) procedure.

The Hartree-Fock solution accounts for roughly 99% of the total energy. Yet, unfortunately, the remaining error of 1% constitutes a real problem because chemically

relevant energy changes are typically of this order of magnitude. The difference between the solution to the electronic Schrödinger equation and the Hartree-Fock (HF) energy is called the correlation energy. Most electron correlation methods use the HF wave function as a starting point for improvements. For example, the Configuration Interactions (CI) method uses a multi-determinant wave function by including excited states to the reference HF ground-state wave function. Perturbation theory provides an alternative approach to finding the correlation energy. Based on the early work of Møller and Plesset,^[6] this method uses the difference between the Hartree-Fock Hamiltonian and the exact non-relativistic Hamiltonian as the perturbation. The first-order energy is the Hartree-Fock energy and electron correlation is included at second-order or higher. Second- and fourth-order perturbations correspond to the MP2 and MP4 methods respectively. Last but not least, the coupled cluster (CC) method is a popular method that is often used for benchmarking purposes because it gives highly accurate results. This method corresponds to a nonlinear exponential parametrization of the HF wavefunction by the cluster operator that contains the single and double excitation operators as well as all higher-order operators. In practice, a hierarchy of CC wavefunctions is obtained by truncating the cluster operator at different excitations levels. In the popular CCSD(T) method, for example, the CCSD equations, for which all higher excitations than single and double are omitted from the cluster operator, are first solved and then a perturbation (T) is applied in order to approximate the effect of triple excitations. In this thesis, some of these methods (MP2, MP4, CCSD(T)) were used to benchmark some of our density functional theory studies in order to choose the best functional associated with the system studied. Heavy atoms subject to relativistic effects that were involved in some *ab initio* calculations were treated with relativistic effective core potentials.

2.3 Density functional theory

A popular alternative to the wavefunction-based methods is density functional theory (DFT).^[3-5] Hohenberg and Kohn provided the exact foundation for DFT in 1964 by proving the existence of a one-to-one correspondence between the electron density of a system and its wavefunction and, thus, its energy.^[7] The energy is a functional of the density, *i.e.* $E = E[\rho]$, and the density can then be used instead of the many-electron wave function. This idea allows a great reduction of the number of variables: for example, a wave function for an N-electron system contains $3N$ coordinates ($4N$ if the spin coordinate is taken into account explicitly) while the density depends only on three coordinates. However, the functional connecting the density and the ground-state energy is not given by the Hohenberg-Kohn theorem and approximations have to be made.

In 1965, Kohn and Sham showed that there exists a system of non-interacting electrons moving in an effective potential which produces the same density as in the real interacting

2 Theory and Methods

system.^[8] With this approach, the non-interacting electrons have one-electron wavefunctions (MOs) and the density is written in terms of a set of such auxiliary one-electron orbitals. By doing this, they introduced an orbital model into DFT. The exact energy functional is further expressed as:

$$E[\rho] = T_s[\rho] + J[\rho] + E_{Ne}[\rho] + E_{XC}[\rho] \quad (2.6)$$

In this expression, T_s is the kinetic energy of the system of non-interacting electrons, J is the classical Coulomb interaction and E_{Ne} is the nuclear attraction term. The big unknown here is the last term E_{XC} that accounts for exchange and Coulomb correlation energy. This term also includes the difference between the kinetic energy of the system of interacting electrons and that of the non-interacting electrons. The exact formulation of the exchange and correlation (XC) functional is not known and therefore it has to be approximated.

Over the years, many XC functionals have been developed for different purposes. One of the first applied XC functionals, the Local Density Approximation (LDA), depends only on the electron density. Improvements appeared with the Generalized Gradient Approximation (GGA) that depends not only on the electron density, but also on the derivatives of the density.

In this thesis, most of the calculations have been carried out with DFT using the GGA functionals BP86 and OLYP that are implemented in the Amsterdam Density Functional (ADF) program package developed by Baerends and others.^[9] BP86 consists of the exchange part proposed by Becke in 1988 and the correlation part presented by Perdew in 1986.^[10] OLYP is composed by the OPTX exchange correction proposed by Handy and the Lee-Yang-Parr correlation correction.^[11] For species containing heavy atoms, relativistic effects were treated using the zeroth-order regular approximation (ZORA).^[12]

2.4 Kohn-Sham Molecular Orbital model

As mentioned in the previous section, an important aspect of Kohn-Sham DFT is its status as a physically meaningful one-electron or MO model.^[13] The Kohn-Sham framework not only offers a road to accurate computation and prediction, but also allows interpretation and understanding of chemical bonding phenomena using familiar physical concepts from MO theory. The various features in the bonding mechanism can furthermore be quantified using an energy decomposition analysis of the bond energy. In this analysis, the total binding energy ΔE associated with forming the overall molecular species of interest, say AB, from two (or sometimes more) radical or closed-shell fragments, A' + B', is made up of two major components:

$$\Delta E = \Delta E_{\text{prep}} + \Delta E_{\text{int}} \quad (2.7)$$

In this formula, the preparation energy ΔE_{prep} is the amount of energy required to deform the individual (isolated) fragments from their equilibrium structure (A' , B') to the geometry that they acquire in the overall molecule (A , B). The interaction energy ΔE_{int} corresponds to the actual energy change when these geometrically deformed fragments A and B are combined to form the combined molecular species AB . It is analyzed using a quantitative decomposition of the bond into electrostatic interaction, Pauli repulsion (or exchange repulsion or overlap repulsion), and (attractive) orbital interactions illustrated in the Figure 2.1.

$$\Delta E_{\text{int}} = \Delta V_{\text{elstat}} + \Delta E_{\text{Pauli}} + \Delta E_{\text{oi}} \quad (2.8)$$

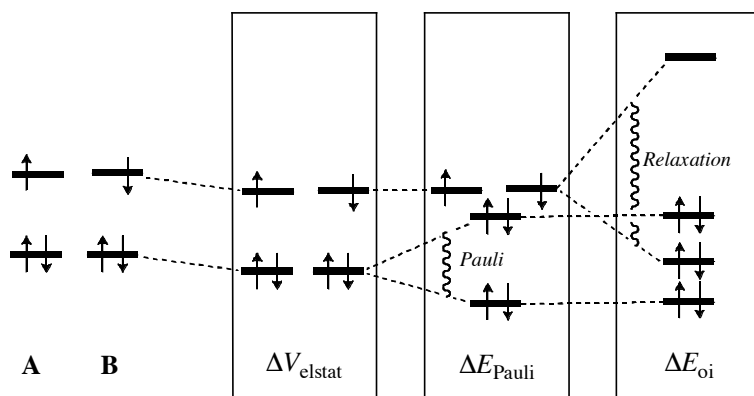


Figure 2.1 Orbital interaction diagram for the interaction of two radical fragments, A and B , in an overall system AB .

The term ΔV_{elstat} corresponds to the classical electrostatic interaction between the unperturbed charge distributions $\rho_A(r) + \rho_B(r)$ of the prepared or deformed radical fragments A and B (*vide infra* for definition of the fragments) that adopt their positions in the overall molecule AB , and is usually attractive. The Pauli repulsion term, ΔE_{Pauli} , comprises the destabilizing interactions between occupied orbitals and is responsible for the steric repulsion. This repulsion is caused by the fact that two electrons with the same spin cannot occupy the same region in space. It arises as the energy change associated with the transition from the superposition of the unperturbed electron densities $\rho_A(r) + \rho_B(r)$ of the geometrically deformed but isolated radical fragments A and B to the wavefunction $\Psi^0 = N \hat{A} [\Psi_A \Psi_B]$, that properly obeys the Pauli principle through explicit antisymmetrization (\hat{A} operator) and renormalization (N constant) of the product of fragment wavefunctions. The orbital interaction ΔE_{oi} in any MO model, and therefore also in Kohn-Sham theory, accounts for electron-pair bonding, charge transfer (i.e., donor–acceptor interactions between occupied orbitals on one moiety with unoccupied orbitals of the other, including the HOMO–LUMO interactions) and polarization (empty–occupied orbital mixing on one fragment due to the presence of another fragment). Since the Kohn-Sham MO method of density-functional

2 Theory and Methods

theory (DFT) in principle yields exact energies and, in practice, with the available density functionals for exchange and correlation, rather accurate energies, we have the special situation that a seemingly one-particle model (an MO method) in principle completely accounts for the bonding energy.

The orbital interaction energy can be decomposed into the contributions from each irreducible representation Γ of the interacting system using the extended transition state (ETS) scheme developed by Ziegler and Rauk^[14] (note that our approach differs in this respect from the Morokuma scheme,^[15] which instead attempts a decomposition of the orbital interactions into polarization and charge transfer):

$$\Delta E_{\text{oi}} = \sum_{\Gamma} \Delta E_{\Gamma} \quad (2.9)$$

References

- [1] A. Szabo, N. S. Ostlund, *Modern Quantum Chemistry: Introduction to Advanced Electronic Structure Theory*, MacMillan Publishing Co., New York, **1982**.
- [2] R. McWeeny, *Methods of Molecular Quantum Mechanics*, 2nd ed., Academic Press, London, **1992**.
- [3] P. W. Atkins, R. S. Friedman, *Molecular Quantum Mechanics*, 3rd ed., Oxford University Press, Oxford, **1997**.
- [4] F. Jensen, *Introduction to Computational Chemistry*, Wiley, Chichester, **1999**.
- [5] W. Koch, M. C. Holthausen, *A Chemist's Guide to Density Functional Theory*, Wiley-VCH, Weinheim **2001**.
- [6] C. Møller, M. S. Plesset, *Phys. Rev.* **1934**, *46*, 618.
- [7] P. Hohenberg, W. Kohn, *Phys. Rev.* **1964**, *136*, B864.
- [8] W. Kohn, L. J. Sham, *Phys. Rev.* **1965**, *140*, A1133.
- [9] (a) E. J. Baerends, D. E. Ellis, P. Ros, *Chem. Phys.* **1973**, *2*, 41; (b) E. J. Baerends, P. Ros, *Chem. Phys.* **1975**, *8*, 412; (c) E. J. Baerends, P. Ros, *Int. J. Quantum. Chem. Symp.* **1978**, *12*, 169; (d) C. Fonseca Guerra, J. G. Snijders, G. te Velde, E. J. Baerends, *Theor. Chem. Acc.* **1998**, *99*, 391 (e) G. te Velde, F. M. Bickelhaupt, E. J. Baerends, C. Fonseca Guerra, S. J. A. van Gisbergen, J. G. Snijders, T. Ziegler, *J. Comput. Chem.* **2001**, *22*, 931.
- [10] (a) A. D. Becke, *Phys. Rev. A* **1988**, *38*, 3098; (b) J. P. Perdew, *Phys. Rev. B* **1986**, *33*, 8822; correction *Phys. Rev. B* **1986**, *34*, 7406.
- [11] N. C. Handy, A. Cohen, *Mol. Phys.* **2001**, *99*, 403; (b) C. Lee, W. Yang and R. G. Parr, *Phys. Rev. B* **1988**, *37*, 785.
- [12] E. van Lenthe, E. J. Baerends, J. G. Snijders, *J. Chem. Phys.* **1994**, *101*, 9783.
- [13] (a) F. M. Bickelhaupt, N. M. Nibbering, E. M. van Wezenbeek, E. J. Baerends, *J. Phys. Chem.* **1992**, *96*, 4864; (b) F. M. Bickelhaupt, E. J. Baerends, in *Reviews in Computational Chemistry*, edited by K. B. Lipkowitz and D. B. Boyd (Wiley-VCH, New York, 2000), Vol. 15; (c) E. J. Baerends, O. V. Gritsenko, *J. Phys. Chem. A* **1997**, *101*, 5383.
- [14] (a) T. Ziegler, A. Rauk, *Inorg. Chem.* **1979**, *18*, 1755; (b) T. Ziegler, A. Rauk, *Inorg. Chem.* **1979**, *18*, 1558; (c) T. Ziegler, A. Rauk, *Theor. Chim. Acta* **1977**, *46*, 1.
- [15] K. Morokuma, *Acc. Chem. Res.* **1977**, *10*, 294.

Part I

Hypervalence

3 Hypervalence and the Delocalizing *versus* Localizing Propensities of H_3^- , Li_3^- , CH_5^- and SiH_5^-

Adapted from S. C. A. H. Pierrefixe, F. M. Bickelhaupt
Struct. Chem. **2007**, *18*, 813

Abstract

Lithium and silicon have the capability to form hypervalent structures, such as Li_3^- and SiH_5^- , which is contrasted by the absence of this capability of hydrogen and carbon, as exemplified by H_3^- and CH_5^- which, although isoelectronic to the former two species, have a distortive, bond-localizing propensity. This well-known fact is nicely confirmed in our DFT study at BP86/TZ2P. We furthermore show that the hypervalence of Li and Si neither originates from the availability of low-energy $2p$ and $3d$ AOs, respectively, nor from differences in the bonding pattern of the valence molecular orbitals; there is, in all cases, a 3-center–4-electron bond in the axial X–A–X unit. Instead, we find that the discriminating factor is the smaller effective size of C as compared to the larger Si atom and the resulting lack of space around the former. Interestingly, a similar steric mechanism is responsible for the difference in bonding capabilities between H and the effectively larger Li atom. This is so despite the fact that the substituents in the corresponding symmetric and linear dicoordinate H_3^- and Li_3^- are on opposite sides of the central atom.

3.1 Introduction

Despite numerous studies, hypervalence in molecular and extended structures continues to be an issue of interest and debate, even to the extent of the meaningfulness of the concept and its very definition, already for about a century.^[1-5] Here, we wish to address the different bonding capabilities of the two group-1 atoms H and Li and of the two group-14 atoms C and Si. While H usually binds no more than one ligand^[6] (except for some examples like the triangular H_3^+), Li, despite being isoelectronic, can bind two or more ligands,^[7] thus exceeding its formal monovalence and constituting a hypervalent compound. Likewise, C can in general bind no more than four ligands^[6] (except for some exotic or controversial examples^[2,8,9]) whereas its isoelectronic equivalent of the third period, i.e., Si, can bind five^[2,9-11] (or sometimes more^[2,12]) substituents. The question we want to tackle here is why lithium and silicon are able to violate their formal mono- and tetravalence, respectively, while hydrogen and carbon do not (or only in rudimentary form) possess this capability?

The nonhypervalence of hydrogen and carbon, on one hand, and the hypervalence of lithium and silicon, on the other hand, is nicely illustrated by comparing the potential energy surfaces of the corresponding $\text{S}_{\text{N}}2$ reactions, which are of the general form:



In the case of the group-1 atoms hydrogen and lithium, i.e., for $\text{X} = \text{Y} = \text{H}$ or Li , the collinear exchange reaction of $\text{H}^- + \text{H}_2$ proceeds via a transition state while that of $\text{Li}^- + \text{Li}_2$ proceeds via a stable transition complex (see also plain and dotted lines, respectively, in Figure 3.1). Thus, although the $D_{\infty h}$ symmetric transition species H_3^- and Li_3^- are isoelectronic and structurally equivalent, H_3^- is a labile species that has the tendency to localize one of its bonds, while Li_3^- is a stable hypervalent equilibrium structure.^[13-15] Likewise, in the case of the group-14 atoms carbon and silicon, i.e., for $\text{X} = \text{H}$ and $\text{Y} = \text{CH}_3$ or SiH_3 , the hydride exchange reaction of $\text{H}^- + \text{CH}_4$ proceeds via labile five-coordinate transition state while that of $\text{H}^- + \text{SiH}_4$ proceeds via a stable, pentavalent transition complex. Thus, again, although the D_{3h} symmetric species are isoelectronic and show equivalent trigonal bipyramidal geometries, HCH_3H^- is a transition state that tends to localize one of its axial C–H bond while HSiH_3H^- is a stable transition complex.^[10,11,15-17]

Obviously, hypervalence is of relevance not only in structural chemistry but also in the field of chemical reactivity. Yet, in the present study, we focus rather on the symmetric transition species with a delocalized structure and the question what causes this species to be hypervalent (i.e., stable) or nonhypervalent (i.e., with a tendency to localize one and partially break another bond). These different propensities can also be recognized in the potential energy surfaces depicted in Figure 3.1.

Our first objective here is to characterize with density functional theory (DFT), the structures and the energetics of the stationary points in the above-mentioned model systems

that involve hypervalently coordinated hydrogen, lithium, carbon and silicon. To this end, we have conducted an extensive and systematic exploration of the potential energy surface (PES) of HCH_3H^- , HSiH_3H^- , H_3^- and Li_3^- , using the ADF program and the generalized gradient approximation (GGA) of DFT at the BP86/TZ2P level.^[18]

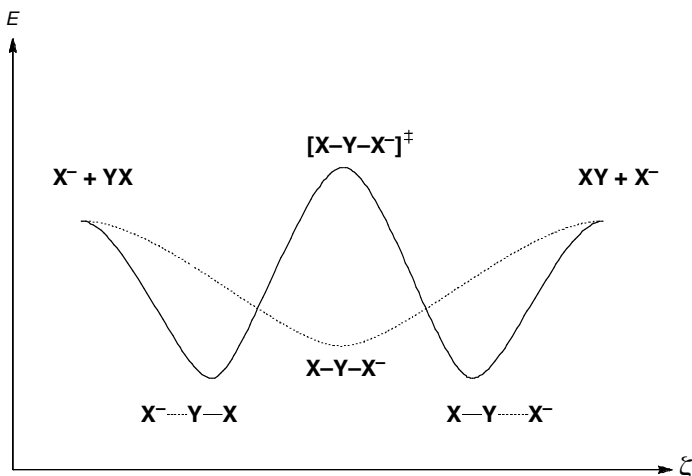
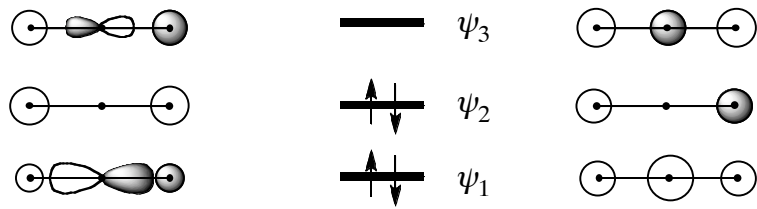


Figure 3.1 Double-well (black line) and single-well (dotted line) $\text{S}_{\text{N}}2$ potential energy surfaces of $\text{X}^- + \text{YX}$, along the reaction coordinate ξ .

The main purpose is however to obtain a more qualitative, physical insight into the factors that determine *why* Li and Si can form hypervalent species whereas H and C cannot. The first proposal to elucidate this puzzling problem was Pauling's idea that the hypervalence of the main group atoms in question derives from the availability of low-energy AOs, *e.g.*, $2p$ and $3d$ in the valence electron shell of lithium and silicon respectively. However, modern *ab initio* calculations showed that, for providing bonding in hypervalent species, the central Si and Li atoms predominantly invoke their valence $3s$ and $3p$ (Si) or $2s$ AOs (Li). The low-energy $3d$ AOs of silicon merely act as corrective polarization functions but not as valence orbitals.^[19] This is again confirmed in the present study. On the other hand, the low-energy $2p$ AOs have been shown to participate more actively in bonding.^[7b] Here, we find however that their contribution is not essential for the hypervalence in Li_3^- .

Nowadays, the bonding in hypervalent species is described, instead, in terms of the 3-center-4-electron (3c-4e) bond.^[20] This model was proposed simultaneously by Pimentel and Rundle^[21] to account for the hypervalency of the central atom in species such as F_3^- and XeF_2 . The 3c-4e bond was formulated in terms of the valence p_{σ} atomic orbitals (AOs) of a linear arrangement of three atoms that yields a well-known pattern of three MOs, ψ_1 , ψ_2 and ψ_3 , similar to those shown in Scheme 3.1, left panel, which are bonding, nonbonding and antibonding, respectively, with the four electrons in ψ_1 and ψ_2 .^[22] A similar formulation in terms of the valence s orbitals was later introduced to account for the bonding in species like H_3^- , see Scheme 3.1 right panel.

Scheme 3.1 Frontier orbitals involved in 3c-4e bonding with central *p* orbitals (left panel) and with central *s* orbitals (right panel).



Note that whereas the 3c-4e MO model accounts for the bonding in hypervalent species, it does *not* explain *why*, for example, silicon and lithium can accommodate more ligands in their valence shell than carbon and hydrogen respectively. Indeed MO theory has so far not elucidated why similar bonding mechanisms (*i.e.* the 3c-4e bonds) yield, in some cases, labile species, such as H_3^- and CH_5^- , and in other cases stable minima as, for example, Li_3^- and SiH_5^- . Here we anticipate that our analyses highlight, in agreement with early work by Schleyer, Dewar or Gillespie,^[4,11,23] that steric factors are important for understanding the hypervalency of SiH_5^- and the nonhypervalency of CH_5^- . Interestingly, steric factors also appear to be responsible for the hypervalency of Li_3^- as opposed to the nonhypervalency of H_3^- , even though the central atom in the latter species is only two-coordinate.

3.2 Theoretical Methods

All calculations were performed using the Amsterdam Density Functional (ADF) program developed by Baerends and others.^[18] The numerical integration was performed using the procedure developed by te Velde et al.^[18g,h] The MOs were expanded in a large uncontracted set of Slater-type orbitals (STOs) containing diffuse functions: TZ2P (no Gaussian functions are involved).^[18i] The basis set is of triple- ζ quality for all atoms and has been augmented with two sets of polarization functions, *i.e.* 3d and 4f on Li, C and Si and 2p and 3d on H. The 1s core shell of carbon and lithium and the 1s2s2p core shell of silicon were treated by the frozen-core approximation.^[18c] An auxiliary set of *s*, *p*, *d*, *f* and *g* STOs was used to fit the molecular density and to represent the Coulomb and exchange potentials accurately in each self-consistent field cycle.^[18j]

Equilibrium structures were optimized using analytical gradient techniques.^[18k] Geometries, energies and vibrational frequencies were computed at the BP86 level of the generalized gradient approximation (GGA): exchange is described by Slater's X α potential^[18l] with corrections due to Becke^[18m,n] added self-consistently and correlation is treated in the Vosko-Wilk-Nusair (VWN) parameterization^[18o] with nonlocal corrections due to Perdew^[18p] added, again, self-consistently (BP86).^[18q]

3.3 Results and Discussions

3.3.1 Structures and Relative Energies

First, we focus on the geometries and relative energies of the various XYX^- species, computed at the BP86/TZ2P level of theory, which are collected in Figure 3.2. Note that Figure 3.2 shows relative energies of any XYX^- relative to $\text{X}^- + \text{YX}$. In line with previous work (see Section 3.1), the $\text{D}_{3\text{h}}$ symmetric five-coordinate CH_5^- (**1a**), which has two equivalent C–H bonds of 1.68 Å, is a first-order saddle-point. It has the propensity to localize one C–H bond to 1.10 Å and to stretch the other C–H bond to 3.83 Å, yielding $\text{H}^- \cdots \text{CH}_4$ (**1b**) in $\text{C}_{3\text{v}}$ symmetry. Whereas the five-coordinate **1a** is 40 kcal/mol above separate $\text{H}^- + \text{CH}_4$, the localized **1b** is at about –1 kcal/mol (see Figure 3.2). We note that **1b** is not the global minimum but a second-order saddle point with two imaginary frequencies that are associated with the $\text{H}^- \cdots \text{C–H}$ bending mode. The real minimum is constituted by a C_s symmetric $\text{H}^- \cdots \text{CH}_4$ species at –3.55 kcal/mol in which, the hydride anion forms a hydrogen bond with one of the methane C–H bonds, to a slightly deformed methane weakly bound to the hydrogen anion via one of the hydrogen of the methane (not shown in Figure 3.2).

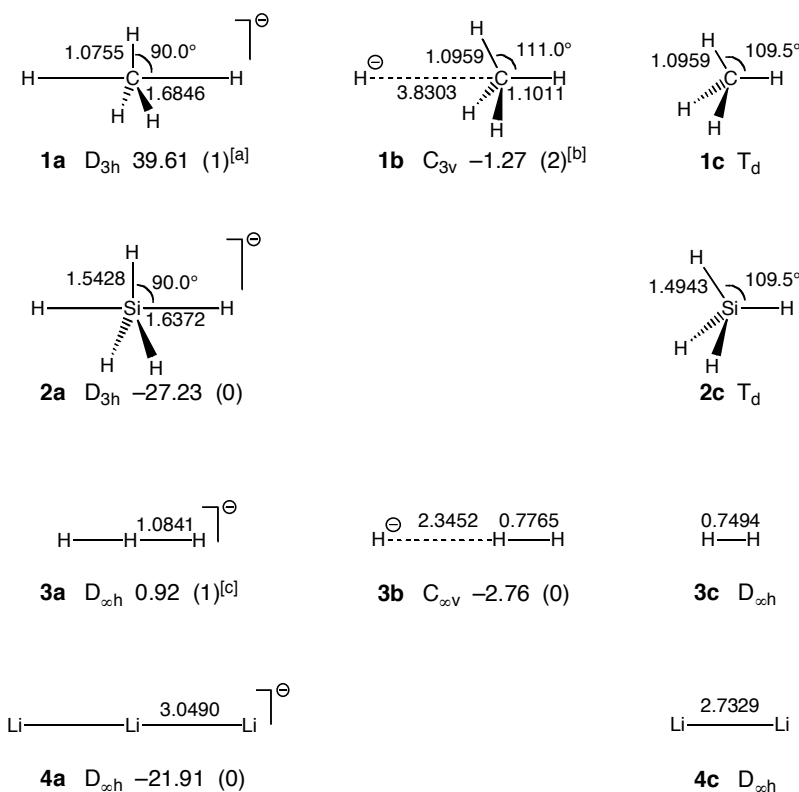


Figure 3.2 Geometries (in Å, deg.), energies relative to reactants $\text{X}^- + \text{YX}$ (in kcal/mol, see also Eq. 3.1) and number of imaginary frequencies (in parentheses) of selected species involved in bonding at C, Si, H and Li (i.e., **1**, **2**, **3** and **4**, respectively), computed at BP86/TZ2P. ^[a] i1234 cm⁻¹. ^[b] i123 cm⁻¹. ^[c] i1083 cm⁻¹.

At variance with the carbon species **1a**, the D_{3h} symmetric five-coordinate SiH_5^- (**2a**), which has two equivalent Si–H bonds of 1.64 Å, is a stable equilibrium structure without any labile, distortive mode (see Figure 3.2). This pentavalent **2a** species is at –27 kcal/mol relative to the separate $\text{H}^- + \text{SiH}_4$.

The group-1 atoms H and Li in A_3^- structures show a similar behavior as the group-14 central atoms in AH_5^- . Thus, the $D_{\infty h}$ symmetric dicoordinate H_3^- (**3a**), which has two equivalent H–H bonds of 1.08 Å, is a first-order saddle-point with the propensity to distort towards a localized $C_{\infty v}$ symmetric $\text{H}^- \cdots \text{H}_2$ (**3b**) structure with a short and a long H–H bond of 0.78 and 2.35 Å, respectively (see Figure 3.2). We find the dicoordinate **3a** at 1 kcal/mol above and the localized **3b** at –3 kcal/mol relative to separate $\text{H}^- + \text{H}_2$. At variance, the $D_{\infty h}$ symmetric dicoordinate Li_3^- (**4a**), which has two equivalent Li–Li bonds of 3.05 Å is a stable, hypervalent species at –22 kcal/mol relative to separate $\text{Li}^- + \text{Li}_2$ (see Figure 3.2).

In conclusion, all structural trends and features in potential energy surfaces computed here agree satisfactorily with earlier experimental and theoretical studies.^[10,11,13-17]

3.3.2 Role of Silicon 3d and Lithium 2p AOs

As pointed out in the introduction, our analyses show that the availability of low-energy 3d and 2p AOs in silicon and lithium, respectively, is not responsible for the capability of these atoms to form hypervalent structures. This insight emerges from computations in which we removed the 2p orbitals of lithium, and the 3d orbitals of silicon from the respective basis sets. The net effect of deleting these low-energy AOs is a destabilization of Li_3^- and SiH_5^- by 1.56 and 7.74 kcal/mol, respectively, relative to the separate reactants (not shown in Figure 3.2). Importantly, however, both Li_3^- and SiH_5^- remain stable hypervalent equilibrium structures. The deletion of the low-energy 2p and 3d AOs does not lead to a distortive, bond localizing propensity. The only effect is the elongation in axial bond lengths compared to the computation with the full basis set. Thus, the Li–Li bonds in Li_3^- expand by 0.1038 Å compared to **4a**. The axial Si–H bonds in SiH_5^- expands by 0.0247 Å compared to **2a** while the equatorial Si–H bonds are more or less unaffected (1.5401 Å compared to 1.5428 in **2a**). Thus, in line with previous work on other hypervalent compounds [19], we find that although the low-energy 2p orbitals of lithium and the 3d orbitals of silicon are important for a correct quantitative description, they are not responsible for the hypervalence of the these atoms. Note that the somewhat larger geometry effects in the case of Li 2p deletion as compared to Si 3d deletion are in line with the earlier finding that lithium 2p AOs participate more actively in bonding.^[7b]

3.3.3 Analysis of CH_5^- versus SiH_5^-

The question remains what *does* cause the difference in bonding capabilities between, on one hand, H and C and, on the other hand, Li and Si. Our analyses of the orbital electronic

structure show that there are also no qualitative differences in terms of the presence or absence of 3c-4e bonding: this bonding pattern occurs pronouncedly in all four symmetric species, i.e., CH_5^- and SiH_5^- (Scheme 3.1, left), and H_3^- and Li_3^- (Scheme 3.1, right).

The origin of the difference in bonding capabilities between C and Si in CH_5^- and SiH_5^- , respectively, appears to be related to the effective size of the central atom and the question if there is sufficient space to bind more than four substituents. A first indication for such steric mechanism is the much larger expansion of the C–H bond in the trigonal bipyramidal CH_5^- (**1a**) compared to CH_4 (**1c**), namely, by 0.59 Å, than that of the Si–H bond in SiH_5^- (**2a**) compared to SiH_4 (**2c**) which amounts to only 0.14 Å (see Figure 3.2).

This observation has inspired us to explore if removal of the steric bulk associated with the equatorial H substituents in CH_5^- (**1a**) would stabilize the resulting linear H–C–H anion and, possibly, make it an equilibrium structure. Note that this species must be a triradical in order to have it in the valence state that this moiety possesses in **1a**. Strikingly, this is exactly what happens as can be seen in Figure 3.3. The optimized geometry of $\text{H}-\text{C}-\text{H}^{\cdot\cdot\cdot}$ is indeed stable with respect to bond localization. If we optimize $\text{H}-\text{C}-\text{H}^{\cdot\cdot\cdot}$ in $\text{C}_{\infty v}$ symmetry the resulting species **5a** has two equivalent C–H bonds of 1.13 Å, nearly of the same length (only 0.03 Å longer) as those in CH_4 (**1c**).^[24] This agrees well with the idea that by going from five- to two-coordination, we have created sufficient space around carbon to accommodate the remaining H substituents in a stable fashion. The removal of the equatorial H substituents from SiH_5^- (**2a**) does not lead to a reduction of the Si–H bond length, in line with the picture that the larger silicon atom already had sufficient space to accommodate all five H substituents in **2a**. The resulting $\text{D}_{\infty h}$ symmetric $\text{H}-\text{Si}-\text{H}^{\cdot\cdot\cdot}$ (**6a**) remains stable with respect to bond length alternation, and the Si–H bonds are even slightly (i.e., 0.05 Å) longer than in SiH_5^- (**2a**) (see Figure 3.3).

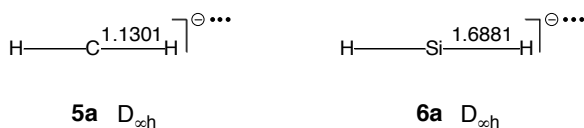


Figure 3.3 Geometries (in Å) of $\text{H}-\text{C}-\text{H}^{\cdot\cdot\cdot}$ (**5a**) and $\text{H}-\text{Si}-\text{H}^{\cdot\cdot\cdot}$ radicals (**6a**), computed at BP86/TZ2P.

The above results support the "steric model" of (non)hypervalence in which the five H substituents, especially along the axial direction, can not simultaneously approach the small carbon atom "sufficiently" closely, i.e., they can not adopt an intrinsically (close-to) optimal C–H distance. This picture gains further support from the following numerical experiments. If CH_5^- (**1a**) is labile due to too long, especially axial C–H bonds, then simply displacing the central C atom along the molecular axis towards one of the axial hydrogen atoms *in an otherwise frozen H_5 structure* (i.e., the five hydrogen substituents retain their relative positions as in **1a**), should cause a similar energy lowering as allowing CH_5^- (**1a**) to fully

relax towards $\text{H}^- \cdots \text{CH}_4$ (**1b**). As shown in Figure 3.4a, this is again exactly what happens. Note that the energy of SiH_5^- , as one might expect, *increases* if we carry out the corresponding numerical experiment of moving the central Si atom of **2b** towards an axial hydrogen atom while keeping the five hydrogen atoms frozen to their geometry in **2b** (see Figure 3.4a).

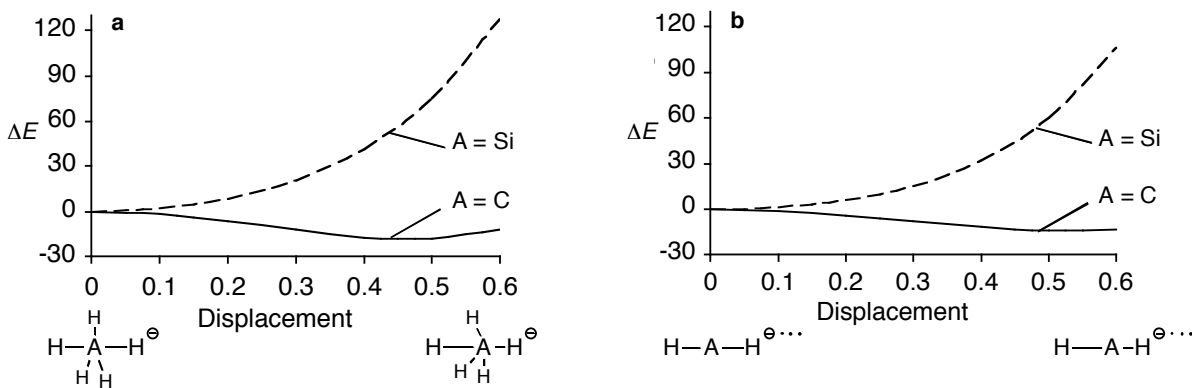


Figure 3.4 Energy (in kcal/mol) relative to the symmetric structure, (a) for $\text{H}-\text{CH}_3-\text{H}^-$ and $\text{H}-\text{SiH}_3-\text{H}^-$ and (b) for $\text{H}-\text{C}-\text{H}^{-\cdots}$ and $\text{H}-\text{Si}-\text{H}^{-\cdots}$, as a function of the displacement (in Å) of the central atom A along the main symmetry axis towards an axial H substituent in the otherwise frozen $\text{H}-\text{H}_3-\text{H}$ (a) and $\text{H}-\text{H}$ moiety (b), computed at BP86/TZ2P.

The same numerical experiments as those shown in Figure 3.4a have also been carried out in the absence of the equatorial H substituents, i.e., for $\text{H}-\text{C}-\text{H}^{-\cdots}$ and $\text{H}-\text{Si}-\text{H}^{-\cdots}$ species with frozen $\text{H}^{\text{axial}}-\text{H}^{\text{axial}}$ distances taken from **1a** and **2a**, respectively (see Figure 3.4b). As can be seen, the change in energy of these $\text{H}-\text{C}-\text{H}^{-\cdots}$ and $\text{H}-\text{Si}-\text{H}^{-\cdots}$ species (Figure 3.4b) closely resembles that of the corresponding ones *with* the three equatorial H atoms (Figure 3.4a). This suggests that as the CH_5^- species cannot accommodate all 5 H substituents at sufficiently short H distances, stabilization can be achieved by partially break ("giving up") one of the anyway too long axial C–H bonds and to localize the other one, yielding net stabilization. This is not necessary in SiH_5^- because here all Si–H bonds are already relatively close to their intrinsic optimum and localization rather destabilizes the system.

3.3.4 Analysis of H_3^- versus Li_3^-

Thus, steric overcrowding around the smaller carbon atom in five-coordinate CH_5^- (**1a**) prevents the latter from being stable, as opposed to the stable hypervalent SiH_5^- (**2a**) in which there is sufficient room around the larger silicon atom. Could such steric arguments also explain the difference in bonding capabilities between H_3^- and Li_3^- ? This seems not so plausible, at first sight, because the two terminal substituents in these species (**3a** and **4a** in Figure 3.2) are on opposite sides of the central atom and one might therefore expect that they are never in steric contact.

Strikingly, however, we find that steric factors make the difference between the nonhypervalent H_3^- and the hypervalent Li_3^- . In the first place, the expansion of the H–H bond in the symmetric H_3^- (**3a**) compared to H_2 (**3c**) is larger than that of the Li–Li bond in Li_3^- (**4a**) compared to Li_2 (**4c**) (see Figure 3.2). Note that, whereas in absolute numbers the bond-length expansions seem to be not so different, i.e., +0.33 versus +0.32 Å, respectively, these values correspond to an elongation by +45% for the H–H bond in **3a** as compared to the much smaller expansion of +12% for the Li–Li bond in **4a**. This difference in behavior between H_3^- and Li_3^- is strongly reminiscent of the corresponding differences between CH_5^- and SiH_5^- .

To further reveal the origin of the destabilization and H–H bond elongation in H_3^- (**3a**), we have scanned the potential energy surface as a function of a symmetric variation of both H–H bond distances, i.e., $D_{\infty h}$ symmetry is preserved. In Figure 3.5a, one can see how the energy of H_3^- rises if, proceeding from the stationary point **3a**, the H–H distances decrease or increase. This is not unexpected, of course, and exactly the same happens in the analogous numerical experiment with Li_3^- (see Figure 3.5b). It becomes interesting, however, if we decompose this net energy into two steps, corresponding with bringing together first the terminal substituents in $[\text{A} \cdots \text{A}]^{\bullet-}$ (see Eq. 3.2) followed by the assembly of these substituents and the central atom A^\bullet to yield the overall A_3^- species (see Eq. 3.3, $\text{A} = \text{H}, \text{Li}$):



As can be clearly seen in Figure 3.5a, the energy of $D_{\infty h}$ symmetric H_3^- as a function of the H–H distance is the result of a trade-off at $\text{H}-\text{H} = 1.08 Å between, on one hand, minimizing by H–H expansion the repulsive energy of the moiety of the outer substituents $[\text{H} \cdots \text{H}]^{\bullet-}$ and, on the other hand, maximizing by H–H contraction the bonding with the central H atom. Clearly, the outer H substituents in H_3^- (**3a**) are in steric contact and repel each other.$

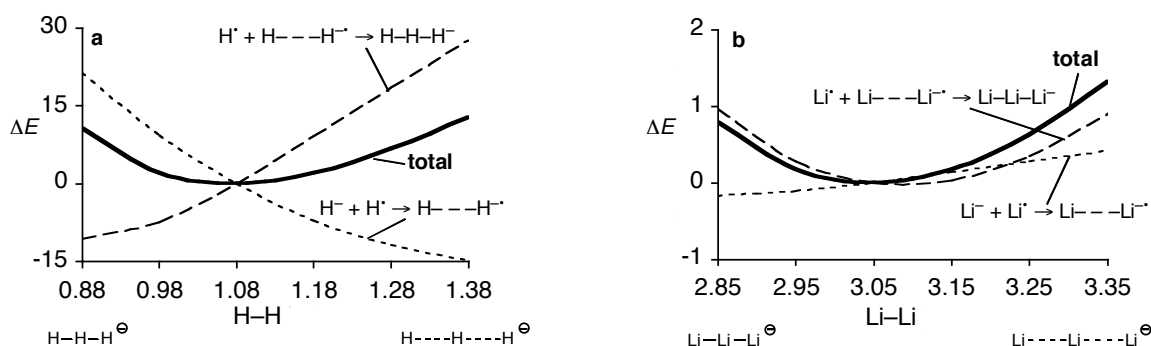


Figure 3.5 Energy (in kcal/mol) of $D_{\infty h}$ symmetric $\text{H}-\text{H}-\text{H}^-$ (a) and $\text{Li}-\text{Li}-\text{Li}^-$ (b) relative to the transition state (**3a**) and stable transition complex (**4a**) structures, respectively, as a function of the A–A distance (in Å, A = H or Li), computed at BP86/TZ2P. The relative energies (bold lines, designated "total") are decomposed as indicated by the partial reactions (see Eq. 3.2 and 3.3).

The above situation for H_3^- differs dramatically from the one of Li_3^- which is shown in Figure 3.5b. Here, the energy curve for the moiety of the outer substituents $[\text{Li}-\cdots-\text{Li}]^\bullet$ is very shallow. Note that in fact it is even slightly attractive at the equilibrium Li–Li distance of 3.05 in **4a** (see Figure 3.5b). This is at variance with the $[\text{H}-\cdots-\text{H}]^\bullet$ curve, which is pronouncedly repulsive around the H–H optimum in H_3^- (see Figure 3.5a). Thus, the terminal Li substituents in Li_3^- (**4b**) only weakly interact. The driving force for the optimum Li–Li distance is predominantly the Li–Li bonding between the terminal substituents $[\text{Li}-\cdots-\text{Li}]^\bullet$ and the central Li^\bullet atom (see Figure 3.5b).

Thus, the direct repulsion between the terminal H atoms in H_3^- prevents them from coming sufficiently close to the central H atom. In line with this picture, displacing the central H atom in H_3^- (**3a**) towards one of the H substituents (while keeping the geometry of the outer substituents frozen to that in (**3a**) causes one strong H–H bond to be formed which indeed goes with a stabilization of the system (see Figure 3.6). A similar displacement of the central Li atom in Li_3^- (**4a**) yields instead a destabilization, as one might expect. This difference in behavior between H_3^- and Li_3^- is reminiscent of the difference in behavior between CH_5^- and SiH_5^- , described above.

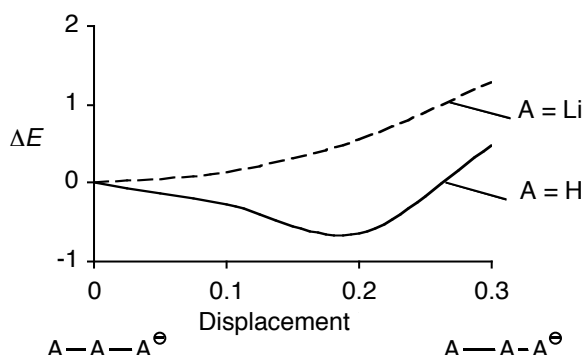


Figure 3.6. Energy (in kcal/mol) relative to the symmetric structure for $\text{H}-\text{H}-\text{H}^-$ and $\text{Li}-\text{Li}-\text{Li}^-$ as a function of the displacement (in Å) of the central atom A (= H or Li) along the main symmetry axis towards an axial A substituent in the otherwise frozen A---A moiety, computed at BP86/TZ2P.

Finally, in accordance with the steric model developed above, if we replace the central H atom in H_3^- (**3a**) by the larger Li atom, a stable $D_{\infty h}$ symmetric $\text{H}-\text{Li}-\text{H}^-$ species results. This $\text{H}-\text{Li}-\text{H}^-$ species has two equivalent Li–H bonds of 1.75 Å and is at -55.74 kcal/mol with respect to separate $\text{H}^- + \text{LiH}$ (data not shown in the figures). The distance between the outer hydrogen substituents in $\text{H}-\text{Li}-\text{H}^-$ (3.50 Å) is significantly larger than in H_3^- (**3a**: 2.17 Å). Consequently, the outer hydrogens in $\text{H}-\text{Li}-\text{H}^-$ are (at variance to the situation of **3a**) not in steric contact, and thus a stable hypervalent species can occur.

3.4 Conclusions

The hypervalence of lithium and silicon as opposed to the nonhypervalence of the isoelectronic hydrogen and carbon atoms (exemplified in this theoretical study by Li_3^- , SiH_5^- , H_3^- and CH_5^- , respectively) is shown to neither originate from the availability of low-energy $3d$ and $2p$ AOs, respectively, nor from differences in the bonding pattern of the valence molecular orbitals. In all model species analyzed, we find the 3-center–4-electron bonding pattern in the axial X–A–X unit. We show that instead the discriminating factor is the smaller effective size of C as compared to the larger Si atom and the resulting lack of space around the former.

Interestingly, a similar steric mechanism appears to be responsible for the difference in bonding capabilities between H and the effectively larger Li atom. This may seem remarkable because of the fact that the substituents in the corresponding symmetric and linear dicoordinate H_3^- and Li_3^- are on opposite sides of the central atom, seemingly out of each other's way. However, the small effective size of hydrogen causes very short H–H bonds in H_3^- . This, in turn, yields a short mutual distance, less than 2.2 Å, between the terminal H atoms which, therefore, are in steric contact. The terminal Li atoms in Li_3^- , on the other hand, are separated by 6.1 Å and have virtually no steric contact.

References

- [1] G. N. Lewis, *J. Am. Chem. Soc.* **1916**, *38*, 762.
- [2] K. Y. Akiba, *Chemistry of Hypervalent Compounds*; Wiley-VCH, New York, **1998**.
- [3] (a) R. Hoffmann, *Solids and Surfaces: A Chemist's View of Bonding in Extended Structures*; John Wiley & Sons Inc, New York, **1989**; (b) J. I. Musher, *Angew. Chem. Int. Ed. Engl.* **1969**, *8*, 54; (c) L. Pauling, *The Nature of the Chemical Bond*; Cornell University Press: Ithaca, New York, **1960**.
- [4] (a) S. Noury, B. Silvi, R. J. Gillespie, *Inorg. Chem.* **2002**, *41*, 2164; (b) R. J. Gillespie, E. A. Robinson, *Inorg. Chem.* **1995**, *34*, 978.
- [5] J. Cioslowski, S. T. Mixon, *Inorg. Chem.* **1993**, *32*, 3209.
- [6] (a) M. B. Smith, J. March, *Advanced Organic Chemistry: Reactions, Mechanisms and Structure*, Wiley-Interscience, New York, **2001**; (b) F. A. Carey, R. J. Sundberg, *Advanced Organic Chemistry: Structure And Mechanisms (Part A)*, Springer, New York, **2000**; (c) A. Streitwieser, C. H. Heathcock, E. M. Kosower, *Introduction to Organic Chemistry*, Prentice Hall, Paramus, **1998**.
- [7] (a) R. O. Jones, A. Lichtenstein, J. J. Hutter, *Chem. Phys.* **1997**, *106*, 4566; (b) F. M. Bickelhaupt, N. Hommes, C. Fonseca Guerra, E. J. Baerends, *Organometallics* **1996**, *15*, 2923; (c) F. M. Bickelhaupt, M. Solà, C. Fonseca Guerra, *J. Chem. Theory Comput.* **2006**, *2*, 965.
- [8] (a) K. Y. Akiba, M. Yamashita, Y. Yamamoto, S. Nagase, *J. Am. Chem. Soc.* **1999**, *121*, 10644; (c) G. A. Olah, G. K. S. Prakash, R. E. Williams, L. D. Field, K. Wade, *Hypercarbon chemistry*, John Wiley & Sons Inc, New York, **1987**; (c) T. R. Forbus, J. C. Martin, *J. Am. Chem. Soc.* **1979**, *101*, 5057.
- [9] (a) J. C. Martin, *Science* **1983**, *221*, 509; (b) A. P. Bento, F. M. Bickelhaupt, *J. Org. Chem.* **2007**, *72*, 2201; (c) A. P. Bento, M. Solà, F. M. Bickelhaupt, *J. Comput. Chem.* **2005**, *26*, 1497.

- [10] (a) D. J. Hajdasz, R. R. Squires, *J. Am. Chem. Soc.* **1986**, *108*, 3139; (b) D. L. Wilhite, L. Spialter, *J. Am. Chem. Soc.* **1973**, *95*, 2100; (c) F. Keil, R. Ahlrichs, *Chem. Phys.* **1975**, *8*, 384; (d) D. J. Hajdasz, Y. H. Ho, R. R. Squires, *J. Am. Chem. Soc.* **1994**, *116*, 10751.
- [11] A. E. Reed, P. v. R. Schleyer, *Chem. Phys. Lett.* **1987**, *133*, 553.
- [12] (a) G. L. Gutsev, *Chem. Phys. Lett.* **1991**, *184*, 305; (b) W. C. Hamilton, *Acta Crystallographica* **1962**, *15*, 353.
- [13] (a) O. K. Kabbaj, M. B. Lepetit, J. P. Malrieu, G. Sini, P. C. Hiberty, *J. Am. Chem. Soc.* **1991**, *113*, 5619; (b) O. K. Kabbaj, F. Volatron, J. P. Malrieu, *Chem. Phys. Lett.* **1988**, *147*, 353; (c) B. Braïda, P. C. Hiberty, *J. Am. Chem. Soc.* **2004**, *126*, 14890.
- [14] (a) H. H. Michels, J. A. Montgomery, *Chem. Phys. Lett.* **1987**, *139*, 535; (b) J. Starck, W. Meyer, *Chem. Phys.* **1993**, *176*, 83.
- [15] F. Keil, R. Ahlrichs, *J. Am. Chem. Soc.* **1976**, *98*, 4787.
- [16] (a) P. Baybutt, *Mol. Phys.* **1975**, *29*, 389; (b) M. T. Carroll, M. S. Gordon, T. L. Windus, *Inorg. Chem.* **1992**, *31*, 825; (c) C. D. Ritchie, G. A. Chappell, *J. Am. Chem. Soc.* **1970**, *92*, 1819; (d) A. Dedieu, A. Veillard, *J. Am. Chem. Soc.* **1972**, *94*, 6730; (e) J. D. Payzant, K. Tanaka, L. D. Betowski, D. K. Bohme, *J. Am. Chem. Soc.* **1976**, *98*, 894; (f) Z. Shi, R. J. Boyd, *J. Phys. Chem.* **1991**, *95*, 4698.
- [17] (a) G. Sini, P. C. Hiberty, S. S. Shaik, *J. Chem. Soc., Chem. Comm.* **1989**, 772; (b) G. Sini, G. Ohanessian, P. C. Hiberty, S. S. Shaik, *J. Am. Chem. Soc.* **1990**, *112*, 1407.
- [18] (a) G. te Velde, F. M. Bickelhaupt, E. J. Baerends, C. Fonseca Guerra, S. J. A. van Gisbergen, J. G. Snijders, T. Ziegler, *J. Comput. Chem.* **2001**, *22*, 931; (b) C. Fonseca Guerra, O. Visser, J. G. Snijders, G. te Velde, E. J. Baerends, in *Methods and Techniques for Computational Chemistry*, (Eds.: E. Clementi, G. Corongiu), STEF: Cagliari, **1995**, 305; (c) E. J. Baerends, D. E. Ellis, P. Ros, *Chem. Phys.* **1973**, *2*, 41; (d) E. J. Baerends, P. Ros, *Chem. Phys.* **1975**, *8*, 412; (e) E. J. Baerends, P. Ros, *Int. J. Quantum. Chem. Symp.* **1978**, *12*, 169; (f) C. Fonseca Guerra, J. G. Snijders, G. te Velde, E. J. Baerends, *Theor. Chem. Acc.* **1998**, *99*, 391; (g) P. M. Boerrigter, G. te Velde, E. J. Baerends, *Int. J. Quantum Chem.* **1988**, *33*, 87; (h) G. te Velde, E. J. Baerends, *J. Comp. Phys.* **1992**, *99*, 84; (i) J. G. Snijders, E. J. Baerends, P. Vernooij, *At. Nucl. Data Tables* **1982**, *26*, 483; (j) J. Krijn, E. J. Baerends, *Fit-Functions in the HFS-Method; Internal Report (in Dutch)*, Vrije Universiteit, Amsterdam, **1984**; (k) L. Versluis, T. Ziegler, *J. Chem. Phys.* **1988**, *88*, 322; (l) J. C. Slater, *Quantum Theory of Molecules and Solids*, Vol. 4, McGraw-Hill, New York, **1974**; (m) A. D. Becke, *J. Chem. Phys.* **1986**, *84*, 4524; (n) A. D. Becke, *Phys. Rev. A* **1988**, *38*, 3098; (o) S. H. Vosko, L. Wilk, M. Nusair, *Can. J. Phys.* **1980**, *58*, 1200; (p) J. P. Perdew, *Phys. Rev. B* **1986**, *33*, 8822 (Erratum: *Phys. Rev. B* **1986**, *34*, 7406); (q) L. Fan, T. Ziegler, *J. Chem. Phys.* **1991**, *94*, 6057.
- [19] (a) W. Kutzelnigg, *Angew. Chem. Int. Ed. Engl.* **1984**, *23*, 272; (b) E. Magnusson, *J. Am. Chem. Soc.* **1990**, *112*, 7940; (c) A. E. Reed, P. v. R. Schleyer, *J. Am. Chem. Soc.* **1990**, *112*, 1434; (d) F. M. Bickelhaupt, M. Solà, P. v. R. Schleyer, *J. Comput. Chem.* **1995**, *16*, 465.
- [20] R. Hoffmann, J. M. Howell, E. L. Muetterties, *J. Am. Chem. Soc.* **1972**, *94*, 3047.
- [21] (a) G. C. Pimentel, *J. Chem. Phys.* **1951**, *19*, 446; (b) R. J. Hach, R. E. Rundle, *J. Am. Chem. Soc.* **1951**, *73*, 4321.
- [22] (a) G. A. Landrum, N. Goldberg, R. Hoffmann, *J. Chem. Soc., Dalton Trans.* **1997**, 3605; (b) C. A. Ramsden, *Chem. Soc. Rev.* **1994**, *23*, 111; (c) T. A. Albright, J. K. Burdett, M.-H. Whangbo, *Orbital Interactions in Chemistry*, John Wiley & Sons Inc, New-York, **1985**.
- [23] M. J. S. Dewar, E. Healy, *Organometallics* **1982**, *1*, 1705.
- [24] Whereas **5a** is stable with respect to C–H bond localization, it is labile with respect to H–C–H bending. The C_{2v} symmetric equilibrium structure is 2.06 kcal/mol more stable than **5a**, has an H–C–H angle of 142° and C–H bonds of 1.12 Å, essentially the same as in **5a**.

4 Hypervalent Silicon *versus* Carbon: Ball-in-a-Box Model

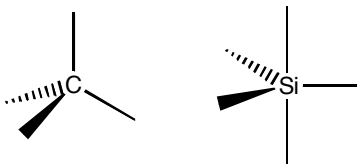
Adapted from S. C. A. H. Pierrefixe, C. Fonseca Guerra, F. M. Bickelhaupt
Chem. Eur. J. **2008**, *14*, 819

Abstract

Why is silicon hypervalent and carbon not? Or, why is $[\text{Cl}-\text{CH}_3-\text{Cl}]^-$ labile, with a tendency to localize one of its axial C–Cl bonds and to largely break the other one, while the isostructural and isoelectronic $[\text{Cl}-\text{SiH}_3-\text{Cl}]^-$ forms a stable pentavalent species, with a delocalized structure featuring two equivalent Si–Cl bonds? Various hypotheses have been developed over the years focusing on electronic but also on steric factors. Here, we present the so-called ball-in-a-box model which tackles hypervalence from a new perspective. The ball-in-a-box model reveals the key role of steric factors and provides a simple way of understanding the above phenomena in terms of different atom sizes. Our bonding analyses are supported by numerical experiments in which we probe, among others, the shape of the S_N2 potential energy surface of Cl^- attacking the carbon atom in the series of substrates CH_3Cl , ${}^1\text{CH}_2\text{Cl}$, ${}^2\text{CHCl}$ and ${}^3\text{CCl}$. Our findings for ClCH_3Cl^- and $\text{ClSiH}_3\text{Cl}^-$ are generalized to other group-14 central atoms (Ge, Sn and Pb) and axial substituents (F).

4.1 Introduction

The concept of hypervalence is challenging chemists already for about a century.^[1] Over the decades, the hypervalence or nonhypervalence of various atoms in both molecular as well as extended structures has been investigated.^[2,3] But also the definition and meaningfulness of the very concept itself has been the subject of, at times vigorous, discussions.^[4,5] Here, we will not enter into such a discussion. The issue that we wish to address is the different bonding capabilities of the two group-14 atoms carbon and silicon: why does carbon, as illustrated below, bind not more than four ligands^[6] (except for some exotic or controversial examples^[2,7,8]) while silicon, despite being isoelectronic, can bind five^[2,8,9] (or sometimes six, and even more^[2,10]) substituents?



The above question also provides us with a robust and intuitive definition, rooted in experimental (and computational) observation, of hypervalence, as being the capability of silicon (as opposed to the incapability of carbon) to exceed its "normal" tetravalence and form also pentavalent, trigonal bipyramidal species.

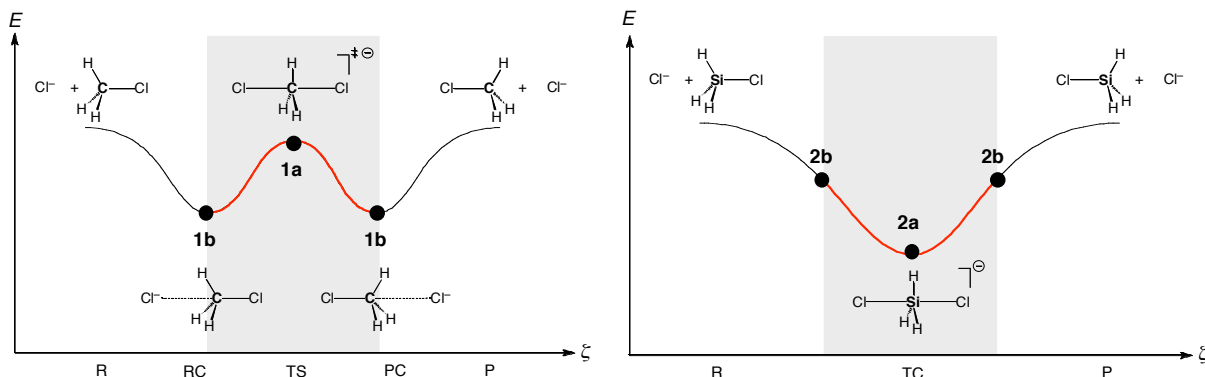
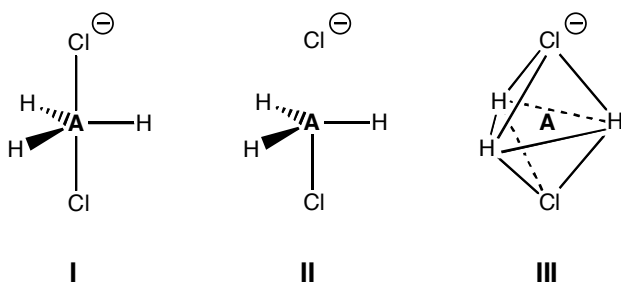


Figure 4.1 Double-well $\text{S}_{\text{N}}2@\text{C}$ (left) and single-well $\text{S}_{\text{N}}2@\text{Si}$ (right) potential energy surfaces along the reaction coordinate ξ (R = reactants, RC = reactant complex, TS = transition state, TC = stable transition complex, PC = product complex, P = products).

The nonhypervalence of carbon and the hypervalence of silicon are exemplified by the pentavalent D_{3h} symmetric species ClCH_3Cl^- (**1a**) and $\text{ClSiH}_3\text{Cl}^-$ (**2a**). While the former is a first-order saddle point that is labile towards localizing of one C–Cl bond and (largely) breaking the other one, the latter is a stable pentavalent species. This is well known as these species feature as the transition state and the stable transition complex in the intensively studied nucleophilic substitution reactions of $\text{Cl}^- + \text{CH}_3\text{Cl}$ ($\text{S}_{\text{N}}2@\text{C}$)^[11-13] and $\text{Cl}^- + \text{SiH}_3\text{Cl}$ ($\text{S}_{\text{N}}2@\text{Si}$)^[9,13-16] respectively (see Figure 4.1). Recently, we have analyzed these reactions in

terms of the rigidity and mutual interaction of the *reactants* (i.e., the nucleophile and the substrate) using the Activation Strain model.^[16] It was shown that the crucial factor for having a central barrier for S_N2@C and thus a labile pentavalent carbon atom is mainly the increased steric repulsion between the nucleophile and the substituents. The central barrier disappears in the S_N2@Si reaction because the larger distance between nucleophile and substituents reduces this steric repulsion. Moreover, in line with this steric picture, the central barrier can be again reintroduced in S_N2@Si reactions if the equatorial substituents are made sterically more demanding.^[16]

In the present study, we wish to approach the phenomenon of hypervalency from a different perspective. Instead of a description of **I** in terms of the two S_N2 reactants **II**, we aim at understanding the lability of five-coordinate carbon and the stability of pentavalent silicon in terms of the central carbon versus silicon atom interacting with the five surrounding (also mutually interacting) substituents **III**:



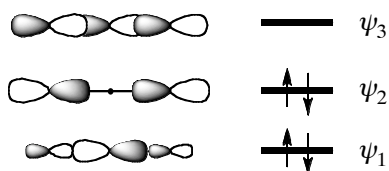
Of course, the description of **I** in terms of **II** is, ultimately, equivalent to that in terms of **III**. It appears however that the alternative description **III** offers a simple and transparent way of understanding hypervalence (which we designate "ball-in-a-box" model) that complements and integrates previous models of hypervalency.

Thus, we have analyzed the bonding in ClCH₃Cl⁻ (**1**) and ClSiH₃Cl⁻ (**2**) as well as in fragments thereof, such as, the "box" of five substituents that "contains" the central C or Si atom, using the ADF program at the BP86/TZ2P level of density functional theory (DFT).^[17,18] The analyses are carried out not only in the geometries of the various species that correspond to the D_{3h} symmetric **1a** and **2a** (see Figure 4.2) but also along various deformation modes. In the first place, we have analyzed how the bonding changes if one proceeds from the symmetric species along the localization coordinate ζ which for **1** and **2** is associated with a convex and concave potential energy surface (PES), respectively (see Figure 4.1). Another deformation mode corresponds to the symmetric Cl–A–Cl stretch. Our bonding analyses are augmented (and supported) by numerical experiments in which we probe, among others, the shape of the S_N2 potential energy surface of Cl⁻ attacking the carbon atom in the series of substrates CH₃Cl, ¹CH₂Cl, ²CHCl and ³CCl. The findings for **1** and **2** are generalized by examining other group-14 central atoms (germanium, tin and lead, in which case relativistic effects are treated using ZORA^[17r]) and axial substituents (fluorine).

The bonding analyses consist of a decomposition of the total energy into interaction energies between (and within) fragments of the overall model systems **1** and **2**. The trends in the various energy terms are interpreted in the conceptual framework provided by the quantitative molecular orbital (MO) model contained in Kohn-Sham DFT.^[18]

Qualitative MO analyses of pentacoordination were carried out already in the early seventies by Hoffmann and coworkers^[19] who arrived at a bonding mechanism that naturally incorporates the 3-center-4-electron (3c-4e) bond proposed by Pimentel and Rundle^[20] to account for the hypervalency of the central atom in species such as F_3^- and XeF_2 . Originally, the 3c-4e bond was formulated in terms of the valence p_σ atomic orbitals (AOs) of a linear arrangement of three atoms that yields a well-known pattern of three MOs: ψ_1 , ψ_2 and ψ_3 , shown in Scheme 4.1. These MOs are bonding, nonbonding and antibonding, respectively, with four electrons occupying together ψ_1 and ψ_2 .^[21,22] This bonding pattern was confirmed by *ab initio* calculations which showed that the central atom in hypervalent species predominantly invokes its *s* and *p* AOs for bonding and that the *d* AOs merely act as corrective polarization functions but not as valence orbitals.^[23] These and other results have falsified Pauling's (plausible but, in the end, incorrect) hypothesis that the hypervalence of maingroup atoms such as silicon derives from the availability of low-energy *d* AOs. These findings are all confirmed by the present study and will not be further discussed.

Scheme 4.1 MOs involved in 3c-4e bonding



Note that, while the 3c-4e MO model is a good description of the bonding in hypervalent species, it does not explain *why* such a bonding mechanism leads to stable hypervalent species in the case of silicon as the central atom but *not* in the case of carbon. On the other hand, in a valence bond (VB) study of the model systems CH_5^- and SiH_5^- , Hiberty, Shaik and coworkers^[24] were able to provide a qualitative explanation based on curve-crossing diagrams of VB configurations. They showed that the comparatively low-energy σ^* orbitals of the equatorial Si–H bonds can accommodate the fifth valence-electron pair which, in the 3c-4e MO model of Scheme 4.1, corresponds to a stabilization of Ψ_2 . The σ^* orbitals of the equatorial C–H bonds do not possess this capability (they are too high in energy). This results in a long axial H–C–H linkage and a high energy of CH_5^- relative to $\text{CH}_4 + \text{H}^-$.

The ball-in-a-box model presented herein makes MO theory in a sense catch up with VB theory regarding the treatment and understanding of why certain atoms (such as silicon) can form stable hypervalent configurations and others (such as carbon) can not. The qualitative picture that emerges is that the five substituents form a cage or "box" (in which they are in

mutual steric contact) and the central atom is a "ball" in that box. Silicon fits nearly exactly into this box and can bind simultaneously to the top and the bottom. At variance, the carbon atom is too small to touch both the top and the bottom and it can thus only bind to one of them. In this way, our ball-in-a-box model nicely integrates the bonding ("electronic factors") and repulsive features ("steric factors") in the bonding mechanism and thus highlights the importance of the relative size of the central atom.^[4,13,15]

4.2 Theoretical Methods

All calculations were performed using the Amsterdam Density Functional (ADF) program developed by Baerends and others.^[17] The numerical integration was performed using the procedure developed by te Velde et al.^[17g,h] The MOs were expanded in a large uncontracted set of Slater-type orbitals (STOs) containing diffuse functions: TZ2P (no Gaussian functions are involved).^[17i] The basis set is of triple- ζ quality for all atoms and has been augmented with two sets of polarization functions (i.e., 2p and 3d on H; 3d and 4f on C, F, Si and Cl; 4d and 4f on Ge; 5d and 4f on Sn; 6d and 5f on Pb). Core shells were treated by the frozen-core approximation (1s of C and F; 1s2s2p of Si and Cl; 1s2s2p2s3p of Ge; 1s2s2p2s3p3d4s4p of Sn; 1s2s2p2s3p4s4p4d of Pb).^[17c] An auxiliary set of s, p, d, f and g STOs was used to fit the molecular density and to represent the Coulomb and exchange potentials accurately in each self-consistent field cycle.^[17j]

Equilibrium structures were optimized using analytical gradient techniques.^[17k] Geometries, energies and vibrational frequencies were computed at the BP86 level of the generalized gradient approximation (GGA): exchange is described by Slater's X α potential^[17l] with corrections due to Becke^[17m,n] added self-consistently and correlation is treated in the Vosko-Wilk-Nusair (VWN) parameterization^[17o] with nonlocal corrections due to Perdew^[17p] added, again, self-consistently.^[17q] For species containing Ge, Sn or Pb, relativistic effects are treated using the zeroth-order regular approximation (ZORA).^[17r]

The bonding in ClCH₃Cl⁻, ClSiH₃Cl⁻ and other species was analyzed using the quantitative molecular orbital (MO) model contained in Kohn-Sham DFT.^[18,25,26]

4.3 Results and Discussions

4.3.1 Structures and Potential Energy Surfaces

In line with previous work (see Figure 4.1 and Section 4.1), we find that D_{3h} symmetric pentacoordinate ClCH₃Cl⁻ (**1a**) is labile towards localization of one and elongation of the other C–Cl bond (i.e., a first-order saddle-point on the PES) whereas D_{3h} symmetric ClSiH₃Cl⁻ (**2a**) constitutes a stable pentavalent species (see Figure 4.2). An important observation, as will become clear later on, is that the C–Cl bonds of 2.3516 Å in the carbon species **1a** are nearly equally long as the Si–Cl bonds of 2.3592 Å in the silicon species **2a** (see Figure 4.2).

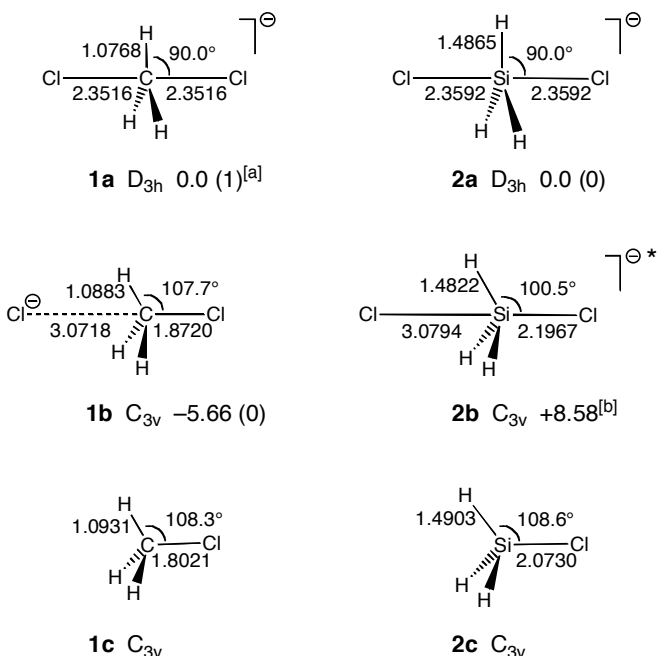


Figure 4.2 Geometries (in Å, deg.), relative energies (in kcal/mol) and number of imaginary frequencies (in parentheses) of selected carbon (**1a-c**) and silicon (**2a-c**) structures, computed at BP86/TZ2P. ^[a] $i316\text{ cm}^{-1}$. ^[b] **2b** is *not* a stationary point (see Section 4.3.1).

The localized C_{3v} symmetric equilibrium structure $\text{Cl}^- \cdots \text{CH}_3\text{Cl}$ (**1b**) is 5.7 kcal/mol more stable than the trigonal bipyramidal **1a** (see Figure 4.2). For the silicon system, there is no such stationary point corresponding to a localized structure $\text{Cl}^- \cdots \text{SiH}_3\text{Cl}$ with a short and a long Si–Cl bond. However, for the purpose of comparison, we have computed the geometry and energy of a localized $\text{Cl}^- \cdots \text{SiH}_3\text{Cl}$ species (**2b**) that, although it is not a stationary point, closely resembles $\text{Cl}^- \cdots \text{CH}_3\text{Cl}$ (**1b**) in that one Si–Cl bond has been elongated, relative to the pentavalent **2a**, by the same amount (i.e., by 0.7202 Å) as the long C–Cl bond in **1b** relative to the pentavalent **1a** (see Figure 4.1). Thus, **2b** is obtained through optimizing $\text{Cl}^- \cdots \text{SiH}_3\text{Cl}$ in C_{3v} symmetry with a long Si–Cl bond kept frozen at 3.0794 Å. This localized structure is 8.6 kcal/mol *higher* in energy than **2a** (see Figure 4.2). The other Si–Cl bond contracts, but only slightly so, from 2.3592 Å in **2a** to 2.1967 Å in **2b** (see Figure 4.2). Note that the short C–Cl bond in the corresponding carbon system undergoes a more pronounced contraction from 2.3516 Å in **1a** to 1.8720 Å in **1b**.

4.3.2 Bonding in $\text{Cl}-\text{AH}_3-\text{Cl}^-$

To understand this difference in bonding capabilities of carbon and silicon, we have analyzed the energy and bonding in ClCH_3Cl^- (**1**) and $\text{ClSiH}_3\text{Cl}^-$ (**2**) along a localization mode proceeding from the D_{3h} symmetric pentavalent species **1a** and **2a** towards the corresponding localized structures. This is done by expanding one of the Cl–A bonds in steps of 0.05 Å from

about 2.36 Å (**1a**: 2.3516 Å; **2a**: 2.3592 Å) to 2.5 Å while all remaining geometry parameters are allowed to relax, in particular, the other A–Cl bond which then contracts (i.e., localizes). The bonding in **1** and **2** is then examined, along this localization mode, by constructing either species stepwise from smaller molecular or atomic fragments and analyzing the bonding mechanism associated with bringing these fragments together. This can be done in various ways. In the following, we present three variants which shed light on the bonding in **1** and **2** from different, complementary perspectives.

First, we build Cl-AH₃-Cl⁻ stepwise from the central atom A^{***} in its *sp*³ valence state interacting with the Cl₂⁻ fragment of the two axial substituents (see Eq. 4.1a), followed by putting the resulting Cl-A-Cl^{***} together with the H₃^{***} fragment of the three equatorial substituents (see Eq. 4.1b and Figure 4.3):

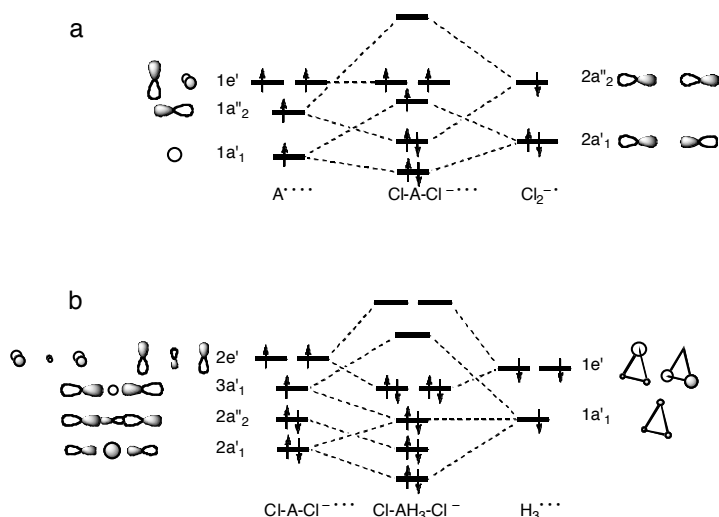


Figure 4.3 Schematic MO interaction diagram describing: (a) the interaction between central atom A^{***} and the axial substituents Cl₂⁻ in Cl-A-Cl^{***}; and (b) the interaction between Cl-A-Cl^{***} and the equatorial substituents H₃^{***} in D_{3h} symmetric Cl-AH₃-Cl⁻ (for the construction of H₃^{***} and Cl₂⁻, see Figure 4.6).

Alternatively, we build Cl-AH₃-Cl⁻ by first combining the central atom A^{***} with the H₃^{***} fragment of the three equatorial fragments (Eq. 4.2a) and *then* putting the resulting AH₃[•] together with the Cl₂⁻ fragment of the two axial substituents (see Eq. 4.2b and Figure 4.4):



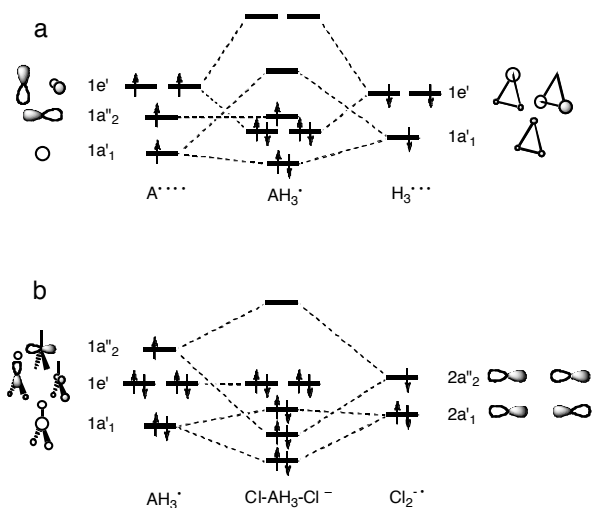


Figure 4.4 Schematic MO interaction diagram describing: (a) the interaction between central atom $A^{\bullet\bullet\bullet}$ and the equatorial substituents $H_3^{\bullet\bullet\bullet}$ in AH_3^{\bullet} ; and (b) the interaction between AH_3^{\bullet} and the axial substituents $Cl_2^{-\bullet}$ in D_{3h} symmetric $Cl-AH_3^{\bullet}-Cl^-$ (for the construction of $H_3^{\bullet\bullet\bullet}$ and $Cl_2^{-\bullet}$, see Figure 4.6).

The third variant is to construct $Cl-AH_3^{\bullet}-Cl^-$ from the $H_3^{\bullet\bullet\bullet}$ fragment of the three equatorial substituents interacting with the $Cl_2^{-\bullet}$ fragment of the two axial substituents (see Eq. 4.3a) and to put, thereafter, the central atom $A^{\bullet\bullet\bullet}$ into the resulting "cage" or "box" of substituents $Cl-H_3^{\bullet}-Cl^{-\bullet\bullet\bullet}$ (see Eq. 4.3b and Figure 4.5):

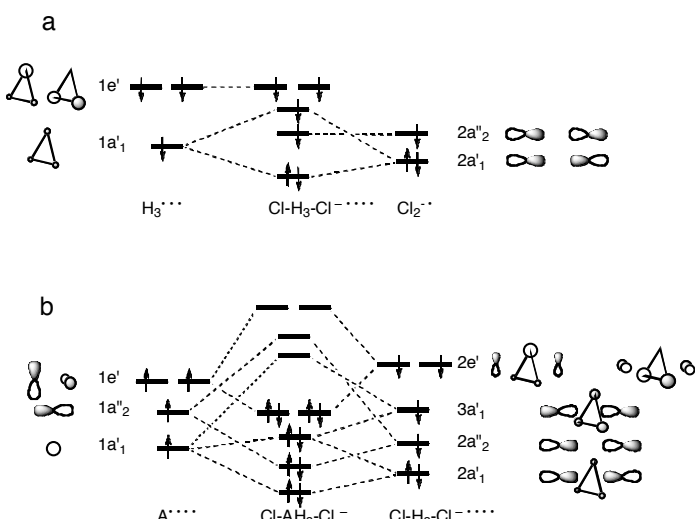


Figure 4.5 Schematic MO interaction diagram describing: (a) the interaction between the equatorial substituents $H_3^{\bullet\bullet\bullet}$ and the axial substituents $Cl_2^{-\bullet}$ in the "box" $Cl-H_3^{\bullet}-Cl^{-\bullet\bullet\bullet}$; and (b) the interaction between the central atom $A^{\bullet\bullet\bullet}$ and the "box" $Cl-H_3^{\bullet}-Cl^{-\bullet\bullet\bullet}$ in D_{3h} symmetric $Cl-AH_3^{\bullet}-Cl^-$ (for the construction of $H_3^{\bullet\bullet\bullet}$ and $Cl_2^{-\bullet}$, see Figure 4.6).

Note that all fragments in Eqs. 4.1 - 4.3 are in the valence configuration they adopt in the overall molecule (see also Figures 4.3 - 4.6), that unpaired electrons within one fragment are of the same spin whereas unpaired electrons on two different fragments are of opposite spin in order to enable the formation of the electron-pair bonds. Note also that in all three fragmentation modes, the fragments $\text{Cl}_2^{-\bullet}$ and $\text{H}_3^{\bullet\bullet\bullet}$ occur, which have been constructed from Cl^- interacting with Cl^\bullet and from three H^\bullet atoms, respectively (see also Figure 4.6). The results of the various analyses are collected in Figure 4.7.

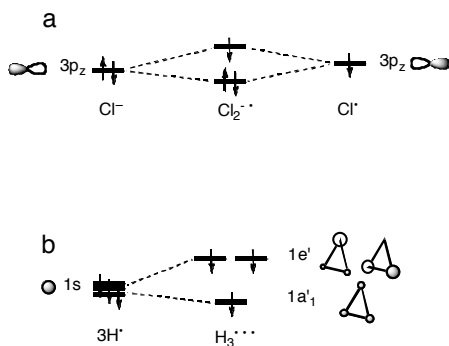


Figure 4.6 Schematic MO interaction diagram describing: (a) the interaction between Cl^- and Cl^\bullet in $\text{Cl}_2^{-\bullet}$; and (b) the interaction between three hydrogen atoms in $\text{H}_3^{\bullet\bullet\bullet}$.

The upper panel of Figure 4.7 (i.e., 3a-c) shows the analysis results for the three fragmentation modes of ClCH_3Cl^- (**1**), the lower panel (i.e., 3d-f) shows the results for $\text{ClSiH}_3\text{Cl}^-$ (**2**). To highlight the equivalence of the two A–Cl bonds, we show the evolution of all energy components from one localized starting point (with, say, the left A–Cl = 2.5 Å) to the D_{3h} symmetric, hypervalent species (both A–Cl \sim 2.36 Å) to the other localized structure (with, say, the right A–Cl = 2.5 Å). Based on the symmetry of the process, the right half of the graphs has been obtained as the mirror image of the left half. Energies are shown relative to the localized structures (A–Cl = 2.5 Å), i.e., the graphs show how the total energy of ClCH_3Cl^- and $\text{ClSiH}_3\text{Cl}^-$ (black lines, designated "total") as well as all the components associated with the steps defined in Eqs. 4.1 - 4.3 (colored and dashed lines) change relative to the localized starting point with A–Cl = 2.5 Å.

In the first place, we note that the analyses nicely reproduce the convex total energy profile for carbon (see Figures 4.7a-c) and the concave total energy surface for silicon as a central atom (see Figures 4.7d-f).^[27] Note that these total energy profiles are identical *within* the set of three graphs for **1**, and *within* the set of three graphs for **2**. And so are, of course, also the energy curves associated with the formation of $\text{Cl}_2^{-\bullet}$ from $\text{Cl}^- + \text{Cl}^\bullet$ and those for the formation of $\text{H}_3^{\bullet\bullet\bullet}$ from three H^\bullet (see Figure 4.6).

The latter are comparatively shallow, especially for $\text{ClSiH}_3\text{Cl}^-$, and are not decisive for the key difference between **1** and **2**, i.e., the convex and concave shape, respectively, of the total energy curve. The $\text{Cl}_2^{-\bullet}$ curve (short dashes) is in fact nearly constant because the overall

Cl–Cl distance is large and changes little as the contraction of one A–Cl bond always goes with the expansion of the other A–Cl bond. The $\text{H}_3\cdots$ curve (long dashes) is always stabilized at the symmetric, hypervalent structure. This is due to the fact that the AH_3 moiety goes from a pyramidal to a planar configuration in which the hydrogen atoms are slightly further away from each other and therefore experience less mutual steric (Pauli) repulsion.^[28] This effect is much more pronounced for ClCH_3Cl^- than for $\text{ClSiH}_3\text{Cl}^-$ because the hydrogen atoms in the former are in closer proximity due to the shorter C–H as compared to Si–H bonds.^[28]

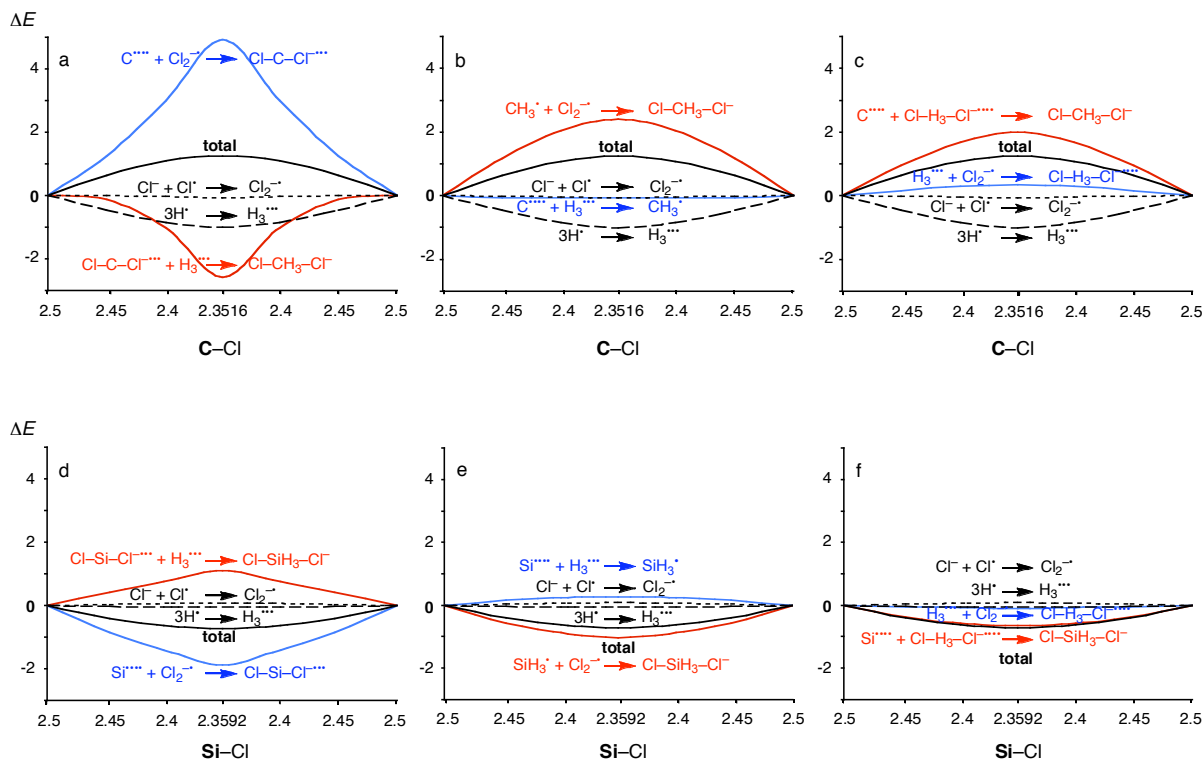


Figure 4.7 Three different decompositions (as indicated by partial reactions in a - c for carbon, and in d - f for silicon) of the relative energy in kcal/mol (bold black line, designated "total") of $[\text{ClCH}_3\text{Cl}]^-$ and $[\text{ClSiH}_3\text{Cl}]^-$ along an $\text{S}_{\text{N}}2$ -type deformation coordinate that brings the species from a localized C_{3v} structure via a D_{3h} symmetric and pentavalent species to the other localized structure. The deformation coordinate is defined by stepwise varying one C–Cl (or Si–Cl) bond from 2.5 to 2.3516 Å (or 2.3592 Å) and optimizing all other geometry parameters in every step.

Thus, the origin of **1a** being a transition state and **2a** a stable, hypervalent species is located somewhere in the other interaction steps, i.e., in the two steps (a) and (b) defined in each of the Eqs. 4.1 - 4.3 (see blue and red curves, respectively, in Figure 4.7). A closer inspection shows that in each of the three fragmentation modes the convex (**1**) or concave (**2**) nature of the total-energy curve is determined by the interaction of the central moiety (either A or AH_3) with the axial substituents (or all substituents simultaneously).

The effect as such and the difference between **1** and **2** are most pronounced for fragmentation mode number one, as defined in Eq. 4.1: as can be seen in Figures 4.7a and 4.7d, the interaction between carbon and the axial-substituents fragment in the Cl–C–Cl^{***} moiety of **1** is *destabilized* by nearly 5 kcal/mol as we go from the localized (C–Cl = 2.5 Å) to the symmetric, pentacoordinate structure **1a** (C–Cl ~ 2.36 Å), whereas the corresponding change in the interaction between silicon and the axial-substituents fragment in the Cl–Si–Cl^{***} moiety of **2** is a *stabilization* of -1.88 kcal/mol. Note that this behavior is counteracted, but not overruled, by the destabilization in the interaction with the equatorial H₃^{***} substituents (in line with the findings in Ref. [28]).

4.3.3 Bonding in Cl–A–Cl^{***}

The fact that Cl–C–Cl^{***} is labile with respect to bond localization is interesting. This species consists of three main group atoms with a 3c-4e bonding mechanism based on p_{σ} AOs (see Scheme 4.1). It is not only isostructural but also isoelectronic with the linear trihalides X–Y–X⁻ which are known to adopt a delocalized, hypervalent structure of D_{∞h} symmetry.^[21] In particular, Cl–F–Cl⁻ which, just as Cl–C–Cl^{***}, consists of an arrangement of two terminal chlorine atoms and a central second-period atom, is a stable D_{∞h} symmetric species with two equivalent Cl–F bonds of 2.0782 Å at the BP86/TZ2P level used in this investigation.

To further investigate this issue, we have computed the equilibrium geometries of Cl–C–Cl^{***} (**3a**) and Cl–Si–Cl^{***} (**4a**). Both species are found to possess linear, D_{∞h} symmetric equilibrium geometries with C–Cl and Si–Cl bond distances of 1.9784 Å (**3a**) and 2.2804 Å (**4a**), respectively (see Figure 4.8). Now, comparison with the corresponding C–Cl and Si–Cl distances in the pentacoordinate ClCH₃Cl⁻ (**1a**) and ClSiH₃Cl⁻ (**2a**) leads to a striking observation: the Si–Cl bond is not much different for the dicoordinate silicon in **4a** (2.2804 Å) than for the pentacoordinate silicon in **2a** (2.3592 Å); from the former to the latter, it expands by only 0.0788 Å or 3% (compare Figures 4.2 and 4.8). At variance, the C–Cl bond expands by a sizeable 0.3732 Å or 19% (!) if we go from dicoordinate carbon in **3a** (1.9784 Å) to pentacoordinate carbon in **1a** (2.3516 Å). Consequently, the C–Cl and Si–Cl bonds in **1a** and **2a** are in good approximation of equal length, as has been mentioned already above.

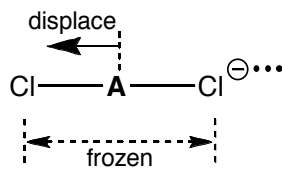


Figure 4.8 Geometries (in Å), relative energies (in kcal/mol) and number of imaginary frequencies (in parentheses) of ClCCl^{-3*} (**3a**) and ClSiCl^{-3*} (**4a**) computed at BP86/TZ2P.

Thus, in **1a**, the axial chlorine substituents can *not* approach the central carbon atom sufficiently closely to form the intrinsically optimal C–Cl bonds for the Cl–C–Cl^{***} moiety. In

2a, at variance, the axial chlorine substituents *can* approach the central silicon atom sufficiently closely to form the intrinsically optimal Si–Cl bonds for the Cl–Si–Cl^{−***} moiety. Consequently, the carbon atom in the Cl–C–Cl^{−***} fragment of **1a** moves closer to one of the two chlorine atoms to form one C–Cl strong bond at the expense of sacrificing one weak C–Cl bond. This is not necessary for the Cl–Si–Cl^{−***} fragment of **2a** in which the Si–Cl bonds have already nearly their optimal value.

This is nicely illustrated by Figure 4.9 which shows how the interaction between A^{−***} and Cl₂[−] (black line, designated "total") varies if the central atom A of a linear Cl–A–Cl^{−***} arrangement with a frozen Cl–Cl distance is displaced 0.5 Å (in steps of 0.1 Å) from the central position towards one of the terminal chlorine atoms frozen (see **IV**):



IV

This numerical experiment is carried out for: (i) Cl–C–Cl^{−***} with Cl–Cl = 2 × 2.3516 Å as in **1a**; (ii) for Cl–Si–Cl^{−***} with Cl–Cl = 2 × 2.3592 Å as in **2a**; and (iii) for Cl–C–Cl^{−***} with Cl–Cl = 2 × 1.9784 Å as in **3a**. For Cl–C–Cl^{−***} with the long Cl–Cl distance as in **1a**, the displacement of carbon away from the center and towards one of the chlorine atoms leads to a slight stabilization of −5.82 kcal/mol at a displacement of 0.5 Å (see Figure 4.9). Optimization, for this frozen Cl–Cl distance, yields a species with one C–Cl distance of 1.8285 Å and one of 2.8747 Å (not shown in the Figures). At variance, for Cl–Si–Cl^{−***} with the long Cl–Cl distance as in **2a**, the displacement of silicon away from the center and towards one of the chlorine atoms leads to a quite pronounced *destabilization* of +32 kcal/mol at a displacement of 0.5 Å. Once the Cl–Cl distance in Cl–C–Cl^{−***} adopts its intrinsically, i.e., for this species **3a**, optimal, somewhat shorter value, the interaction energy varies in the same manner as for Cl–Si–Cl^{−***}, i.e., it is destabilized by +29 kcal/mol at a displacement of 0.5 Å of the central carbon atom towards one of the terminal chlorine atoms.

The short C–Cl bond of 1.9784 Å in the Cl–C–Cl^{−***} species **3a** and the longer one of 2.3592 Å in the Cl–Si–Cl^{−***} species **4a** are nicely in line with the fact that the overlap between the more compact carbon 2p_z AO and the chloride 3p_z AO reaches its optimum of 0.270 at C–Cl = 1.88 Å whereas the overlap between the more diffuse silicon 3p_z AO and chloride 3p_z AO reaches its optimum of 0.299 already at a longer Si–Cl separation of 2.26 Å. Note that the optimum <2p_z|3p_z> and <3p_z|3p_z> distances are shorter than the actual optimum C–Cl and Si–Cl distances in **3a** and **4a**. This is, of course, due to the fact that the 3c–4e bonding in these species is somewhat more involved than in a diatomic species and because Pauli repulsion with closed valence and core shells of the other atom produce a longer

equilibrium distance compared to the fictitious situation with only bonding orbital interactions.^[29]

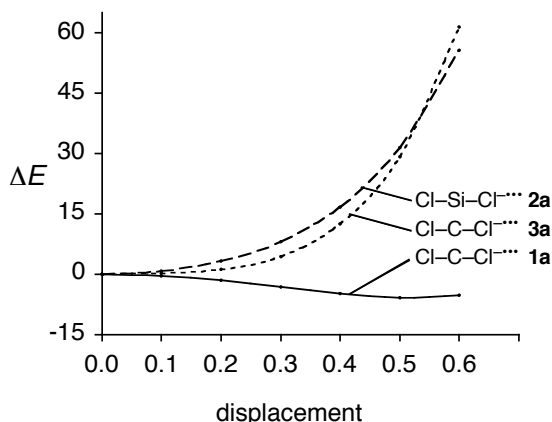


Figure 4.9 Interaction energy (in kcal/mol) between central atom A^{'''} and terminal substituents Cl₂⁻ for three Cl-A-Cl^{'''} fragments as a function of the displacement (in Å) of A towards one of the Cl atoms with the Cl-Cl distance kept frozen as shown in IV: (a) Cl-C-Cl^{'''} fragment taken from transition state **1a**; (b) Cl-Si-Cl^{'''} fragment taken from transition complex **2a**; (c) optimized Cl-C-Cl^{'''} species **3a**.

In the context of the above overlap considerations, it is interesting to examine the orbital contour diagrams in Figure 4.10. Therein, we have plotted the singly-occupied carbon 2p_z (left, in blue) and silicon 3p_z AOs (right, in red) located in between the lobes of the a₂" SOMO of the Cl-H₃-Cl^{'''} boxes of substituents (left and right, in black) in the geometries of the transition state **1a** and the transition complex **2a**, respectively. Note that the a₂" SOMO is mainly chlorine 3p_z – 3p_z. One can indeed recognize graphically that the overlap between the SOMOs in the silicon case is close to its optimum: the silicon 3p_z lobes have already nearly reached the nodal surfaces of the chlorine 3p_z AOs and further bond shortening is going to cause cancellation of overlap (see Figure 4.10, right). This is not the case with carbon as the central atom: the carbon 2p_z lobes can still gain more overlap with the 3p_z AOs if the distance C-Cl is shortened (see Figure 4.10, left). This can be related to the difference in size between these two atoms, silicon being more diffuse than carbon.^[28]

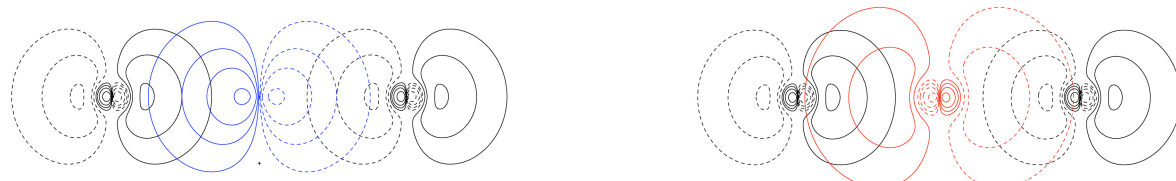


Figure 4.10 Contour plots of the singly-occupied carbon 2p_z (left, in blue) and silicon 3p_z AOs (right, in red) in between the chlorine 3p_z lobes (in black) of the a₂" SOMO of the "box" of substituents Cl-H₃-Cl^{'''} in the geometry of transition state **1a** and transition complex **2a**, respectively, computed at BP86/TZ2P (scan values: ±0.04, ±0.10, ±0.20, ±0.40, ±1.00).

4.3.4 The Central Atom as a Ball in a "Box" of Substituents

Thus, as a result of the "too long" and weak C–Cl bonds in D_{3h} symmetric ClCH_3Cl^- (**1a**), the system has the propensity to localize and strengthen one of them at the expense of breaking the other one. But why are the C–Cl bonds in **1a** too long in the first place, i.e., at 2.3516 Å instead of the 1.9784 Å which would be optimal for the isolated $\text{Cl}-\text{C}-\text{Cl}^{\bullet\bullet\bullet}$ unit?

To answer this question, we have added the three hydrogen atoms to the substituents fragment as the long C–Cl distances occur in the presence of these equatorial substituents. This yields the complete "box" of substituents $\text{Cl}-\text{H}_3-\text{Cl}^{\bullet\bullet\bullet}$. This corresponds to step 1 of the fragmentation scheme defined in Eq. 4.3. This box is as such not a stable species. But it does adopt an optimum geometry under constrained optimization within C_{3v} symmetry and a frozen H_3 unit. Interestingly, this yields a $\text{Cl}-\text{H}_3-\text{Cl}^{\bullet\bullet\bullet}$ structure that is very similar to the corresponding fragments in **1a** and **2a**: The distance between the Cl atoms and the empty central site (where otherwise C or Si are located) amounts to 2.4070 Å and 2.3166 Å in **5** and **6** in which the H_3 unit is taken from **1a** and **2a**, respectively (see Figure 4.11). This has to be compared with the nearly identical C–Cl and Si–Cl bond distances of 2.3516 and 2.3592 Å in **1a** and **2a** (see Figure 4.2).

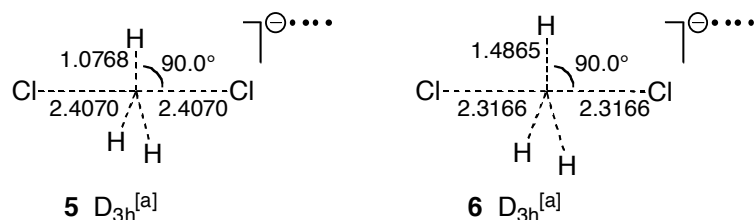
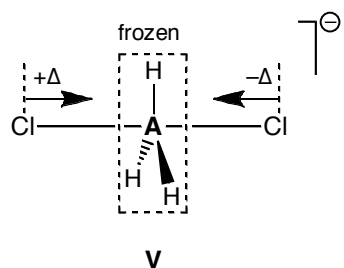


Figure 4.11 Geometries (in Å, deg.) of $\text{ClH}_3\text{Cl}^{\bullet\bullet\bullet}$ "boxes" of substituents (i.e., **5** and **6**), computed at BP86/TZ2P. ^[a] Optimized with frozen H_3 moiety (see Section 4.3.4).

The above finding is important: the box of substituents has an intrinsic optimum at the A–Cl distances of ca 2.36 Å found also in **1a** and **2a**. Further compressing the box increases its energy, although the associated potential energy surface (PES) is relatively shallow. This can be nicely recognized in a numerical experiment in which the axial chlorine substituents of the $\text{Cl}-\text{H}_3-\text{Cl}^{\bullet\bullet\bullet}$ box are symmetrically (i.e., preserving D_{3h} symmetry) compressed, in steps of 0.1 Å, from a distance of 2.5 to 1.9 Å with a frozen H_3 unit as shown in V:



The results are visualized in Figure 4.12 with the carbon and silicon systems to the left and to the right, respectively. Along the compression, the substituent–substituent interaction in the box goes through a minimum at 2.3 - 2.4 Å and is then destabilized as the Cl–H distance is further reduced (see Figure 4.12, red lines, carbon and silicon cases are left and right, respectively). This resistance towards compression is of course much increased if the central atom is introduced in the overall ClAH_3Cl^- systems (bold black lines in Figure 4.12). This is due to the additional Cl–C or Cl–Si repulsion (on top of the Cl–H repulsion) which destabilizes the interaction between the central atom and the axial substituents at shorter distances (blue lines in Figure 4.12). Thus, steric factors prevent the box of substituents to get more compact than it is in either **1a** and **2a**, even in the absence of the central atom, yielding substituent boxes of very similar geometrical dimensions for both carbon and silicon (see Figures 4.2 and 4.11).

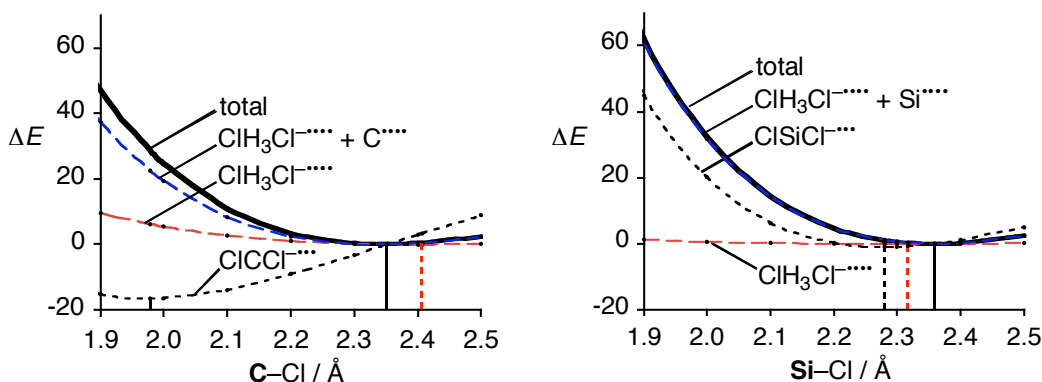


Figure 4.12 Energy (in kcal/mol) of D_{3h} symmetric ClCH_3Cl^- (left) and $\text{ClSiH}_3\text{Cl}^-$ (right) relative to transition state **1a** and transition complex **2a**, respectively, as a function of the Cl–Cl distance (see also V), computed at BP86/TZ2P. Relative energies of the overall species ClAH_3Cl^- (bold lines, designated "total") are decomposed into the relative energy of the "box" of substituent $\text{Cl}-\text{H}_3-\text{Cl}^{\cdots\cdots}$ (red dashed lines) plus the interaction between this "box" and the central atom A (blue dashed lines). Furthermore, the relative energy of $\text{Cl}-\text{C}-\text{Cl}^{\cdots\cdots}$ (left) and $\text{Cl}-\text{Si}-\text{Cl}^{\cdots\cdots}$ (right) is indicated (black dashed lines). Vertical lines indicate the energy minimum for the corresponding energy curve.

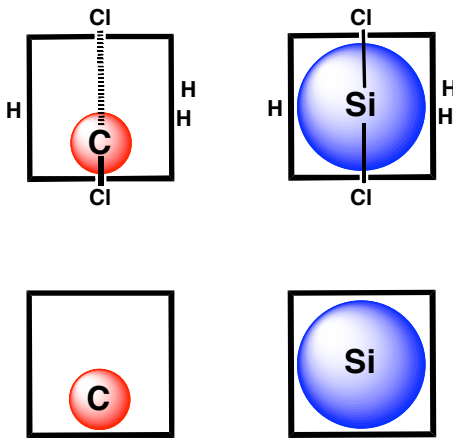
The optimum "box size" of the silicon species (Figure 4.12, right) is more or less the same for the isolated box $\text{Cl}-\text{H}_3-\text{Cl}^{\cdots\cdots}$ (red vertical line), for the interaction of $\text{A}^{\cdots\cdots} + \text{Cl}-\text{H}_3-\text{Cl}^{\cdots\cdots}$ and for the overall system $\text{Cl}-\text{SiH}_3-\text{Cl}^-$ (black vertical line). Interestingly, it is also more or less the same for the $\text{Cl}-\text{Si}-\text{Cl}^{\cdots\cdots}$ species (dashed black vertical line). Thus, both steric factors and Si–Cl bonding interactions ("electronic factors") favor a substituent box of approximately the same size leading to a stable symmetric structure **2a** for $\text{ClSiH}_3\text{Cl}^-$.

The situation is qualitatively different for the carbon species (Figure 4.12, left). The optimum "box size" is still more or less the same for the isolated box $\text{Cl}-\text{H}_3-\text{Cl}^{\cdots\cdots}$ (red vertical line), for the interaction of $\text{A}^{\cdots\cdots} + \text{Cl}-\text{H}_3-\text{Cl}^{\cdots\cdots}$ and for the overall system $\text{Cl}-\text{CH}_3-\text{Cl}^-$

(black vertical line). Strikingly, although in line with the above analyses of the Cl–A–Cl^{···} species, the optimum "box size", here, is at much shorter Cl–Cl distance for the Cl–C–Cl^{···} species (*dashed* black vertical line). We recall that the energy curves in Figure 4.12 refer to *symmetric* Cl–Cl variation, i.e., not to localization modes as shown in Figures 4.7 and 4.9. The consequence of the counteracting tendencies in Cl–CH₃–Cl[−] of having a large Cl–H₃–Cl^{···} but striving for short C–Cl bonds in Cl–C–Cl^{···} is that, if one lifts this symmetry constraint, the C–Cl bonds localize while simultaneously the size of the Cl–H₃–Cl^{···} box is more or less preserved. In line with this, optimization of ClCH₃Cl[−] structure **1a** with a frozen [Cl–H₃–Cl] moiety but an unconstrained carbon atom yields a localized structure at −1.2 kcal/mol with C–Cl bonds of 2.09 and 2.61 Å. Thus, whereas steric factors still lead to a large substituent box, C–Cl bonding interactions ("electronic factors") favor shorter C–Cl bonds leading to a localized structure **1b** for ClCH₃Cl[−].

The qualitative picture that emerges from our MO analyses is that the five substituents form a cage or "box" ClH₃Cl[−] in which they are in mutual steric contact (see Scheme 4.2). The central atom A can be viewed as a "ball" in that box. Silicon fits nearly exactly into the box and can bind simultaneously to the top and the bottom (see Scheme 4.2). This yields the hypervalent ClSiH₃Cl[−] with a trigonal-bipyramidal structure. At variance, the carbon atom is too small to touch both the top and the bottom and it can thus only bind to one of them (see Scheme 4.2). This leads to a species Cl[−]---H₃CCl with one localized C–Cl bond, one long C–Cl contact, and a pyramidalized CH₃ unit.

Scheme 4.2 "Ball-in-a-box" model for five-coordinate carbon and silicon

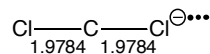


We have generalized our findings for ClCH₃Cl[−] and ClSiH₃Cl[−] to other group-14 central atoms (Ge, Sn and Pb) and axial substituents (F). Thus, D_{3h} symmetric FCH₃F[−] and FSiH₃F[−] are a labile transition state and a stable trigonal bipyramidal complex, respectively. In nice agreement with the above analyses, we find again that the C–F bond length in D_{3h} symmetric FCH₃F[−] (1.8538 Å) is much longer than its intrinsic optimum as given by the D_{∞h} symmetric equilibrium structure of F–C–F^{···} (1.5937 Å). Furthermore, all of the heavier ClAH₃Cl[−] analogs (A = Ge, Sn, Pb) have stable D_{3h} symmetric equilibrium structures, just as ClSiH₃Cl[−].

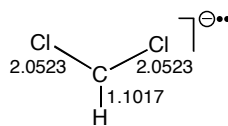
And, again in nice agreement with the above analyses, we find that the A–Cl bond length in D_{3h} symmetric ClAH_3Cl^- (2.4928, 2.6208 and 2.7346 Å for A = Ge, Sn, Pb) is quite close to its intrinsic optimum as given by the $D_{\infty h}$ symmetric equilibrium structure of $\text{Cl}-\text{A}-\text{Cl}^{\bullet\bullet\bullet}$ (2.4048, 2.5758 and 2.7184 Å for A = Ge, Sn, Pb).

4.3.5 Nucleophilic Substitution at Carbon without a Barrier

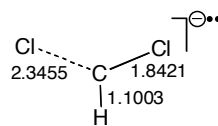
The ball-in-a-box model is further consolidating earlier reports that highlight the steric nature of the central barrier in S_N2 reactions.^[16a,b] This has prompted us to carry out one more numerical experiment. If steric congestion around the central atom plays a prominent role, the central S_N2 barrier should be lowered if we reduce the number of substituents. Indeed, this is exactly what happens in the series of nucleophilic substitutions at carbon ($S_N2@C$) in the series of model reactions shown in Eq. 4.4a-d:



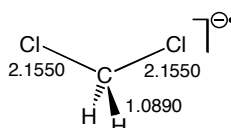
3a $D_{\infty h}(0)$



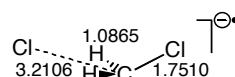
7a $C_{2v}\ 0.0\ (1)^{[a]}$



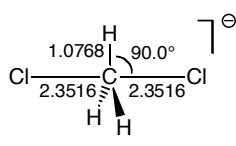
7b $C_s\ -0.50\ (0)$



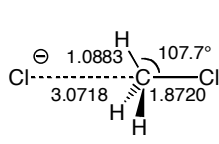
8a $C_{2v}\ 0.0\ (1)^{[b]}$



8b $C_s\ -5.18\ (1)^{[c]}$



1a $D_{3h}\ 0.0\ (1)^{[d]}$



1b $C_{3v}\ -5.66\ (0)$

Figure 4.13 Geometries (in Å, deg.), relative energies (in kcal/mol) and number of imaginary frequencies (in parentheses) of selected $\text{ClCH}_n\text{Cl}^{(3-n)\bullet}$ structures with n = 0, 1, 2 and 3 (i.e., **3a**, **7**, **8** and **1**, respectively) computed at BP86/TZ2P. ^[a] i198 cm⁻¹. ^[b] i271 cm⁻¹. ^[c] i111 cm⁻¹. ^[d] i316 cm⁻¹.

Along reactions 4.4a-d, the number of equatorial hydrogen substituents in the transition structure decreases from $n = 3$ to 2 to 1 to 0. And, as expected, the barrier decreases systematically from 5.7 to 5.2 to 0.5 to 0 kcal/mol (see Figure 4.13). Furthermore, in line with the systematic reduction in barrier height, the C–Cl bonds in the symmetric transition structure contracts from 2.3516 Å (**1a**) to 2.1550 Å (**8a**) to 2.0523 Å (**7a**) to 1.9784 Å (**3a**), as can be seen in Figure 4.13.

4.4 Conclusions

Based on quantitative MO theory, we have developed here the qualitative "ball-in-a-box" model for understanding *why* certain atoms A (such as silicon) *can* form stable hypervalent configurations ClAH_3Cl^- while others (such as carbon) *can not*. The qualitative picture that emerges from our MO analyses is that the five substituents form a cage or "box" ClH_3Cl^- in which they are in mutual steric contact (if the substituents are forced at a closer mutual distance, they begin to strongly repel each other). The central atom A can be viewed as a "ball" in that box.

Silicon fits nearly exactly into the box and can bind simultaneously to the top and the bottom. This yields the hypervalent $\text{ClSiH}_3\text{Cl}^-$ with a trigonal-bipyramidal structure. At variance, the carbon atom is too small to touch both the top and the bottom and it can thus only bind to one of them. To somewhat stretch the qualitative picture, one could say that the carbon-atom ball "drops" onto the bottom of the box (Scheme 4.2) leading, consequently, to a species $\text{Cl}^- \cdots \text{H}_3\text{CCl}$ with one localized C–Cl bond, one long C–Cl contact, and a pyramidalized CH_3 unit. Our findings for ClCH_3Cl^- and $\text{ClSiH}_3\text{Cl}^-$ have been generalized to other group-14 central atoms (Ge, Sn and Pb) and another axial substituent (F). The ball-in-a-box model is furthermore supported by the fact that the $\text{S}_{\text{N}}2$ central barrier for nucleophilic attack by Cl^- decreases monotonically along the substrates CH_3Cl , $^{\bullet}\text{CH}_2\text{Cl}$, $^{\bullet\bullet}\text{CHCl}$ and $^{\bullet\bullet\bullet}\text{CCl}$.

In a sense, the ball-in-a-box model makes MO theory catch up with VB theory regarding the treatment and understanding of the phenomenon of hypervalence. It also nicely integrates bonding orbital interactions ("electronic factors") and repulsive orbital interactions ("steric factors") into one qualitative model. This highlights the importance of the relative size of the central atom for the capability to form hypervalent compounds.^[4,13,15]

References

- [1] G. N. Lewis, *J. Am. Chem. Soc.* **1916**, *38*, 762.
- [2] (a) K. Y. Akiba in *Chemistry of Hypervalent Compounds* (K. Y. Akiba, Ed.); Wiley-VCH: New York, **1998**, Chapters 1 and 2; (b) C. Chuit, R. J. P. Corriu, C. Reye in *Chemistry of Hypervalent Compounds* (K. Y. Akiba, Ed.); Wiley-VCH: New York, **1998**, Chapter 4.
- [3] (a) R. Hoffmann, *Solids and Surfaces: A Chemist's View of Bonding in Extended Structures*; John Wiley & Sons Inc: New York, **1989**; (b) J. I. Musher, *Angew. Chem.* **1969**, *81*, 68; *Angew.*

- Chem. Int. Ed. Engl.* **1969**, 8, 54; (c) L. Pauling, *The Nature of the Chemical Bond*; 3rd ed., Cornell University Press: Ithaca: New York, **1960**.
- [4] (a) S. Noury, B. Silvi, R. J. Gillespie, *Inorg. Chem.* **2002**, 41, 2164; (b) R. J. Gillespie, E. A. Robinson, *Inorg. Chem.* **1995**, 34, 978.
- [5] J. Cioslowski, S. T. Mixon, *Inorg. Chem.* **1993**, 32, 3209.
- [6] (a) M. B. Smith, J. March, *Advanced Organic Chemistry: Reactions, Mechanisms and Structure*; Wiley-Interscience: New York, **2001**; (b) F. A. Carey, R. J. Sundberg, *Advanced Organic Chemistry: Structure And Mechanisms (Part A)*; Springer: New York, **2000**; (c) A. Streitwieser, C. H. Heathcock, E. M. Kosower, *Introduction to Organic Chemistry*; Prentice Hall: Paramus, **1998**.
- [7] (a) K. Y. Akiba, Y. Moriyama, M. Mizozoe, H. Inohara, T. Nishii, Y. Yamamoto, M. Minoura, D. Hashizume, F. Iwasaki, N. Takagi, K. Ishimura, S. Nagase, *J. Am. Chem. Soc.* **2005**, 127, 5893; (b) K. Y. Akiba, M. Yamashita, Y. Yamamoto, S. Nagase, *J. Am. Chem. Soc.* **1999**, 121, 10644; (c) G. A. Olah, G. K. S. Prakash, R. E. Williams, L. D. Field, K. Wade, *Hypercarbon chemistry*; John Wiley & Sons Inc: New York, **1987**; (d) T. R. Forbus, J. C. Martin, *J. Am. Chem. Soc.* **1979**, 101, 5057.
- [8] J. C. Martin, *Science* **1983**, 221, 509.
- [9] D. J. Hajdasz, R. R. Squires, *J. Am. Chem. Soc.* **1986**, 108, 3139.
- [10] (a) G. L. Gutsev, *Chem. Phys. Lett.* **1991**, 184, 305; (b) W. C. Hamilton, *Acta Crystallographica* **1962**, 15, 353.
- [11] (a) J. K. Laerdahl, E. Uggerud, *Int. J. Mass. Spectrom.* **2002**, 214, 277; (b) M. N. Glukhovtsev, A. Pross, L. Radom, *J. Am. Chem. Soc.* **1996**, 118, 6273; (c) S. S. Shaik, H. B. Schlegel, S. Wolfe, *Theoretical aspects of physical organic chemistry: the S_N2 mechanism*; John Wiley & Sons Inc: New York, **1992**; (d) G. L. Gutsev, *Chem. Phys.* **1992**, 166, 57; (e) Z. Shi, R. J. Boyd, *J. Phys. Chem.* **1991**, 95, 4698; (f) R. Vetter, L. Zulicke, *J. Am. Chem. Soc.* **1990**, 112, 5136; (g) S. C. Tucker, D. G. Truhlar, *J. Phys. Chem.* **1989**, 93, 8138; (h) S. Wolfe, D. J. Mitchell, H. B. Schlegel, *J. Am. Chem. Soc.* **1981**, 103, 7692; (i) J. D. Payzant, K. Tanaka, L. D. Betowski, D. K. Bohme, *J. Am. Chem. Soc.* **1976**, 98, 894; (j) F. Keil, R. Ahlrichs, *J. Am. Chem. Soc.* **1976**, 98, 4787; (k) R. F. W. Bader, A. J. Duke, R. R. Messer, *J. Am. Chem. Soc.* **1973**, 95, 7715; (l) A. Dedieu, A. Veillard, *J. Am. Chem. Soc.* **1972**, 94, 6730; (m) C. D. Ritchie, G. A. Chappell, *J. Am. Chem. Soc.* **1970**, 92, 1819.
- [12] W. N. Olmstead, J. I. Brauman, *J. Am. Chem. Soc.* **1977**, 99, 4219.
- [13] M. J. S. Dewar, E. Healy, *Organometallics* **1982**, 1, 1705.
- [14] (a) G. L. Gutsev, *J. Phys. Chem.* **1994**, 98, 1570; (b) M. T. Carroll, M. S. Gordon, T. L. Windus, *Inorg. Chem.* **1992**, 31, 825; (c) S. Gronert, R. Glaser, A. Streitwieser, *J. Am. Chem. Soc.* **1989**, 111, 3111; (d) N. T. Anh, C. Minot, *J. Am. Chem. Soc.* **1980**, 102, 103; (e) P. Baybutt, *Mol. Phys.* **1975**, 29, 389; (f) F. Keil, R. Ahlrichs, *Chem. Phys.* **1975**, 8, 384; (g) D. L. Wilhite, L. Spialter, *J. Am. Chem. Soc.* **1973**, 95, 2100.
- [15] A. E. Reed, P. v. R. Schleyer, *Chem. Phys. Lett.* **1987**, 133, 553.
- [16] (a) A. P. Bento, F. M. Bickelhaupt, *J. Org. Chem.* **2007**, 72, 2201. See also: (b) M. A. van Bochove, M. Swart, F. M. Bickelhaupt, *J. Am. Chem. Soc.* **2006**, 128, 10738; (c) A. P. Bento, M. Solà, F. M. Bickelhaupt, *J. Comput. Chem.* **2005**, 26, 1497.
- [17] (a) G. te Velde, F. M. Bickelhaupt, E. J. Baerends, C. Fonseca Guerra, S. J. A. van Gisbergen, J. G. Snijders, T. Ziegler, *J. Comput. Chem.* **2001**, 22, 931; (b) C. Fonseca Guerra, O. Visser, J. G. Snijders, G. te Velde, E. J. Baerends, in *Methods and Techniques for Computational Chemistry*, (Eds.: E. Clementi, G. Corongiu), STEF: Cagliari, **1995**, p. 305-395; (c) E. J. Baerends, D. E. Ellis, P. Ros, *Chem. Phys.* **1973**, 2, 41; (d) E. J. Baerends, P. Ros, *Chem. Phys.* **1975**, 8, 412; (e) E. J. Baerends, P. Ros, *Int. J. Quantum. Chem. Symp.* **1978**, 12, 169; (f) C. Fonseca Guerra, J. G. Snijders, G. te Velde, E. J. Baerends, *Theor. Chem. Acc.* **1998**, 99, 391; (g) P. M. Boerriger, G.

- te Velde, E. J. Baerends, *Int. J. Quantum Chem.* **1988**, *33*, 87; (h) G. te Velde, E. J. Baerends, *J. Comp. Phys.* **1992**, *99*, 84; (i) J. G. Snijders, E. J. Baerends, P. Vernooijs, *At. Nucl. Data Tables* **1982**, *26*, 483; (j) J. Krijn, E. J. Baerends, *Fit-Functions in the HFS-Method; Internal Report (in Dutch)*, Vrije Universiteit, Amsterdam, **1984**; (k) L. Versluis, T. Ziegler, *J. Chem. Phys.* **1988**, *88*, 322; (l) J. C. Slater, *Quantum Theory of Molecules and Solids, Vol. 4*, McGraw-Hill, New York, **1974**; (m) A. D. Becke, *J. Chem. Phys.* **1986**, *84*, 4524; (n) A. Becke, *Phys. Rev. A* **1988**, *38*, 3098; (o) S. H. Vosko, L. Wilk, M. Nusair, *Can. J. Phys.* **1980**, *58*, 1200; (p) J. P. Perdew, *Phys. Rev. B* **1986**, *33*, 8822 (Erratum: *Phys. Rev. B* **1986**, *34*, 7406); (q) L. Fan, T. Ziegler, *J. Chem. Phys.* **1991**, *94*, 6057; (r) E. van Lenthe, E. J. Baerends, J. G. Snijders, *J. Chem. Phys.* **1994**, *101*, 9783.
- [18] (a) F. M. Bickelhaupt, E. J. Baerends, Kohn-Sham density functional theory: Predicting and understanding chemistry. In *Reviews In Computational Chemistry*, **2000**; Vol. 15; pp 1. For the analysis of electron-pair (2c-2e) bonds see: (b) F. M. Bickelhaupt, N. M. M. Nibbering, E. M. van Wezenbeek, E. J. Baerends, *J. Phys. Chem.* **1992**, *96*, 4864; for the analysis of 2c-3e bonds see: (c) F. M. Bickelhaupt, A. Diefenbach, S. P. de Visser, L. J. de Koning, N. M. M. Nibbering, *J. Phys. Chem. A* **1998**, *102*, 9549.
- [19] R. Hoffmann, J. M. Howell, E. L. Muetterties, *J. Am. Chem. Soc.* **1972**, *94*, 3047.
- [20] (a) G. C. Pimentel, *J. Chem. Phys.* **1951**, *19*, 446; (b) R. J. Hach, R. E. Rundle, *J. Am. Chem. Soc.* **1951**, *73*, 4321.
- [21] G. A. Landrum, N. Goldberg, R. Hoffmann, *J. Chem. Soc. Dalton Trans.* **1997**, 3605.
- [22] (a) C. A. Ramsden, *Chem. Soc. Rev.* **1994**, *23*, 111; (b) T. A. Albright, J. K. Burdett, M.-H. Whangbo, *Orbital Interactions in Chemistry*; John Wiley & Sons Inc: New-York, **1985**.
- [23] (a) A. E. Reed, P. v. R. Schleyer, *J. Am. Chem. Soc.* **1990**, *112*, 1434; (b) E. Magnusson, *J. Am. Chem. Soc.* **1990**, *112*, 7940; (c) W. Kutzelnigg, *Angew. Chem.* **1984**, *96*, 262; *Angew. Chem. Int. Ed. Engl.* **1984**, *23*, 272.
- [24] (a) S. Shaik, A. Shurki, *Angew. Chem.* **1999**, *111*, 616; *Angew. Chem. Int. Ed. Engl.* **1999**, *38*, 587; (b) P. C. Hiberty, *J. Mol. Struct. (THEOCHEM)* **1998**, *451*, 237; (c) G. Sini, G. Ohanessian, P. C. Hiberty, S. S. Shaik, *J. Am. Chem. Soc.* **1990**, *112*, 1407; (d) G. Sini, P. C. Hiberty, S. S. Shaik, *J. Chem. Soc. Chem. Comm.* **1989**, 772.
- [25] (a) T. Ziegler, A. Rauk, *Inorg. Chem.* **1979**, *18*, 1755; (b) T. Ziegler, A. Rauk, *Inorg. Chem.* **1979**, *18*, 1558; (c) T. Ziegler, A. Rauk, *Theor. Chim. Acta* **1977**, *46*, 1.
- [26] (a) K. Kitaura, K. Morokuma, *Int. J. Quantum Chem.* **1976**, *10*, 325; (b) K. Morokuma, *J. Chem. Phys.* **1971**, *55*, 1236.
- [27] These energy profiles closely resemble but are not exactly identical to the minimum energy profiles corresponding to the internal reaction coordinate as defined in K. Fukui, *Acc. Chem. Res.* **1981**, *14*, 363.
- [28] F. M. Bickelhaupt, T. Ziegler, P. v. R. Schleyer, *Organometallics* **1996**, *15*, 1477.
- [29] (a) M. L. Munzarová, R. Hoffmann, *J. Am. Chem. Soc.* **2002**, *124*, 4787; (b) F. M. Bickelhaupt, R. L. DeKock, E. J. Baerends, *J. Am. Chem. Soc.* **2002**, *124*, 1500.

5 Hypervalent *versus* Nonhypervalent Carbon in Noble-Gas Complexes

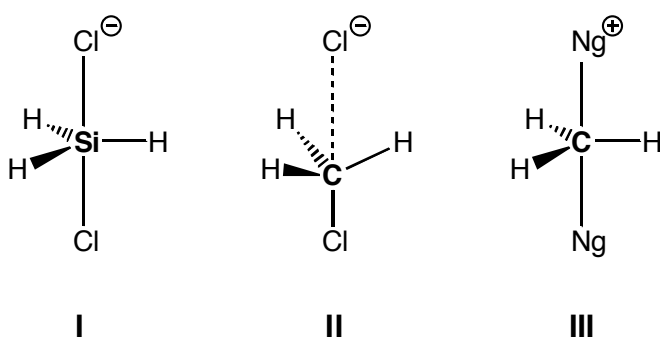
Adapted from S. C. A. H. Pierrefixe, J. Poater, C. Im, F. M. Bickelhaupt
Chem. Eur. J. **2008** Accepted

Abstract

Silicon in $[\text{Cl}-\text{SiH}_3-\text{Cl}]^-$ is hypervalent whereas carbon in $[\text{Cl}-\text{CH}_3-\text{Cl}]^-$ is not. We have recently shown how this can be understood in terms of the ball-in-a-box model according to which silicon fits perfectly into the box that is constituted by the five substituents, while carbon is too small and, in a sense, "drops to the bottom" of the box. But how does carbon acquire hypervalency in the isostructural and isoelectronic noble gas-methyl cation complexes $[\text{Ng}-\text{CH}_3-\text{Ng}]^+$, which feature a delocalized D_{3h} symmetric structure with two equivalent C-Ng bonds? That is, for Ng = He and Ne. From Ng = Ar, the $[\text{Ng}-\text{CH}_3-\text{Ng}]^+$ complex acquires again a propensity to localize one of its axial C-Ng bonds and to largely break the other one, and this propensity increases along Ng = Ar, Kr, Xe and Rn. The behavior of the helium and neon complexes violates the ball-in-a-box principle! Why does this happen? The purpose of this study is to answer these questions and to understand why carbon can become truly hypervalent under certain conditions. To this end, we have carefully analyzed the structure and bonding in NgCH_3Ng^+ and, for comparison, CH_3Ng^+ , NgHNg^+ and NgH^+ . It appears that, at variance with $[\text{Cl}-\text{CH}_3-\text{Cl}]^-$, the carbon atom in $[\text{Ng}-\text{CH}_3-\text{Ng}]^+$ can no longer be considered as a ball in a box of the five substituents.

5.1 Introduction

Silicon in $[\text{Cl}-\text{SiH}_3-\text{Cl}]^-$ is hypervalent whereas carbon in $[\text{Cl}-\text{CH}_3-\text{Cl}]^-$ is not. This is well known.^[1-3] Very recently, we have explained this difference in valency in terms of the ball-in-a-box model.^[1] In this model, the five substituents form a cage or "box" ClH_3Cl^- in which they are in mutual steric contact. The central atom A can be viewed as a "ball" in that box. Silicon fits perfectly into the box that is constituted by the five substituents yielding a hypervalent configuration with delocalized, equivalent Si–Cl bonds (**I**). The carbon atom, on the other hand, is too small and, in a sense, "drops to the bottom" of the box leading, consequently, to a species $\text{Cl}^- \cdots \text{H}_3\text{CCl}$ with one localized C–Cl bond, one long C–Cl contact, and a pyramidalized CH_3 unit (**II**). Our findings for ClCH_3Cl^- and $\text{ClSiH}_3\text{Cl}^-$ have been generalized to other group-14 central atoms (Ge, Sn and Pb) and another axial substituent (F).^[1]



But why then does carbon become a hypervalent atom in the isostructural and isoelectronic noble gas–methyl cation complexes $[\text{Ng}-\text{CH}_3-\text{Ng}]^+$,^[4] which feature delocalized D_{3h} symmetric structure with two equivalent C–Ng bonds (**III**)? That is, for $\text{Ng} = \text{He}$ and Ne .^[4a] For $\text{Ng} = \text{Ar}$, the $[\text{Ng}-\text{CH}_3-\text{Ng}]^+$ complex acquires again a propensity to localize one of its axial C–Ng bonds and to largely break the other one.^[4a] Why is that so? And does this localizing propensity persist or, possibly, further increase along $\text{Ng} = \text{Ar}, \text{Kr}, \text{Xe}$ and Rn ?

The purpose of this study is to answer the above questions and to understand why carbon can become truly hypervalent under certain conditions. To this end, we have carefully analyzed the structure and bonding in NgCH_3Ng^+ and, for comparison, CH_3Ng^+ , NgHNg^+ and NgH^+ . This was done using density functional theory (DFT), with relativistic corrections for species involving Kr, Xe and Rn, as implemented in the ADF program.^[5,6] The bonding analyses consist of a decomposition of the total bond energy into interaction energies between fragments of the overall model systems, e.g., methyl cation + noble gas. The trends in the various energy terms are interpreted in the conceptual framework provided by the quantitative molecular orbital (MO) model contained in Kohn-Sham DFT.^[7] We compare the results of the present analyses of noble-gas complexes NgCH_3Ng^+ with those previously obtained for the halogen-substituted XCH_3X^- and XSiH_3X^- species.^[1]

In addition, to validate our DFT approach, we have first computed accurate *ab initio* benchmarks for the helium, neon and argon complexes using a hierarchical series of *ab initio*

methods up to CCSD(T).^[8] The *ab initio* calculations were carried out with the Gaussian program^[9] and they support our DFT approach.

Interestingly, it appears that, at variance with the situation of $[\text{Cl}-\text{CH}_3-\text{Cl}]^-$, the carbon atom in $[\text{Ng}-\text{CH}_3-\text{Ng}]^+$ can no longer be considered as a ball in a box of the five substituents. Instead, the $[\text{Ng}-\text{CH}_3-\text{Ng}]^+$ species are better conceived as a "disk between balls". Here, the "disk" is CH_3^+ and the "balls" are constituted by the two noble-gas atoms. We propose a spectrum of five-coordinate carbon species that ranges from the ball-in-a-box situation to the disk-between-balls model, depending on the ratio of bond strengths between carbon–axial versus carbon–equatorial substituents.

5.2 Theoretical Methods

5.2.1 DFT Computations

DFT calculations were performed for all species using the Amsterdam Density Functional (ADF) program developed by Baerends and others^[5] with the OLYP and BP86 functionals^[6] that were used in combination with the TZ2P basis set, which is a large uncontracted set of Slater-type orbitals (STOs) containing diffuse functions. This basis set of triple- ζ quality for all atoms has been augmented with two sets of polarization functions, i.e. $2p$ and $3d$ on H and He, $3d$ and $4f$ on C, Ne and Ar, $4d$ and $4f$ on Kr, $5d$ and $4f$ on Xe and $6d$ and $5f$ on Rn. The core shells of carbon and neon ($1s$), argon ($1s2s2p$), krypton ($1s2s2p3s3p$), xenon ($1s2s2p3s3p4s3d4p$) and of radon ($1s2s2p3s3p4s3d4p5s4d5p$) were treated by the frozen-core approximation. An auxiliary set of s , p , d , f and g STOs was used to fit the molecular density and to represent the Coulomb and exchange potentials accurately in each self-consistent field cycle. Relativistic effects were taken into account in calculations of species involving Kr, Xe or Rn atoms using the zeroth-order regular approximation (ZORA).^[5c] All stationary points were confirmed to be equilibrium structures (no imaginary frequency) or transition states (one imaginary frequency) through vibrational analysis.

5.2.2 Ab Initio Calculations

Ab initio calculations were carried out for NgCH_3Ng^+ and CH_3Ng^+ ($\text{Ng} = \text{He}, \text{Ne}, \text{Ar}$) with the Gaussian program^[9] using the a hierarchical series of methods: Møller-Plesset perturbation theory^[8a] through second-order (MP2) and fourth-order (MP4) and coupled-cluster theory^[8b] with single and double excitations as well as and triple excitations treated perturbatively [CCSD(T)].^[8c] These calculations were done using Pople's 6-311++G** basis set^[10] at each level of theory and Dunning's correlation consistent polarized valence basis set of triple- ζ quality (cc-pVTZ)^[11] at MP2 and MP4. The geometries for the ArCH_3Ar^+ systems were, due to the enormous computational demand, all optimized at MP2/6-311++G**. Energies at a higher level of theory are, for these species, computed in a single-point fashion

using the MP2/6-311++G** geometries. This approach was verified for the CH_3Ar^+ system to yield deviations in relative energies of only a few hundredths of a kcal/mol.

5.2.3 Bond Analyses

To gain more insights into the nature of the bonding in our noble gas–methyl cation complexes, an energy decomposition analysis has been carried out.^[7] In this analysis, the total binding energy ΔE associated with forming the overall molecular species of interest, say AB, from two fragments, A' + B', is made up of two major components (Eq. 5.1):

$$\Delta E = \Delta E_{\text{prep}} + \Delta E_{\text{int}} \quad (5.1)$$

In this formula, the preparation energy ΔE_{prep} is the amount of energy required to deform the individual (isolated) fragments from their equilibrium structure (A', B') to the geometry that they acquire in the overall molecule (A, B). The interaction energy ΔE_{int} corresponds to the actual energy change when these geometrically deformed fragments A and B are combined to form the combined molecular species AB. It is analyzed in the framework of the Kohn-Sham Molecular Orbital (MO) model using a quantitative decomposition of the bond into electrostatic interaction, Pauli repulsion (or exchange repulsion or overlap repulsion), and (attractive) orbital interactions (Eq. 5.2).^[7]

$$\Delta E_{\text{int}} = \Delta V_{\text{elstat}} + \Delta E_{\text{Pauli}} + \Delta E_{\text{oi}} \quad (5.2)$$

The term ΔV_{elstat} corresponds to the classical electrostatic interaction between the unperturbed charge distributions $\rho_A(r) + \rho_B(r)$ of the deformed fragments A and B (*vide infra* for definition of the fragments) that adopt their positions in the overall molecule AB, and is usually attractive. The Pauli repulsion term, ΔE_{Pauli} , comprises the destabilizing interactions between occupied orbitals and is responsible for the steric repulsion. This repulsion is caused by the fact that two electrons with the same spin cannot occupy the same region in space (cf. Pauli principle). It arises as the energy change associated with the transition from the superposition of the unperturbed electron densities $\rho_A(r) + \rho_B(r)$ of the geometrically deformed but isolated fragments A and B to the wavefunction $\Psi^0 = N \hat{A} [\Psi_A \Psi_B]$, that properly obeys the Pauli principle through explicit antisymmetrization (\hat{A} operator) and renormalization (N constant) of the product of fragment wavefunctions (see Ref. [7a] for an exhaustive discussion). The orbital interaction ΔE_{oi} in any MO model, and therefore also in Kohn-Sham theory, accounts for charge transfer (i.e., donor–acceptor interactions between occupied orbitals on one moiety with unoccupied orbitals of the other, including the HOMO–LUMO interactions) and polarization (empty–occupied orbital mixing on one fragment due to the presence of another fragment).^[7] Since the Kohn-Sham MO method of density-functional theory (DFT) in principle yields exact energies and, in practice, with the available density functionals for exchange and correlation, rather accurate energies, we have

the special situation that a seemingly one-particle model (a MO method) in principle completely accounts for the bonding energy.^[7a]

The orbital interaction energy can be further decomposed into the contributions from each irreducible representation Γ of the interacting system (Eq. 5.3) using the extended transition state (ETS) scheme developed by Ziegler and Rauk^[7c-e] (note that our approach differs in this respect from the Morokuma scheme,^[12] which instead attempts a decomposition of the orbital interactions into polarization and charge transfer):

$$\Delta E_{\text{oi}} = \sum_{\Gamma} \Delta E_{\Gamma} = \Delta E_{\sigma} + \Delta E_{\pi} \quad (5.3)$$

In our model systems, the irreducible representations can be categorized into A and E symmetric which correspond to what is commonly designated σ and π electron systems, respectively. This gives rise to the orbital-interaction components ΔE_{σ} and ΔE_{π} as shown in Eq. 5.3 above.

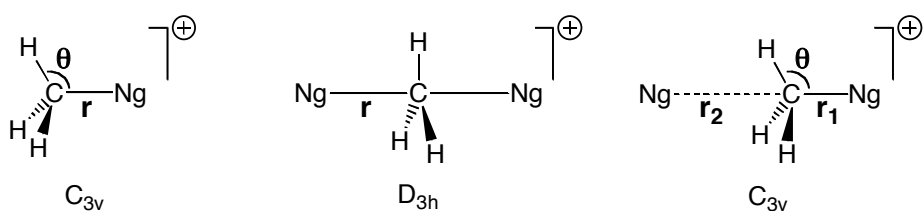
Atomic charges were computed using the Voronoi deformation density (VDD) method^[13] and the Hirshfeld scheme.^[14]

5.3 Results and Discussions

5.3.1 Ab Initio Benchmarks and DFT Validation. Geometries

First, we have computed *ab initio* benchmark geometries and C–Ng complexation energies of CH_3Ng^+ and NgCH_3Ng^+ , for Ng = He, Ne and Ar, against which we can assess the performance of our DFT approach. The benchmarks derive from a hierarchical series of *ab initio* methods: MP2, MP4 and CCSD(T) which have been evaluated in combination with the basis sets 6-311++G** (basis B) and, in the case of MP2 and MP4, cc-pVTZ (basis C). The *ab initio* and DFT results are summarized in Tables 5.1 and 5.2, together with the scarcely available C–Ng bond distances from infrared photo dissociation (IRPD) experiments. Definitions of geometry parameters can be found in Scheme 5.1.

Scheme 5.1 Definition of geometry parameters in our model systems.



It is clear from Tables 5.1 and 5.2 that C–Ng distances (r , r_1 , r_2) and H-C-Ng angles (θ) are converged along the hierarchical series of *ab initio* methods within a few hundredths of an Å and a few tenths of a degree, respectively. We recall, however, that the geometries of the C_{3v} and D_{3h} symmetric ArCH_3Ng^+ species were evaluated in all cases only at MP2/B because of the large computational costs for these systems. The CCSD(T)/B values for C–Ng

distances in CH_3Ng^+ are 1.882 (He), 2.168 (Ne) and 1.985 Å (Ar) and those in the equilibrium structures of NgCH_3Ng^+ are 2.047 (He, D_{3h}), 2.261 (Ne, D_{3h}) and 1.991 Å (Ar, r_1 , C_{3v} ; from MP2/B!). These *ab initio* geometries agree well with previous computations by Dopfer and others.^[4] The discrepancy with the IRPD experimental C–Ng distances which are about 0.1 – 0.3 Å longer than those obtained at CCSD(T) (and also at MP2 and MP4) has previously been ascribed to the strong angular–radial coupling effect on the vibrationally averaged experimental C–Ng distances.^[4e]

Table 5.1 Geometry parameters r and θ (in Å, deg.) and complexation energies ΔE (in kcal/mol) of C_{3v} symmetric CH_3Ng^+ complexes ($\text{Ng} = \text{He}, \text{Ne}, \text{Ar}$) computed at various levels of theory.^[a]

	CH_3He^+			CH_3Ne^+			CH_3Ar^+		
	r	θ	ΔE	r	θ	ΔE	r	θ	ΔE
BP86/A	1.545	94.2	-5.19	1.964	92.8	-5.50	2.006	99.0	-25.71
OLYP/A	1.701	92.8	-1.74	2.170	91.6	-2.89	2.012	99.0	-20.61
MP2/B	1.868	91.2	-1.78	2.177	91.1	-3.29	1.951	99.8	-18.50
MP2/C	1.856	91.3	-1.73	2.170	91.2	-3.17	1.968	99.5	-18.35
MP4/B	1.857	91.3	-1.87	2.152	91.2	-3.58	1.975	99.4	-18.23
MP4/C	1.849	91.4	-1.79	2.141	91.4	-3.42	1.990	99.1	-18.05
CCSD(T)/B	1.882	91.0	-1.86	2.168	91.1	-3.45	1.985	99.1	-17.94
IRPD exp. ^[b]	2.176			2.300			2.053		

[a] Basis sets A, B and C correspond to TZ2P, 6-311++G** and cc-pVTZ (see also Sections 5.2.1–5.2.2).

[b] Data from Ref. [4a].

Table 5.2 Geometry parameters r , r_1 , r_2 and θ (in Å, deg.) and $\text{Ng} + \text{CH}_3\text{Ng}^+$ complexation energies ΔE (in kcal/mol) of D_{3h} and C_{3v} symmetric NgCH_3Ng^+ complexes ($\text{Ng} = \text{He}, \text{Ne}, \text{Ar}$)^[a] computed at various levels of theory.^[b]

	HeCH_3He^+		NeCH_3Ne^+		$\text{ArCH}_3\text{Ar}^+ C_{3v}$				$\text{ArCH}_3\text{Ar}^+ D_{3h}$	
	r	ΔE	r	ΔE	r_1	r_2	θ	ΔE	r	ΔE
BP86/A	1.845	-0.66	2.117	-2.45					2.364	-3.27
OLYP/A	2.123	-0.62	2.395	-1.76	2.030	3.528	98.6	-1.30	2.429	-0.48
MP2/B	2.051	-1.32	2.262	-2.80	1.991	2.941	98.7	-2.80	2.385	-1.35
MP2/C	2.015	-1.18	2.258	-2.66	1.991 ^[c]	2.941 ^[c]	98.7 ^[c]	-2.29 ^[c]	2.385 ^[c]	-1.08 ^[c]
MP4/B	2.044	-1.38	2.258	-2.99	1.991 ^[c]	2.941 ^[c]	98.7 ^[c]	-2.89 ^[c]	2.385 ^[c]	-1.84 ^[c]
MP4/C	2.010	-1.20	2.239	-2.81	1.991 ^[c]	2.941 ^[c]	98.7 ^[c]	-2.30 ^[c]	2.385 ^[c]	-1.45 ^[c]
CCSD(T)/B	2.047	-1.38	2.261	-2.92	1.991 ^[c]	2.941 ^[c]	98.7 ^[c]	-2.91 ^[c]	2.385 ^[c]	-2.08 ^[c]
IRPD exp. ^[d]			2.344							

[a] HeCH_3He^+ and NeCH_3Ne^+ are D_{3h} symmetric species.

[b] r , r_1 , r_2 are C–Ng distances; θ is the H–C–Ng angle. Basis sets A, B and C correspond to TZ2P, 6-311++G** and cc-pVTZ (see also Section 5.2).

[c] Single-point energy calculation at MP2/6-311++G** geometry.

[d] Data from Ref. [4a].

The OLYP/TZ2P values for C–Ng distances and H-C-Ng angles θ agree within about a tenth of an Å and about one degree (see Tables 5.1 and 5.2). Deviations are somewhat larger for the BP86 data but still this DFT approach reproduces the *ab initio* benchmark trends. There is one noticeably larger deviation, namely, in the case of the long C–Ng distance (r_2) in C_{3v} symmetric Ng---CH₃Ng⁺: the OLYP value here is about half an Å longer than the MP2 value. While OLYP indeed somewhat underestimates the corresponding bond energy (*vide infra*), this deviation in r_2 is also to a large extent ascribed to the extreme shallowness of the associated potential energy well. This softness in the potential makes that small changes in the level of theory and thus small changes in the bond energy may still lead to relatively larger fluctuations in r_2 .

5.3.2 *Ab Initio* Benchmarks and DFT Validation. Energies

Next, we examine the potential energy surfaces of the above species. Here, the OLYP approach turns out to excel more pronouncedly as compared to BP86 than in the case of the geometries. But first we consider the *ab initio* benchmark study. It is again clear from Tables 5.1 and 5.2 that the energies ΔE of CH₃Ng⁺ (defined by reaction 5.4) and of NgCH₃Ng⁺ (defined by reaction 5.5) are converged along the hierarchical series of ab initio methods within a few tenths of a kcal/mol.



The CCSD(T)/B values for ΔE of CH₃Ng⁺ are –1.86 (He), –3.45 (Ne) and –17.94 kcal/mol (Ar) and those in the equilibrium structures of NgCH₃Ng⁺ are –1.38 (He, D_{3h}), –2.92 (Ne, D_{3h}) and –2.91 kcal/mol (Ar, C_{3v}). Note that, in the case of Ng = Ar, the equilibrium structure is a C_{3v} symmetric reactant complex Ar---CH₃Ar⁺ and that the D_{3h} symmetric [Ar-CH₃-Ar]⁺ is a transition state at ΔE = –2.08 kcal/mol, i.e., +0.83 kcal/mol above the asymmetric reactant complex (compare upper and lower PES in Figure 5.1). These *ab initio* relative energies agree again well with the available results from previous studies.^[4]

The OLYP/TZ2P approach, as pointed out above, agrees well with the *ab initio* benchmark: relative energies typically agree within about a kcal/mol with a somewhat larger deviation of about two and a half kcal/mol in the case of CH₃Ar⁺. Importantly, the trends in relative energies is correctly reproduced by OLYP: (i) a slight strengthening in ΔE from CH₃He⁺ to CH₃Ne⁺ and a significant stabilization from CH₃Ne⁺ to CH₃Ar⁺; and (ii) a slight strengthening in ΔE from HeCH₃He⁺ to NeCH₃Ne⁺, a very subtle weakening from NeCH₃Ne⁺ to Ar---CH₃Ar⁺ and, notably, the occurrence, in the latter, of a weakly labile D_{3h} symmetric [Ar-CH₃-Ar]⁺ species that is 0.82 kcal/mol above two C_{3v} symmetric reactant complexes which it separates along an S_N2 reaction pathway (compare upper and lower PES in Figure 5.1). The BP86/TZ2P approach fails in particular regarding the qualitative trend of having

stable D_{3h} symmetric, pentavalent $[\text{He}-\text{CH}_3-\text{He}]^+$ and $[\text{Ne}-\text{CH}_3-\text{Ne}]^+$ complexes but a labile five-coordinate $[\text{Ar}-\text{CH}_3-\text{Ar}]^+$ that localizes one of the C–Ar bonds and partially breaks the other one, leading to the asymmetric $\text{Ar}---\text{CH}_3\text{Ar}^+$ equilibrium structure.

In conclusion, OLYP/TZ2P agrees well with the *ab initio* benchmarks for Ng = He, Ne and Ar and performs better than the BP86/TZ2P approach. Therefore, in the following, we carry out our computations and analyses for the full range of systems, i.e., for Ng = He, Ne, Ar, Kr, Xe and Rn, using OLYP/TZ2P in combination with ZORA relativistic effects for Kr, Xe and Rn.

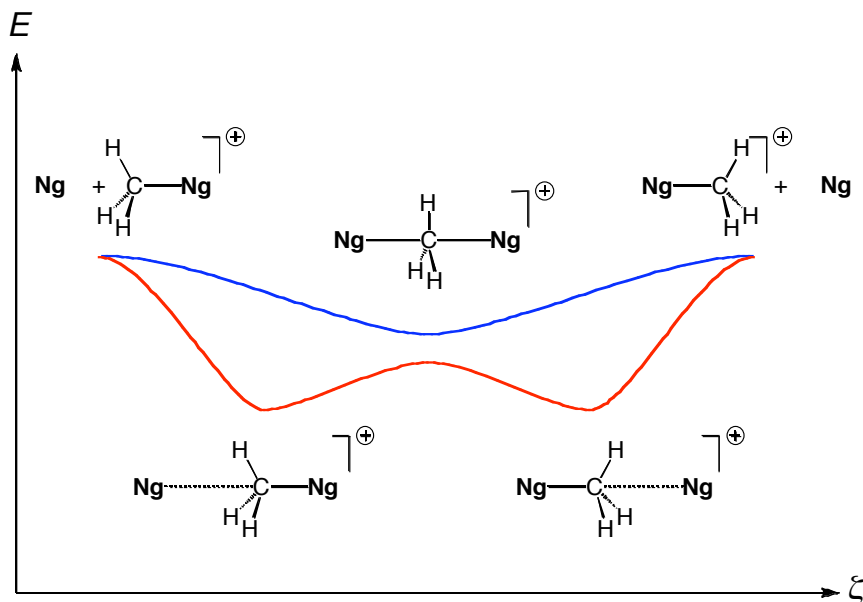


Figure 5.1 Single-well (upper: Ng = He, Ne) and double-well (lower: Ng = Ar - Rn) potential energy surface along the S_N2 reaction coordinate ξ of Ng + CH_3Ng^+ .

5.3.3 Structure and Bonding in $[\text{CH}_3-\text{Ng}]^+$

The C–Ng bond strength ΔE of the CH_3Ng^+ complexes increases monotonically if we descend along the Ng atoms in group 18: from -1.7 (He) to -2.9 (Ne) to -20.6 (Ar) to -30.2 (Kr) to -42.6 (Xe) to -49.3 kcal/mol (Rn), as computed at (ZORA-)OLYP/TZ2P (see Table 5.3). Thus, the previously obtained trend of a systematic C–Ng bond strengthening along Ng = He, Ne and Ar continues, beyond these atoms, also for the heavier noble gases, down till radon.

The trend becomes more pronounced along Ne, Ar, Kr, Xe and Rn. Now, both the HOMO–LUMO gap (which decreases) and the bond overlap (which increases towards a plateau) work in concert and cause the orbital interactions ΔE_{oi} and thus the net C–Ng bond strength ΔE to increase markedly as mentioned above (see Table 5.3 and Eq. 5.2). Note in particular the sharp increase in C–Ng bond strength from -2.9 to -20.6 kcal/mol as one goes from CH_3Ne^+ to CH_3Ar^+ .

Table 5.3 Analysis of the C–Ng bond between CH_3^+ and Ng in CH_3Ng^+ (Ng = He, Ne, Ar, Kr, Xe and Rn).^[a]

	CH_3He^+	CH_3Ne^+	CH_3Ar^+	CH_3Kr^+	CH_3Xe^+	CH_3Rn^+
Geometry (in Å, deg.)						
C–Ng: r	1.701	2.170	2.012	2.114	2.242	2.320
H-C-Ng: θ	92.8	91.6	99.0	100.1	101.8	102.3
C–H	1.094	1.094	1.089	1.089	1.088	1.088
Bond Energy Decomposition (in kcal/mol) ^[b]						
ΔE_{oi}	-16.47	-9.94	-71.58	-88.46	-111.62	-120.21
ΔE_{Pauli}	17.51	8.65	57.12	63.84	73.16	72.95
ΔV_{elstat}	-3.36	-1.79	-12.26	-13.25	-14.64	-13.45
ΔE_{int}	-2.32	-3.08	-26.71	-37.87	-53.1	-60.72
ΔE_{prep}	0.58	0.19	6.10	7.72	10.54	11.38
$\Delta E: \text{CH}_3^+ + \text{Ng}$	-1.74	-2.89	-20.61	-30.15	-42.56	-49.34
$(\Delta E: \text{Ng} + \text{CH}_3\text{Ng}^+)$ ^[c]	(-0.62)	(-1.76)	(-1.30)	(-1.65)	(-1.99)	(-2.21)
$\langle \text{Ng} \text{CH}_3^+ \rangle$ Fragment Orbital Overlap						
$\langle \text{HOMO} \text{LUMO} \rangle$	0.27	0.13	0.27	0.29	0.31	0.30
Fragment Orbital Energy (in eV)						
Ng: HOMO a_1	-15.783	-13.604	-10.209	-9.163	-8.141	-7.556
Fragment Orbital Population (in electrons)						
Ng: HOMO a_1	1.90	1.93	1.60	1.55	1.42	1.32
$\text{CH}_3^+:$ LUMO a_1	0.11	0.07	0.39	0.45	0.58	0.65
Noble-Gas Atomic Charge (in a.u.)						
Q^{VDD}	0.26	0.18	0.42	0.48	0.54	0.58
$Q^{\text{Hirshfeld}}$	0.18	0.16	0.47	0.54	0.63	0.68

[a] Computed at OLYP/TZ2P with ZORA relativistic effects for Ng = Kr, Xe and Rn. See Section 5.2.

[b] $\Delta E = \Delta E_{\text{prep}} + \Delta E_{\text{int}} = \Delta E_{\text{prep}} + \Delta V_{\text{elstat}} + \Delta E_{\text{Pauli}} + \Delta E_{\text{oi}}$. See also Section 5.2.

[c] For comparison: ΔE associated with adding a second Ng to CH_3Ng^+ under formation of the NgCH_3Ng^+ equilibrium structure (D_{3h} for Ng = He, Ne; C_{3v} for Ng = Ar, Kr, Xe, Rn).

The overall trend in bond strengths ΔE and especially that in ΔE_{oi} is nicely reflected by the trend in the gross population P of the CH_3^+ $2a_1$ LUMO in CH_3Ng^+ ($P = 0.11, 0.07, 0.39, 0.45, 0.58$ and 0.65 e along He - Rn) as well as the trend noble-gas atomic charge ($Q^{\text{VDD}} = +0.26, +0.18, +0.42, +0.48, +0.54$ and $+0.58\text{ a.u.}$; see Table 5.3). These trends all are consistent with an increasing donor–acceptor orbital interaction and an increasing amount of electronic charge transfer from noble gas to methyl cation along He, Ne, Ar, Xe, Kr and Rn. In line with this, the extent of pyramidalization increases along this series, as reflected by the H-C-Ng angle θ which varies along 92.8° (He), 91.6° (Ne), 99.0° (Ar), 100.1° (Kr), 101.8° (Xe) and 102.3° (Rn; see Table 5.3). This can be understood in terms of the above-mentioned increase in the HOMO–LUMO interactions in ΔE_{oi} along this series which works in two

ways: (i) the very HOMO–LUMO interaction itself directly ("electronically") induces pyramidalization because this deformation lowers the methyl $2a_1$ LUMO^[15] and thus stabilizes the HOMO–LUMO interaction (see Figure 5.2a); (ii) it also indirectly induces pyramidalization through the approach of the (increasingly bulky) noble-gas atom which sterically forces the substituents (i.e., the three hydrogen atoms) to bend backwards.^[1c,d]

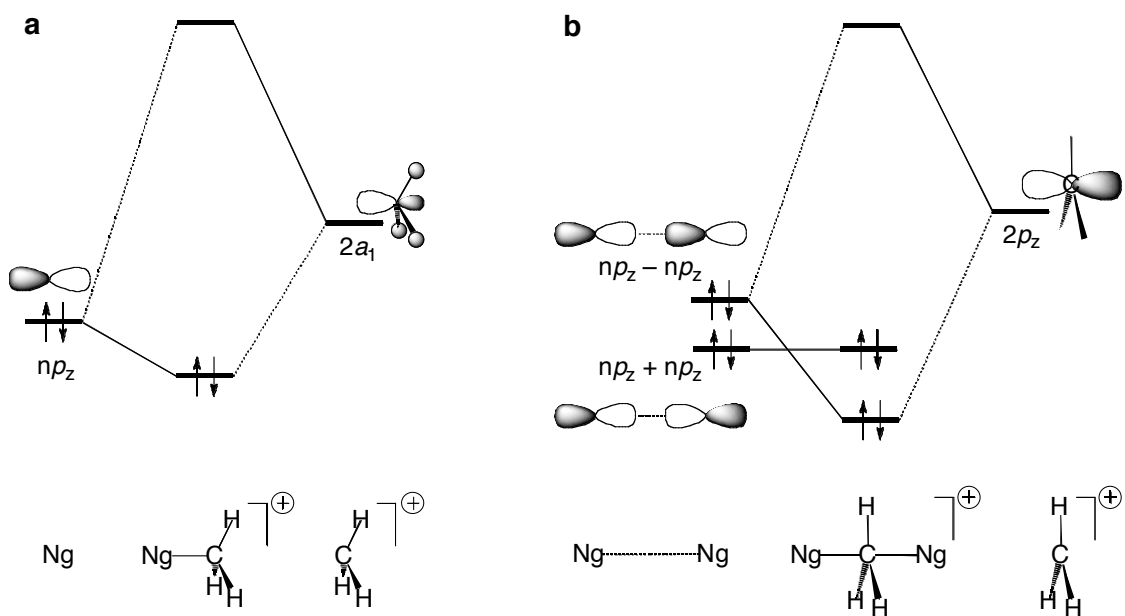


Figure 5.2 Generic frontier orbital-interaction diagrams: (a) between Ng and CH_3^+ in CH_3Ng^+ , and (b) between Ng---Ng and CH_3^+ in D_{3h} symmetric NgCH_3Ng^+ . Based on Kohn-Sham MO analyses at (ZORA-)OLYP/TZ2P. For Ng = He, the noble-gas AOs are $1s$ instead of np_z .

Importantly however the methyl moiety in the CH_3Ng^+ complexes is not that pyramidal at all. In fact, in CH_3He^+ and CH_3Ne^+ it is virtually planar, and the deviation from planarity for the heavier noble-gas complexes is only moderate, even in the most extreme case: CH_3Rn^+ . In the latter, θ is 102.3° which is significantly less than in the isoelectronic methyl halides CH_3X , such as CH_3Cl for which θ amounts to 108.5° , close to the perfect tetrahedral angle of 109.5° . This can again be understood in terms of the longer and much weaker (heterolytic) C–Ng bond ($\Delta E = -2$ to -49 kcal/mol; see Table 5.3) as compared to the stronger (homolytic) C–X bond ($\Delta E = -86.5$ kcal/mol for CH_3Cl ; not shown in Table 5.3; see also Ref. [15]).

The preservation of a (close to) planar, disk-shaped methyl unit in the CH_3Ng^+ species has led to the term "disk-and-ball" complex, used previously by Dopfer and coworkers.^[4a,e] This notion turns out to play a central role also in understanding the hypervalency (or "nearly hypervalency") of carbon in the NgCH_3Ng^+ systems, as will become clear in the next section.

5.3.4 Structure and Bonding in $[\text{Ng}-\text{CH}_3-\text{Ng}]^+$

The stabilization ΔE upon adding a second Ng atom to the backside of the methyl group in CH_3Ng^+ (see Eq. 5.5) ranges from -0.6 (He) through -2.2 kcal/mol (Rn) and is thus even smaller than the already weak C–Ng bond strength associated with adding the first one to CH_3^+ (see Eq. 5.4), as can be seen in Table 5.3 by comparing the ΔE values in parentheses (referring to Eq. 5.5) to the corresponding values without parentheses (referring to Eq. 5.4). The approach of the second Ng atom slightly pushes the hydrogen atoms of the methyl moiety back towards the first Ng atom. Accordingly, the methyl fragment becomes about $1 - 2^\circ$ less pyramidal, as measured by the H-C-Ng angle θ (compare θ values in Tables 5.3 and 5.4). Note that this is enough to make the methyl unit in $[\text{He}-\text{CH}_3-\text{He}]^+$ and $[\text{Ne}-\text{CH}_3-\text{Ne}]^+$ virtually planar, thus, yielding D_{3h} symmetric equilibrium structures with a hypervalent carbon atom (see Table 5.4). The heavier noble-gas complexes however retain a C_{3v} symmetric geometry $\text{Ng---CH}_3\text{Ng}^+$ with a localized and a somewhat longer C–Ng bond.

In the following, we discuss the stability and bonding in NgCH_3Ng^+ species in terms of the energy ΔE associated with forming a trimer from two noble-gas atoms and a methyl cation:



The stability ΔE of equilibrium structures NgCH_3Ng^+ , defined in this way, shows the same trend as that of CH_3Ng^+ (see Eq. 5.4): it increases monotonically if we descend along the Ng atoms in group 18: from -2.4 (He) to -4.6 (Ne) to -21.9 (Ar) to -31.8 (Kr) to -44.6 (Xe) to -51.6 kcal/mol (Rn), as computed at (ZORA-)OLYP/TZ2P (see Table 5.4). As mentioned above, the NgCH_3Ng^+ species adopt D_{3h} symmetric (hypervalent) structures for Ng = He and Ne. From Ng = Ar and downwards group 18, the D_{3h} symmetric species are S_{N2} transition states that connect two equivalent C_{3v} symmetric $\text{Ng---CH}_3\text{Ng}^+$ complexes via a relatively low central barrier of $0.8 - 1.2$ kcal/mol (see ΔE_{rel} in Table 5.4).

The trend in ΔE derives again mainly from the systematic increase in the energy of the valence $1s$ or np atomic orbitals (AOs) along the series of noble gas atoms, as follows from our analyses. Here, we have analyzed ΔE in terms of the interaction ΔE_{int} between the Ng---Ng fragment and the CH_3^+ fragment plus the preparation energy ΔE_{prep} (see Eq. 5.2). The latter term consists of the energy change associated with bringing the two Ng atoms together in Ng---Ng , which is negligibly endothermic (i.e., 0.2 kcal/mol or less; not shown in Table 5.4), plus the energy change upon deforming the CH_3^+ fragment, which essentially makes up the entire preparation energy. Note however that ΔE_{prep} is somewhat smaller in NgCH_3Ng^+ ($\Delta E_{\text{prep}} = 0.01 - 9.27$ kcal/mol) than in CH_3Ng^+ ($0.19 - 11.38$ kcal/mol) because the methyl group is less pyramidal in the former than in the latter (compare values in Tables 5.4 and 5.3, respectively). The trend in stability ΔE is determined by the trend in the actual interaction ΔE_{int} which, in turn, is dominated by the trend in the orbital interactions ΔE_{oi} (see Table 5.4).

Table 5.4 Analysis of C–Ng bonding between Ng---Ng and CH_3^+ in D_{3h} and C_{3v} stationary points of NgCH_3Ng^+ (Ng = He, Ne, Ar, Kr, Xe and Rn).^[a]

	<u>HeCH₃He⁺</u>	<u>NeCH₃Ne⁺</u>	<u>ArCH₃Ar⁺</u> ^[c]	<u>KrCH₃Kr⁺</u> ^[c]	<u>XeCH₃Xe⁺</u> ^[c]	<u>RnCH₃Rn⁺</u> ^[c]		
	<u>D_{3h}</u> ^[b]	<u>D_{3h}</u> ^[b]	<u>C_{3v}</u>	<u>D_{3h}</u>	<u>C_{3v}</u>	<u>D_{3h}</u>	<u>C_{3v}</u>	<u>D_{3h}</u>
Geometry Parameters (in Å, deg.)								
C–Ng: r_1	2.123	2.395	2.030	2.429	2.153	2.539	2.281	2.697
C–Ng: r_2	2.123	2.395	3.528	2.429	3.443	2.539	3.679	2.697
H–C–Ng: θ	90.0	90.0	98.6	90.0	99.2	90.0	100.9	90.0
C–H	1.093	1.094	1.089	1.086	1.088	1.085	1.087	1.082
Bond Energy Decomposition (in kcal/mol) ^[d]								
ΔE_{oi}	-8.58	-10.60	-70.28	-48.66	-84.75	-63.65	-107.62	-81.14
ΔE_{Pauli}	7.57	7.37	54.56	34.49	58.84	41.04	67.74	47.38
ΔV_{elstat}	-1.36	-1.41	-11.73	-7.01	-12.23	-8.41	-13.66	-9.74
ΔE_{int}	-2.37	-4.64	-27.45	-21.17	-38.15	-31.02	-53.54	-43.49
ΔE_{prep}	0.01	0.01	5.54	0.08	6.35	0.11	8.98	0.17
ΔE	-2.36	-4.63	-21.91	-21.09	-31.80	-30.91	-44.56	-43.32
$(\Delta E_{\text{rel}})^{[e]}$	(0.00)	(0.00)	(0.00)	(0.82)	(0.00)	(0.89)	(0.00)	(1.24)
$\langle \text{Ng---Ng} \text{CH}_3^+ \rangle$ Fragment Orbital Overlap								
$\langle \text{HOMO} \text{LUMO} \rangle$	0.215	0.135	0.220	0.247	0.243	0.267	0.256	0.283
$\langle \text{HOMO-1} \text{LUMO} \rangle$	0.000	0.000	0.156	0.000	0.149	0.000	0.161	0.000
Fragment Orbital Energy (in eV)								
Ng---Ng: HOMO	-15.78	-13.60	-10.20	-10.18	-9.15	-9.13	-8.12	-8.09
Ng---Ng: HOMO-1	-15.79	-13.61	-10.22	-10.23	-9.18	-9.20	-8.16	-8.19
Fragment Orbital Population (in electrons)								
$\text{CH}_3^+:$ LUMO	0.07	0.08	0.38	0.38	0.44	0.43	0.57	0.56
Noble-Gas Atomic Charge (in a.u.)								
Q^{VDD}	0.15	0.12	0.23 ^[f]	0.23	0.26 ^[f]	0.26	0.29 ^[f]	0.30
$Q^{\text{Hirshfeld}}$	0.09	0.11	0.25 ^[f]	0.26	0.30 ^[f]	0.31	0.35 ^[f]	0.36

[a] Computed at OLYP/TZ2P with ZORA relativistic effects for Ng = Kr, Xe and Rn. See Section 5.2.

[b] D_{3h} symmetric NgCH_3Ng^+ structure is equilibrium geometry for Ng = He, Ne.

[c] C_{3v} and D_{3h} symmetric structures are equilibrium and S_N2 transition-state geometries, respectively, for Ng = Ar, Kr, Xe, Rn.

[d] $\Delta E = \Delta E_{\text{prep}} + \Delta E_{\text{int}} = \Delta E_{\text{prep}} + \Delta V_{\text{elstat}} + \Delta E_{\text{Pauli}} + \Delta E_{\text{oi}}$. See also Section 5.2.

[e] $\Delta E_{\text{rel}} = \Delta E(D_{3h}) - \Delta E(C_{3v})$ = central barrier for S_N2 reaction of Ng + CH_3Ng^+ .

[f] Average of the atomic charges of each of the two Ng atoms.

This is all very much alike the situation for the C–Ng bond in CH_3Ng^+ , discussed above, as is the fact that ΔE_{oi} stem for about 90% or more (values not shown in Table 5.4) from the donor–acceptor interactions between the occupied noble-gas valence AOs of Ng---Ng and the methyl-cation 2a₁ LUMO in the σ-electron system (values of ΔE_{σ} not shown in Table 5.4). In

the Ng---Ng fragment, however, the noble-gas AOs combine into a bonding $np_z + np_z$ and antibonding $np_z - np_z$ fragment MO, the HOMO-1 and HOMO of the σ -electron system (see Figure 5.2b). In the D_{3h} symmetric structure, the HOMO-1 has zero overlap with the methylcation LUMO $2a_1$ (we adhere to using this C_{3v} symmetry label, for comparability with C_{3v} symmetric $\text{Ng---CH}_3\text{Ng}^+$ and CH_3Ng^+ species). The donor–acceptor interaction is now provided only by the HOMO–LUMO interaction which increases again as the orbital energy of the HOMO ($-15.8 \text{ -- } -7.5 \text{ eV}$ along the series) as well as the $\langle \text{HOMO} | \text{LUMO} \rangle$ overlap ($0.14 \text{ -- } 0.29$ along the series) increase as Ng descends in group 18 (see Table 5.4). Note that the energy of the Ng---Ng HOMO and HOMO-1 both differ hardly from the noble-gas AOs they derive from (compare orbital energies in Tables 5.4 and 5.3, respectively). This is due to the fact that the noble-gas atoms in Ng---Ng have a relatively large separation of more than 4 \AA and therefore experience only a very minor mutual interaction.

However, if the D_{3h} symmetric species is allowed to relax towards bond localized C_{3v} symmetric equilibrium structure $\text{Ng---CH}_3\text{Ng}^+$ (for Ng = Ar - Rn), the Ng---Ng HOMO-1 can also build up an overlap with the CH_3^+ LUMO of about 0.15 while the $\langle \text{HOMO} | \text{LUMO} \rangle$ overlap is reduced by an amount of some 0.03 only (see Table 5.4). This leads in all cases to a net strengthening of the orbital interactions ΔE_{oi} and of the net interaction energy ΔE_{int} .

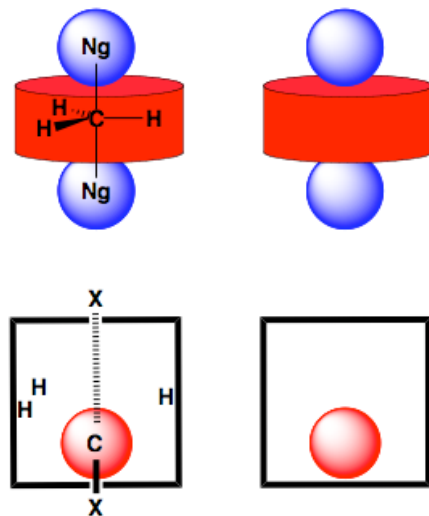
The question whether this extra stabilization upon C–Ng bond localization causes a lowering of the overall energy, and thus really happens, depends on the question if the interaction is strong enough to surmount the deformation energy ΔE_{prep} needed to pyramidalize the rigid methyl cation. As can be seen in Table 5.4, the C–Ng interaction energy ΔE_{int} shows again (as in the case of the CH_3Ng^+ species) a strong increase from -4.6 to -21.2 kcal/mol if we go from D_{3h} symmetric $[\text{Ne---CH}_3\text{---Ne}]^+$ to $[\text{Ar---CH}_3\text{---Ar}]^+$ and then further increases to -51.0 for $[\text{Rn---CH}_3\text{---Rn}]^+$. Going from D_{3h} symmetric $[\text{Ar---CH}_3\text{---Ar}]^+$ to the C_{3v} symmetric $\text{Ar---CH}_3\text{Ar}^+$, ΔE_{int} is stabilized by -6.3 kcal/mol which is just enough to surmount the pyramidalization energy ΔE_{prep} of CH_3^+ which amounts here to 5.5 kcal/mol . Note that even the *total* interaction energy ΔE_{int} of -2.4 and -4.6 kcal/mol in $[\text{He---CH}_3\text{---He}]^+$ and $[\text{Ne---CH}_3\text{---Ne}]^+$ is too small to surmount such a pyramidalization energy (see Table 5.4). The methyl cation is too firmly bound and rigid to gain overall stabilization from C–Ng bond localization.

5.3.5 The Methyl Cation in $[\text{Ng---CH}_3\text{---Ng}]^+$ as a "Disk between Balls"

The qualitative picture that emerges from our MO analyses is that CH_3^+ is a rigid, internally tightly bound "disk" that touches with two weaker contacts to a ball above and below, the two noble-gas atoms. We designate this bonding situation "disk-between-balls" (DbB) model (see Scheme 5.2, upper), in analogy to the term "disk-and-ball" complex used by Dopfer for CH_3Ng^+ complexes.^[4a,e] The resistance of the CH_3^+ fragment to pyramidalize is related to the

strong and short C–H bonds which cause the hydrogen atoms to be in close, steric contact. Pyramidalization aggravates this steric repulsion and is therefore avoided.^[15a]

Scheme 5.2 "Disk-between-Balls" (upper) versus Ball-in-a-Box model (lower) for five-coordinate carbon.



Note however that the rigidity of the methyl moiety is a relative property: CH_3^+ is internally rigid if compared to the weak carbon–axial substituent ($\text{C}-\text{X}^{\text{ax}}$) bond in the noble-gas complexes, especially for $\text{Ng} = \text{He}$ and Ne . It is this situation that causes the breakdown of the ball-in-a-box (BiaB) model (Scheme 5.2, lower). The latter explains why silicon in $[\text{Cl}-\text{SiH}_3-\text{Cl}]^-$ is hypervalent whereas carbon in $[\text{Cl}-\text{CH}_3-\text{Cl}]^-$ is not. In terms of this model, silicon fits perfectly into the box that is constituted by the five substituents. Carbon, on the other hand, is too small and, in a sense, "drops to the bottom" of the box leading, consequently, to a species $\text{Cl}^--\text{H}_3\text{CCl}$ with one long C–Cl bond, one localized C–Cl contact, and a pyramidalized CH_3 unit. The validity of this model was shown to extend also to heavier group-14 central atoms (Ge, Sn, Pb) as well as for other axial substituents (F). However, the ball-in-a-box (BiaB) picture is no longer a reasonable physical model if the carbon atom binds much more firmly to the "walls of the box" than to the "bottom", i.e., if the carbon atom begins to form a much tighter subunit with the equatorial hydrogen atoms.

Thus, a switch occurs in the bonding capability of five-coordinate carbon from hypervalent (DbB model) to nonhypervalent (BiaB model) if the interaction with the axial substituents is strong enough such that bond localization yields sufficient $\text{C}-\text{X}^{\text{ax}}$ bonding stabilization to compensate for the loss in stability in the methyl moiety that goes with the accompanying pyramidalization. Accordingly, all five-coordinate-carbon species for which the BiaB model holds, we have much smaller differences between the strength of the carbon–equatorial hydrogen ($\text{C}-\text{H}^{\text{eq}}$) bond and the $\text{C}-\text{X}^{\text{ax}}$ bond: the former have weaker and the latter significantly stronger interaction energies. This can be nicely seen in Table 5.5 which shows the ΔE_{int} energies of $\text{C}-\text{H}^{\text{eq}}$, $\text{C}-\text{X}^{\text{ax}}$ and their $\text{C}-\text{H}^{\text{eq}}/\text{C}-\text{X}^{\text{ax}}$ ratio for a series of

isoelectronic, D_{3h} symmetric $[X-CH_3-X]^q$ species that all share an X–C–X 3-center–4-electron bonding motive. Thus, for $[F-CH_3-F]^-$ and $[Cl-CH_3-Cl]^-$, the C–H^{eq}/C–X^{ax} ratio adopts moderate values of 2.4 to 3.5. On the other hand, for $[He-CH_3-He]^+$ and $[Ne-CH_3-Ne]^+$, the C–H^{eq}/C–X^{ax} ratio is comparatively large, with 132 and 63, respectively.

Table 5.5 Valency of a central carbon atom in terms of the spectrum of bonding situations between disk-between-balls and ball-in-a-box model.

species	bond strengths ^[a]			model ^[b]	barrier ^[c]	C valency
	C–H ^{eq}	C–X ^{ax}	ratio			
$[He-CH_3-He]^+$	-131.50	-1.00	131.5	DbB	0.0	hyper
$[Ne-CH_3-Ne]^+$	-130.89	-2.09	62.6	DbB	0.0	hyper
$[Ar-CH_3-Ar]^+$	-126.35	-6.25	20.2	DbB/BiaB	0.8	weakly nonhyper
$[Kr-CH_3-Kr]^+$	-124.49	-8.34	14.9	DbB/BiaB	0.9	weakly nonhyper
$[Xe-CH_3-Xe]^+$	-122.34	-10.47	11.7	DbB/BiaB	1.2	weakly nonhyper
$[Rn-CH_3-Rn]^+$	-121.22	-11.71	10.4	DbB/BiaB	0.8	weakly nonhyper
$[Cl-CH_3-Cl]^-$	-112.75	-31.88	3.5	BiaB	8.9	nonhyper
$[F-CH_3-F]^-$	-109.35	-44.65	2.4	BiaB	8.1	nonhyper

[a] Homolytic C–H^{ax} and heterolytic C–X^{eq} interaction energies ΔE_{int} (in kcal/mol) between the corresponding molecular fragments frozen to the geometry they adopt in the overall D_{3h} symmetric species; see also Section 5.2 and Eq. 5.1. Computed at OLYP/TZ2P with ZORA relativistic effects for Ng = Kr, Xe and Rn.

[b] BiaB = ball in a box; DbB = disk between balls; DbB/BiaB = intermediate situation.

[c] Central S_N2 barrier (in kcal/mol).

At this point, we wish to stress that, of course, the rigidity of the methyl moiety also depends on its effective valence configuration. Although all the species listed in Table 5.5 are isoelectronic, the $[Ng-CH_3-Ng]^+$ complexes have effectively a methyl cation fragment whereas the more conventional S_N2 transition states $[X-CH_3-X]^-$ contain, effectively a methyl radical fragment. The latter, i.e., $CH_3\cdot$, opposes much less to pyramidalization than CH_3^+ . This is illustrated in Figure 5.3 which shows the PES for pyramidalizing CH_3^+ , $CH_3\cdot$ and, for comparison, CH_3^- , which is even stabilized by adopting a pyramidal structure.^[15a,17] At the same time, the C–H interaction energy also decreases in this order (see Table 5.5). Therefore, the somewhat simplifying criterion of the C–H^{eq}/C–X^{ax} ratio of interaction energies is still valid, although it should not be overrated. On the other hand, this C–H^{eq}/C–X^{ax} ratio criterion is in practice very straightforwardly applicable and therefore a powerful tool for categorizing five-coordinate carbon species as hypervalent (DbB) or nonhypervalent (BiaB).

Finally, we note that the data in Table 5.5 suggest a spectrum of bonding situations that runs from truly hypervalent (DbB model) to truly nonhypervalent (BiaB model) via a range of intermediate bonding situations (DbB/BiaB in Table 5.5). Of course, the transition from hypervalent (stable D_{3h} symmetric species) to nonhypervalent (labile D_{3h} symmetric species) cannot be taken as a sharp border between DbB and BiaB, and the choice of where to classify the situation as intermediate or “weakly nonhypervalent” is certainly associated with some arbitrariness. Yet, it is also a fact that the propensity of the system to localize one of its C–X^{ax}

bonds and to expand the other one, smoothly increases if one goes down in Table 5.5. We feel that is possible to conceive the $[\text{Ng}-\text{CH}_3-\text{Ng}]^+$ complexes with intermediate $\text{C}-\text{H}^{\text{eq}}/\text{C}-\text{X}^{\text{ax}}$ ratios (ca. 10 to 20 for Ng = Rn, Xe, Kr, Ar) as distorted DbB complexes as well as species that show BiaB behavior. Here, in Table 5.5, we have chosen to classify the species with $S_{\text{N}}2$ central barriers of about 0, 1 and 10 kcal/mol as truly hypervalent (DbB), “weakly hypervalent (DbB/BiaB) and truly nonhypervalent (BiaB).

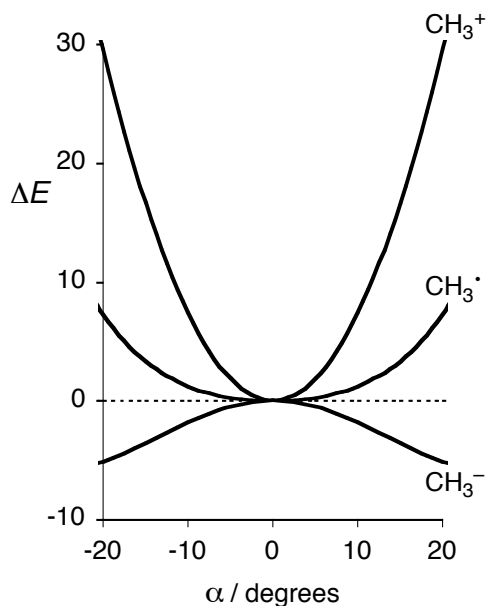


Figure 5.3 Relative energy (in kcal/mol) of CH_3^+ , CH_3^\cdot and CH_3^- as a function of the pyramidalization angle $\alpha = \theta - 90^\circ$ (see Scheme 5.1), computed at OLYP/TZ2P.

5.3.6 Comparison with $[\text{Ng}-\text{H}]^+$ and $[\text{Ng}-\text{H}-\text{Ng}]^+$

Finally, we compare the disk-and-ball as well as the disk-between-balls complexes CH_3Ng^+ and NgCH_3Ng^+ , respectively, with the corresponding protonated noble-gas atoms and proton-bound noble-gas dimers. The above results show that, if the central $[\text{CH}_3]$ unit is sufficiently tightly bound and rigid, stable, hypervalent $[\text{X}-\text{CH}_3-\text{X}]^q$ structures occur. This also nicely agrees with the finding of a previous study that $[\text{Cl}-\text{C}-\text{Cl}]^{***}$, which is isoelectronic to the labile transition state $[\text{Cl}-\text{CH}_3-\text{Cl}]^-$ also forms a stable symmetric structure with two equivalent C–Cl bonds.^[1]

Indeed, the proton-bound noble-gas dimers adopt $D_{\infty h}$ symmetric, hypervalent $[\text{Ng}-\text{H}-\text{Ng}]^+$ equilibrium structures with Ng–H distances that monotonically increase from 0.939 (He) to 1.169 (Ne) to 1.533 (Ar) to 1.685 (Kr) to 1.890 (Xe) to 1.986 Å (Kr), as can be seen in Table 5.6. The stabilization ΔE associated with the complexation of the proton with the first noble-gas atom (see Eq. 5.7 and Table 5.7) increases monotonically from -46.7 (He) to -52.8 (Ne) to -96.6 (Ar) to -109.0 (Kr) to -125.4 (Xe) to -133.9 kcal/mol (Rn), in good

agreement with previous computations of the proton affinities ($\text{PA} = -\Delta E$) of these species at ZORA-BP86/TZ2P.^[16]



The stabilization ΔE associated with the complexation of NgH^+ with the second noble-gas atom (see Eq. 5.8) is consistently smaller but also increases (although not entirely monotonically) from -14.7 kcal/mol for HeHHe^+ to -18.2 kcal/mol for RnHRn^+ (see Table 5.6).

Table 5.6 Analysis of Ng–H bonding between Ng---Ng and H⁺ in NgHNg⁺ (Ng = He, Ne, Ar, Kr, Xe and Rn).^[a]

	HeHHe ⁺	NeHNe ⁺	ArHAr ⁺	KrHKr ⁺	XeHXe ⁺	RnHRn ⁺
Ng–H Bond Distance (in Å)						
r	0.939	1.169	1.533	1.685	1.890	1.986
Bond Energy Decomposition (in kcal/mol) ^[b]						
ΔE_{oi}	-93.90	-98.82	-148.23	-161.76	-176.56	-186.50
ΔE_{Pauli}	0.00	0.00	0.00	0.00	0.00	0.00
ΔV_{elstat}	29.64	26.36	30.29	30.72	29.75	30.58
ΔE_{int}	-64.26	-72.46	-117.94	-131.04	-146.81	-155.92
ΔE_{prep}	2.85	2.43	3.88	3.99	3.94	3.81
ΔE	-61.41	-70.03	-114.06	-127.05	-142.87	-152.11
(ΔE) ^[c]	(-14.71)	(-17.22)	(-17.46)	(-18.03)	(-17.51)	(-18.22)
Noble-Gas Atomic Charge (in a.u.)						
Q^{VDD}	0.32	0.31	0.37	0.40	0.42	0.43
$Q^{\text{Hirshfeld}}$	0.30	0.35	0.42	0.44	0.47	0.48

[a] Computed at OLYP/TZ2P with ZORA relativistic effects for Ng = Kr, Xe and Rn. See also Section 5.2. NgHNg⁺ species are D_{oh} symmetric equilibrium structures, respectively.

[b] $\Delta E = \Delta E_{\text{prep}} + \Delta E_{\text{int}} = \Delta E_{\text{prep}} + \Delta V_{\text{elstat}} + \Delta E_{\text{Pauli}} + \Delta E_{\text{oi}}$. ΔE_{prep} is the energy associated with combining two separate Ng atoms into the Ng---Ng fragment. See also Section 5.2.

[c] For comparison: ΔE associated with adding a second Ng to HNg⁺ under formation of the NgHNg⁺ equilibrium structure.

This resembles the situation described above for the corresponding methyl-cation complex, for which complexation with the first noble-gas atom Ng also yields a larger stabilization than complexation of CH₃Ng⁺ with a second Ng (see Table 5.4). Also the bonding mechanism of the proton complexes is very similar to that of the methyl-cation complexes. It arises from a strong HOMO–LUMO interaction between the occupied noble-gas 1s (He) or np (Ne - Rn) valence AOs with the unoccupied proton 1s acceptor orbital. This goes with a sizeable charge transfer as reflected by the large positive charge of the noble-gas atoms Q^{VDD} that ranges from +0.41 a.u. in HeH⁺ to 0.82 a.u. in RnH⁺ (see Table 5.7).

There is however also a marked difference between the methyl-cation and the proton complexes. The bond energies in CH₃Ng⁺ (-1.7 to -49.3 kcal/mol, see Table 5.3) are much lower than in the corresponding NgH⁺ (-46.7 to -133.9 kcal/mol, see Table 5.7). The main

reason for this gigantic difference in bond energies is the Pauli repulsion ΔE_{Pauli} with closed-shell orbitals in CH_3^+ and the complete absence of such repulsion with H^+ , which has no closed shells (compare Tables 5.3 and 5.7, respectively). The only force that prevents the Ng–H bond to collapse to zero is the nuclear–nuclear repulsion. Thus, whereas the electrostatic interaction ΔV_{elstat} is in general attractive,^[7a] all NgH^+ species show pronouncedly positive (i.e., destabilizing) values between roughly 27 and 39 kcal/mol (see Table 5.7). Similar mechanisms account for the difference in bond energies between NgHNg^+ and NgCH_3Ng^+ complexes.

Table 5.7 Analysis of Ng–H bonding between Ng and H^+ in NgH^+ (Ng = He, Ne, Ar, Kr, Xe and Rn).^[a]

	HeH^+	NeH^+	ArH^+	KrH^+	XeH^+	RnH^+
Ng–H Bond Distance (in Å)						
r	0.789	1.014	1.297	1.433	1.612	1.702
Bond Energy Decomposition (in kcal/mol) ^[b]						
ΔE_{oi}	-75.94	-79.63	-134.91	-147.84	-164.18	-171.72
ΔE_{Pauli}	0.00	0.00	0.00	0.00	0.00	0.00
ΔV_{elstat}	29.24	26.83	38.31	38.82	38.82	37.84
ΔE_{int}	-46.69	-52.80	-96.60	-109.02	-125.36	-133.88
ΔE_{prep}	0.00	0.00	0.00	0.00	0.00	0.00
ΔE	-46.69	-52.80	-96.60	-109.02	-125.36	-133.88
Noble-Gas Atomic Charge (in a.u.)						
Q^{VDD}	0.44	0.44	0.57	0.63	0.66	0.70
$Q^{\text{Hirshfeld}}$	0.41	0.49	0.66	0.72	0.78	0.82

[a] Computed at OLYP/TZ2P with ZORA relativistic effects for Ng = Kr, Xe and Rn. See also Section 5.2.
 NgH^+ species are $\text{C}_{\infty v}$ symmetric equilibrium structures.

[b] $\Delta E = \Delta E_{\text{prep}} + \Delta E_{\text{int}} = \Delta E_{\text{prep}} + \Delta V_{\text{elstat}} + \Delta E_{\text{Pauli}} + \Delta E_{\text{oi}}$. See also Section 5.2.

5.4 Conclusions

The ball-in-a-box model that we recently introduced explains why silicon in $[\text{Cl}-\text{SiH}_3-\text{Cl}]^-$ is hypervalent whereas carbon in $[\text{Cl}-\text{CH}_3-\text{Cl}]^-$ is not. In terms of this model, silicon fits perfectly into the box that is constituted by the five substituents. Carbon, on the other hand, is too small and, in a sense, "drops to the bottom" of the box leading, consequently, to a species $\text{Cl}^--\text{H}_3\text{CCl}$ with one long C–Cl bond, one localized C–Cl contact, and a pyramidalized CH_3 unit. The validity of this model was shown to extend also to heavier group-14 central atoms (Ge, Sn, Pb) as well as for other axial substituents (F).

In the present study, however, we have encountered species that violate this ball-in-a-box behavior: although isostructural and isoelectronic with the above $[\text{X}-\text{CH}_3-\text{X}]^-$ systems, the noble gas–methyl cation complexes $[\text{Ng}-\text{CH}_3-\text{Ng}]^+$ adopt, for Ng = helium and neon, a perfectly D_{3h} symmetric structure featuring a stable hypervalent carbon atom with two equivalent C–Ng bonds. Our analyses show that the carbon atom in $[\text{Ng}-\text{CH}_3-\text{Ng}]^+$ can no longer be considered as a ball in a box of the five substituents because it is much more tightly bound to the equatorial H atoms than to the axial noble-gas substituents. Thus, the $[\text{Ng}-\text{CH}_3-$

$\text{Ng}]^+$ species are better conceived as a "disk between balls". Here, the "disk" is CH_3^+ and the "balls" are constituted by the two noble-gas atoms.

Finally, we propose to classify the nature of five-coordinate carbon species in terms of a spectrum between the ball-in-a-box situation (nonhypervalent C) and the disk-between-balls model (hypervalent C). The position along this spectrum is determined by the ratio (i.e., the relative magnitudes) of the strengths of the carbon-equatorial substituent bond ($\text{C}-\text{H}^{\text{eq}}$) versus that of the carbon-axial substituent bond ($\text{C}-\text{X}^{\text{ax}}$). Hypervalent species have large $\text{C}-\text{H}^{\text{eq}}/\text{C}-\text{X}^{\text{ax}}$ ratios (here: 63 - 132) whereas truly nonhypervalent species have small $\text{C}-\text{H}^{\text{eq}}/\text{C}-\text{X}^{\text{ax}}$ ratios (here: 2.4 - 3.5). Intermediate or "weakly nonhypervalent" cases (i.e., species with a weak tendency to localize one and to partly break the other axial carbon-substituent bond), such as $[\text{Ng}-\text{CH}_3-\text{Ng}]^+$ complexes with heavy noble-gas atoms, correspond to situations with intermediate $\text{C}-\text{H}^{\text{eq}}/\text{C}-\text{X}^{\text{ax}}$ ratios (here: 10 - 20).

References

- [1] S. C. A. H. Pierrefixe, C. Fonseca Guerra, F. M. Bickelhaupt, *Chem. Eur. J.* **2008**, *14*, 819.
- [2] For related work, see, for example: (a) R. Hoffmann, J. M. Howell, E. L. Muetterties, *J. Am. Chem. Soc.* **1972**, *94*, 3047; (b) G. C. Pimentel, *J. Chem. Phys.* **1951**, *19*, 446; (c) R. J. Hach, R. E. Rundle, *J. Am. Chem. Soc.* **1951**, *73*, 4321; (e) A. P. Bento, F. M. Bickelhaupt, *J. Org. Chem.* **2007**, *72*, 2201; (f) M. A. van Bochove, M. Swart, F. M. Bickelhaupt, *J. Am. Chem. Soc.* **2006**, *128*, 10738.
- [3] (a) M. B. Smith, J. March, *March's Advanced Organic Chemistry*, 6th ed., Wiley-Interscience: New York, **2007**; (b) S. S. Shaik, H. B. Schlegel, S. Wolfe, *Theoretical aspects of physical organic chemistry: the S_N2 mechanism*; John Wiley & Sons Inc: New York, **1992**; (c) J. K. Laerdhal, E. Uggerud, *Int. J. Mass Spectrom.* **2002**, *214*, 277.
- [4] (a) E. J. Bieske, O. Dopfer, *Chem. Rev.* **2000**, *100*, 3963 and references cited therein; (b) K. Hiraoka, I. Kudaka, S. Yamabe, *Chem. Phys. Lett.* **1991**, *178*, 103; (c) R. V. Olkhov, S. A. Kizkorodov, O. Dopfer, *J. Chem. Phys.* **1998**, *108*, 10046; (d) R. V. Olkhov, S. A. Kizkorodov, O. Dopfer, *J. Chem. Phys.* **1999**, *110*, 9527; (e) O. Dopfer, R. V. Olkhov, J. P. Maier, *J. Chem. Phys.* **2000**, *112*, 2176; (f) R. W. Gora, S. Roszak, J. Leszczynski, *J. Chem. Phys.* **2001**, *115*, 771; (g) O. Dopfer, D. Luckhaus, *J. Chem. Phys.* **2002**, *116*, 1012; (h) O. Dopfer, *Int. Rev. Phys. Chem.* **2003**, *22*, 437; i) A. Cunje, A. C. Hopkinson, S. Yamabe, K. Hiraoka, F. Nakagawa, M. Ishida, K. Fujita, K. Takao, A. Wada, K. Hiizumi, *J. Phys. Chem. A* **2004**, *108*, 11218.
- [5] (a) G. te Velde, F. M. Bickelhaupt, E. J. Baerends, C. Fonseca Guerra, S. J. A. van Gisbergen, J. G. Snijders, T. Ziegler, *J. Comput. Chem.* **2001**, *22*, 931; (b) C. Fonseca Guerra, J. G. Snijders, G. te Velde, E. J. Baerends, *Theor. Chem. Acc.* **1998**, *99*, 391; (c) E. van Lenthe, E. J. Baerends, J. G. Snijders, *J. Chem. Phys.* **1994**, *101*, 9783; (d) E. J. Baerends, J. Autschbach, A. Bérces, J. A. Berger, F. M. Bickelhaupt, C. Bo, P. L. de Boeij, P. M. Boerrigter, L. Cavallo, D. P. Chong, L. Deng, R. M. Dickson, D. E. Ellis, M. van Faassen, L. Fan, T. H. Fischer, C. Fonseca Guerra, S. J. A. van Gisbergen, J. A. Groeneveld, O. V. Gritsenko, M. Grüning, F. E. Harris, P. van den Hoek, C. R. Jacob, H. Jacobsen, L. Jensen, E. S. Kadantsev, G. van Kessel, R. Klooster, F. Kootstra, E. van Lenthe, D. A. McCormack, A. Michalak, J. Neugebauer, V. P. Nicu, V. P. Osinga, S. Patchkovskii, P. H. T. Philipsen, D. Post, C. C. Pye, W. Ravenek, P. Romaniello, P. Ros, P. R. T. Schipper, G. Schreckenbach, J. G. Snijders, M. Solà, M. Swart, D. Swerhone, G. te Velde, P. Vernooijss, L. Versluis, L. Visscher, O. Visser, F. Wang, T. A. Wesolowski, E. M.

- van Wezenbeek, G. Wiesnekker, S. K. Wolff, T. K. Woo, A. L. Yakovlev, T. Ziegler, *ADF2007*, Scientific Computing & Modeling, Amsterdam, The Netherlands, 2007.
- [6] (a) C. Lee, W. Yang, R. G. Parr, *Phys. Rev. B* **1988**, *37*, 785; (b) N. C. Handy, A. Cohen, *Mol. Phys.* **2001**, *99*, 403; (c) A. D. Becke, *Phys. Rev. A* **1988**, *38*, 3098; (d) J. P. Perdew, *Phys. Rev. B* **1986**, *33*, 8822; Erratum: *Phys. Rev. B* **1986**, *34*, 7406.
- [7] (a) F. M. Bickelhaupt, E. J. Baerends, in *Reviews in Computational Chemistry*, edited by K. B. Lipkowitz and D. B. Boyd (Wiley-VCH, New York, **2000**), Vol. 15, p. 1 - 86; (b) F. M. Bickelhaupt, N. M. M. Nibbering, E. M. van Wezenbeek, E. J. Baerends, *J. Phys. Chem.* **1992**, *96*, 4864; (c) T. Ziegler, A. Rauk, *Inorg. Chem.* **1979**, *18*, 1755; (d) T. Ziegler, A. Rauk, *Inorg. Chem.* **1979**, *18*, 1558; (e) T. Ziegler, A. Rauk, *Theor. Chim. Acta* **1977**, *46*, 1.
- [8] (a) C. Møller, M. S. Plesset, *Phys. Rev.* **1934**, *46*, 618; (b) J. J. Cizek, *Chem. Phys.* **1966**, *45*, 4256; (c) K. Raghavachari, G. W. Trucks, J. A. Pople , M. Headgordon, *Chem. Phys. Lett.* **1989**, *157*, 479.
- [9] M. J. Frisch, G. W. Trucks, H. B. Schlegel, G. E. Scuseria, M. A. Robb, J. R. Cheeseman, J. A. Montgomery, Jr., T. Vreven, K. N. Kudin, J. C. Burant, J. M. Millam, S. S. Iyengar, J. Tomasi, V. Barone, B. Mennucci, M. Cossi, G. Scalmani, N. Rega, G. A. Petersson, H. Nakatsuji, M. Hada, M. Ehara, K. Toyota, R. Fukuda, J. Hasegawa, M. Ishida, T. Nakajima, Y. Honda, O. Kitao, H. Nakai, M. Klene, X. Li, J. E. Knox, H. P. Hratchian, J. B. Cross, C. Adamo, J. Jaramillo, R. Gomperts, R. E. Stratmann, O. Yazyev, A. J. Austin, R. Cammi, C. Pomelli, J. W. Ochterski, P. Y. Ayala, K. Morokuma, G. A. Voth, P. Salvador, J. J. Dannenberg, V. G. Zakrzewski, S. Dapprich, A. D. Daniels, M. C. Strain, O. Farkas, D. K. Malick, A. D. Rabuck, K. Raghavachari, J. B. Foresman, J. V. Ortiz, Q. Cui, A. G. Baboul, S. Clifford, J. Cioslowski, B. B. Stefanov, G. Liu, A. Liashenko, P. Piskorz, I. Komaromi, R. L. Martin, D. J. Fox, T. Keith, M. A. Al-Laham, C. Y. Peng, A. Nanayakkara, M. Challacombe, P. M. W. Gill, B. Johnson, W. Chen, M. W. Wong, C. Gonzalez, J. A. Pople, *GAUSSIAN 03*, Gaussian, Inc., Pittsburgh PA, 2003.
- [10] M. J. Frisch, J. A. Pople, J. S. Binkley, *J. Chem. Phys.* **1984**, *80*, 3265.
- [11] T. H. Dunning Jr., *J. Chem. Phys.* **1989**, *90*, 1007.
- [12] K. Morokuma, *Acc. Chem. Res.* **1977**, *10*, 294.
- [13] (a) C. Fonseca Guerra, J.-W. Handgraaf, E. J. Baerends, F. M. Bickelhaupt, *J. Comput. Chem.* **2004**, *25*, 189; (b) F. M. Bickelhaupt, N. J. R. van Eikema Hommes, C. Fonseca Guerra, E. J. Baerends, *Organometallics* **1996**, *15*, 2923; (c) C. Fonseca Guerra, F. M. Bickelhaupt, J. G. Snijders, E. J. Baerends, *Chem. Eur. J.* **1999**, *5*, 3581.
- [14] F. L. Hirshfeld, *Theor. Chim. Acta* **1977**, *44*, 129.
- [15] (a) F. M. Bickelhaupt, T. Ziegler, P. v. R. Schleyer, *Organometallics* **1996**, *15*, 1477; (b) L. Deng, V. Branchadell, T. Ziegler, *J. Am. Chem. Soc.* **1994**, *116*, 10645.
- [16] M. Swart, E. Rösler, F. M. Bickelhaupt, *J. Comput. Chem.* **2006**, *27*, 1486.
- [17] T. A. Albright, J. K. Burdett, M.-H. Whangbo, *Orbital Interactions in Chemistry*; John Wiley & Sons Inc: New-York, **1985**.

Part II

Aromaticity

6 Aromaticity. Molecular Orbital Picture of an Intuitive Concept

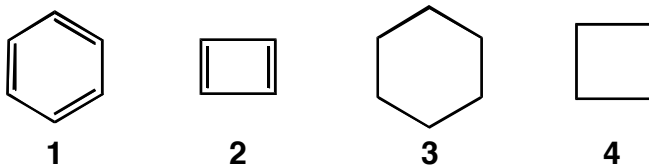
Adapted from S. C. A. H. Pierrefixe and F. M. Bickelhaupt
Chem. Eur. J. **2007**, *13*, 6321

Abstract

Geometry is one of the primary and most direct indicators of aromaticity and antiaromaticity: a regular structure with delocalized double bonds (e.g., benzene) is symptomatic of aromaticity whereas a distorted geometry with localized double bonds (e.g., 1,3-cyclobutadiene) is characteristic of antiaromaticity. Here, we present an MO model of aromaticity that explains, in terms of simple orbital-overlap arguments, *why* this is so. Our MO model is based on accurate Kohn-Sham DFT analyses of the bonding in benzene, 1,3-cyclobutadiene, cyclohexane and cyclobutane, and how the bonding mechanism is affected if these molecules undergo geometrical deformations between regular, delocalized ring structures and distorted ones with localized double bonds. We show that the propensity of the π electrons is always, i.e., in both the aromatic and antiaromatic molecules, to *localize* the double bonds, against the delocalizing force of the σ electrons. More importantly, we show that the π electrons nevertheless decide about the localization or delocalization of the double bonds. A key ingredient in our model for uncovering and resolving this seemingly contradictory situation is to analyze the bonding in the various model systems in terms of two interpenetrating fragments that preserve, in good approximation, their geometry along the localization/delocalization modes.

6.1 Introduction

Ever since the early work of Kékulé, in the mid 19th century, benzene (**1**) and its aromatic nature have appealed to the imagination of generations of chemists and physicists.^[1]



The concept of aromaticity is to some extent intuitive. The core of aromatic nature is often defined by referring to a series of structural, energetic and spectroscopic characteristics, of which the following constitute the core: (i) a highly symmetric, delocalized structure involving six C–C bonds of equal length, each with partial double-bond character, (ii) enhanced thermodynamic stability, and (iii) reduced reactivity as compared to nonaromatic conjugated hydrocarbons.^[2] Other properties that have been taken as symptoms of aromatic character are, for example, the down-field shift in proton NMR spectra, the exaltation of diamagnetic susceptibility, and a comparatively low reactivity.^[3-5] The counterpart of **1** is the antiaromatic 1,3-cyclobutadiene (**2**) which, for example, shows localized double bonds instead of a regular delocalized structure with four C–C bonds of equal length.^[2]

Aromaticity continues to be a topic in many studies associated not only with its relevance in chemistry, biology and technology, but also with the very concept itself.^[5,6] Indeed, despite many pioneering contributions on this issue, there is still a gap in our physical understanding of the nature of aromaticity.^[2-7] In the early twentieth century, Pauling and Hückel were the first to quantum chemically address the issue of benzene's (**1**) structure and enhanced stability using valence bond (VB) and molecular orbital (MO) theory.^[8,9] In a VB-type approach, used by both Pauling and Hückel, the circular topology of benzene enables a resonance between the wavefunctions of two complementary sets of localized bonds, leading to an additional stabilization. In the MO approach applied by Hückel to the benzene problem, the enhanced stability of **1** compared, for example, to isolated or linearly conjugated double bonds, is attributed to an extra bonding contact (or resonance integral or interaction matrix element) in circularly conjugated hydrocarbons with $4n+2 \pi$ electrons^[9] (a generalization to other than pericyclic topologies was later derived by Goldstein and Hoffmann).^[10] The driving force for delocalization in **1** and other circularly conjugated $4n+2 \pi$ -electron species and, likewise, the tendency of **2** and other circularly conjugated $4n \pi$ -electron systems to form localized double bonds has therefore originally been attributed to the π electron system ($n = 1$ for **1** and **2**).^[4]

Herein, we address the question *why* **1** and **2** have delocalized and localized structures, respectively, i.e. with six equivalent C–C bonds in **1** and with alternating single and double bonds in **2**. Recent sophisticated VB^[11-12] as well as MO studies^[13] confirm that the circular conjugation in benzene's π -electron system is responsible for this molecule's enhanced stability. This is also reproduced by our calculations and will not be further discussed here.

On the other hand, since the late 1950's, evidence has been repeatedly reported against the idea that benzene's (**1**) D_{6h} symmetric structure originates from a delocalizing propensity of its π -electron system.^[14,15] This led to the somewhat contradictory notion, nicely sketched by Kutzelnigg,^[16] that benzene's regular, delocalized structure is, on one hand, only possible due to the π electron's capability to form *delocalized bonds* whereas, on the other hand, the very same π electrons do favor a structure with *localized double bonds*. The distortive propensity of the π electrons has been confirmed in various studies during the last two decades.^[15] Evidence comes not only from theory but also from experiment, such as benzene's surprisingly low-energy and large-amplitude B_{2u} bond-alternation mode observed by Berry already in 1961.^[14e] This interpretation has been supported more recently by Haas and Zilberg's (computational) observation of an increase in the frequency of this B_{2u} bond-alternation mode as benzene undergoes $\pi \rightarrow \pi^*$ excitation from ground to first excited state.^[15a] Shaik, Hiberty and coworkers^[11] showed in terms of an elegant VB model that it is the σ system that enforces the delocalized, D_{6h} symmetric structure of **1** upon the π system which intrinsically strives for localized double bonds. These conclusions initiated a debate^[17] but were eventually reconfirmed by others.^[13,18] One factor that promoted a controversy is that whereas in VB theory there is a clear model why, e.g., in **1** σ delocalization overrules π localization, such a clear model is missing in MO theory that initially played such an important role in the question on aromatic stabilization and, beyond this particular issue, has been enormously successful in clarifying chemistry in general.^[19]

Our purpose is to develop a simple, qualitative MO model, based on accurate computations, that explains *why* benzene (**1**) shows delocalized double bonds whereas 1,3-cyclobutadiene (**2**) features localized double bonds. Apart from arriving at a better understanding of these archetypal geometric symptoms of aromaticity and antiaromaticity, this closes a gap in the MO theoretical treatment of this issue. Thus, we have quantum chemically investigated **1**, **2**, planar cyclohexane (**3**) and planar cyclobutane (**4**) at the BP86/TZ2P level of density functional theory (DFT) using the ADF program.^[20]

Our MO model reveals that in both, the aromatic and antiaromatic model compounds, the π -electron system always has a propensity to *localize* double bonds, against the delocalizing force of the σ -electron system. Interestingly, we can also resolve the seemingly contradictory notion that, despite the fact that they have in all cases a distortive, localizing propensity, the π electrons do play a decisive role in determining that benzene can adopt its delocalized aromatic structure whereas cyclobutadiene obtains a localized antiaromatic structure. Through our MO model, this can be understood in terms of simple orbital-overlap arguments.

6.2 Theoretical Methods

6.2.1 General Procedure

All calculations were performed using the Amsterdam Density Functional (ADF) program developed by Baerends and others.^[20] The numerical integration was performed using the procedure developed by te Velde et al.^[20g,h] The MOs were expanded in a large uncontracted set of Slater type orbitals (STOs) containing diffuse functions: TZ2P (no Gaussian functions are involved).^[20i] The basis set is of triple- ζ quality for all atoms and has been augmented with two sets of polarization functions, i.e. 3d and 4f on C and 2p and 3d on H. The 1s core shell of carbon were treated by the frozen-core approximation.^[20c] An auxiliary set of s, p, d, f and g STOs was used to fit the molecular density and to represent the Coulomb and exchange potentials accurately in each self-consistent field cycle.^[20j]

Equilibrium structures were optimized using analytical gradient techniques.^[20k] Geometries and energies were calculated at the BP86 level of the generalized gradient approximation (GGA): exchange is described by Slater's X α potential^[20l] with corrections due to Becke^[20m,n] added self-consistently and correlation is treated in the Vosko-Wilk-Nusair (VWN) parameterization^[20o] with nonlocal corrections due to Perdew^[20p] added, again, self-consistently (BP86).^[20q]

6.2.2 Bonding Energy Analysis

To obtain more insight into the nature of the bonding in our aromatic (**1**), antiaromatic (**2**) and nonaromatic model systems (**3**, **4**), an energy decomposition analysis has been carried out.^[21] In this analysis, the total binding energy ΔE associated with forming the overall molecular species of interest, say AB, from two (or sometimes more) radical fragments, A' + B', is made up of two major components (Eq. 6.1):

$$\Delta E = \Delta E_{\text{prep}} + \Delta E_{\text{int}} \quad (6.1)$$

In this formula, the preparation energy ΔE_{prep} is the amount of energy required to deform the individual (isolated) radical fragments from their equilibrium structure (A', B') to the geometry that they acquire in the overall molecule (A, B). The interaction energy ΔE_{int} corresponds to the actual energy change when these geometrically deformed fragments A and B are combined to form the combined molecular species AB. It is analyzed in the framework of the Kohn-Sham Molecular Orbital (MO) model using a quantitative decomposition of the bond into electrostatic interaction, Pauli repulsion (or exchange repulsion or overlap repulsion), and (attractive) orbital interactions (Eq. 6.2).^[21]

$$\Delta E_{\text{int}} = \Delta V_{\text{elstat}} + \Delta E_{\text{Pauli}} + \Delta E_{\text{oi}} \quad (6.2)$$

The term ΔV_{elstat} corresponds to the classical electrostatic interaction between the unperturbed charge distributions $\rho_A(r) + \rho_B(r)$ of the prepared or deformed radical fragments A and B (*vide infra* for definition of the fragments) that adopt their positions in the overall molecule AB, and is usually attractive. The Pauli repulsion term, ΔE_{Pauli} , comprises the destabilizing interactions between occupied orbitals and is responsible for the steric repulsion. This repulsion is caused by the fact that two electrons with the same spin cannot occupy the same region in space. It arises as the energy change associated with the transition from the superposition of the unperturbed electron densities $\rho_A(r) + \rho_B(r)$ of the geometrically deformed but isolated radical fragments A and B to the wavefunction $\Psi^0 = N \hat{A} [\Psi_A \Psi_B]$, that properly obeys the Pauli principle through explicit antisymmetrization (\hat{A} operator) and renormalization (N constant) of the product of fragment wavefunctions (see Ref. [21a] for an exhaustive discussion). The orbital interaction ΔE_{oi} in any MO model, and therefore also in Kohn-Sham theory, accounts for electron-pair bonding,^[21a,b] charge transfer (i.e., donor–acceptor interactions between occupied orbitals on one moiety with unoccupied orbitals of the other, including the HOMO–LUMO interactions) and polarization (empty–occupied orbital mixing on one fragment due to the presence of another fragment). In the bond-energy decomposition, open-shell fragments are treated with the spin-unrestricted formalism but, for technical (not fundamental) reasons, spin-polarization is not included. This error causes an electron-pair bond to become in the order of a few kcal/mol too strong. To facilitate a straightforward comparison, the results of the energy decomposition were scaled to match exactly the regular bond energies. Since the Kohn-Sham MO method of density-functional theory (DFT) in principle yields exact energies and, in practice, with the available density functionals for exchange and correlation, rather accurate energies, we have the special situation that a seemingly one-particle model (a MO method) in principle completely accounts for the bonding energy.^[21a]

The orbital interaction energy can be decomposed into the contributions from each irreducible representation Γ of the interacting system (Eq. 6.3) using the extended transition state (ETS) scheme developed by Ziegler and Rauk^[21c-e] (note that our approach differs in this respect from the Morokuma scheme,^[22] which instead attempts a decomposition of the orbital interactions into polarization and charge transfer):

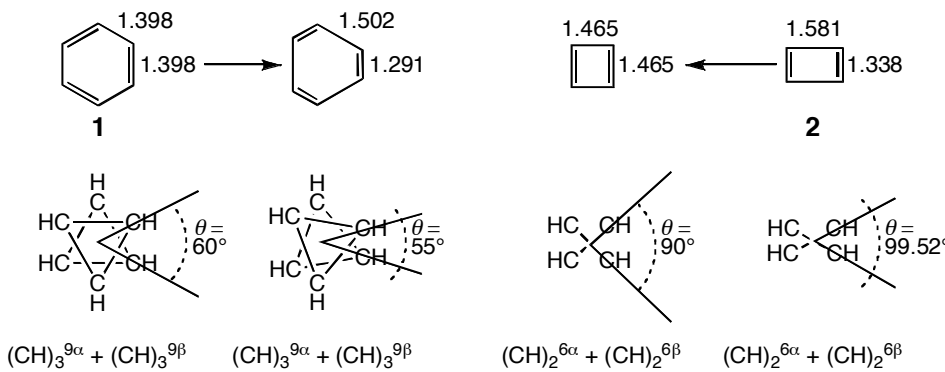
$$\Delta E_{\text{oi}} = \sum_{\Gamma} \Delta E_{\Gamma} = \Delta E_{\sigma} + \Delta E_{\pi} \quad (6.3)$$

In our model systems, the irreducible representations can be categorized into symmetric and antisymmetric with respect to the mirror plane provided by the carbon-atom framework, which correspond to what is commonly designated σ and π electron systems, respectively. This gives rise to the orbital-interaction components ΔE_{σ} and ΔE_{π} , as shown in Eq. 6.3 above.

6.3 Results and Discussions

First, we focus on benzene (**1**) and 1,3-cyclobutadiene (**2**) for which we find the usual D_{6h} and D_{2h} symmetric equilibrium geometries: **1** has six equivalent C–C bonds of 1.398 Å and **2** has alternating short and long bonds of 1.338 and 1.581 Å (see Scheme 6.1). To understand why **1** opposes to localization and **2** undergoes localization, we have examined the energy and bonding of these species along a distortion mode proceeding from a regular delocalized structure with all C–C bonds equivalent towards a geometry with alternating single and double bonds. A key step in our approach is that this can be done by rotating two equivalent and geometrically frozen fragments relative to each other, as shown in Scheme 6.1, which greatly reduces the complexity of the bond analysis because we go from a multi-fragment to a two-fragment problem. For benzene, we go from D_{6h} symmetric **1** with all C–C bonds at 1.398 Å to a D_{3h} symmetric structure with alternating C–C bonds of 1.291 and 1.502 Å. For comparison, the C–C bond lengths in ethylene and ethane are, at the same level of theory, 1.333 and 1.532 Å. In the case of cyclobutadiene, we go from a D_{4h} symmetric species with all C–C bonds at 1.465 Å to the D_{2h} symmetric **2** with alternating C–C bonds of 1.338 and 1.581 Å. Note that along this distortion of cyclobutadiene, we preserve the singlet electron configuration of the equilibrium structure **2**, as we wish to understand the behavior of the latter (the D_{4h} arrangement has a triplet ground state which is 5.19 kcal/mol above **2** and has C–C bonds of 1.444 Å).

Scheme 6.1 Construction and distortion of **1** and **2** in terms of two rigid fragments.



At this point, we note that, although physically quite plausible, our choices of deformation modes, in particular the nonequilibrium localized benzene and delocalized 1,3-cyclobutadiene geometries, are not unique. We have therefore verified that all trends and conclusions that play a role in the following discussion are not affected if other plausible choices are made. Thus, we have analyzed the bonding in benzene, analogously to the procedure defined in Scheme 6.1 but proceeding from a localized benzene structure with alternating C–C distances of 1.333 and 1.532 Å, i.e., the C–C bond distances in ethene and ethane (the corresponding delocalized structure has C–C distances of 1.434 Å). Likewise, we

repeated our analyses for 1,3-cyclobutadiene by proceeding from the delocalized equilibrium geometry of the triplet ground state with equal C–C bonds of 1.444 Å (the corresponding localized geometry has alternating C–C bonds of 1.319 and 1.559 Å). The results (not shown here) for this alternative choice of deformation mode fully reproduce and confirm all trends and conclusions that we obtain with the definition of Scheme 6.1 (shown in Figures 6.1 and 6.2). The same holds also for yet another plausible choice for a cyclohexatriene-like benzene structure with alternating C–C bonds of 1.330 and 1.480 Å that correspond to the single and double bonds in 1,3-butadiene (results not shown). We conclude that whereas the precise numerical values vary somewhat, the trends that are essential for our conclusions are quite robust regarding the exact choice of the deformation mode.

Now we return to the discussion of our analyses of the deformation modes defined in Scheme 6.1. In our approach, the change in energy ΔE that goes with localizing our model systems is equal to the change in interaction energy ΔE_{int} between two geometrically frozen $(\text{CH})_3^{9^{\bullet}}$ fragments in their decet valence configuration for benzene and two $(\text{CH})_2^{6^{\bullet}}$ fragments in their septet valence configuration for cyclobutadiene. The preparation energy ΔE_{prep} vanishes in this analysis because it is constant for geometrically frozen fragments. Each pair of fragments has mutually opposite spins (superscripts α and β in Scheme 6.1) to allow for the formation of all σ and π electron-pair bonds. These $(\text{CH})_3^{9^{\bullet}}$ and $(\text{CH})_2^{6^{\bullet}}$ fragments are weakly (compared to the bonding interactions in **1** and **2**) repulsive conglomerates of three and two $\text{CH}^{3^{\bullet}}$ radicals, respectively. The changes in interaction can be analyzed within the conceptual framework of the MO model contained in Kohn-Sham DFT by decomposing ΔE_{int} into classical electrostatic attraction (ΔV_{elstat}), Pauli repulsive orbital interactions between same-spin electrons (ΔE_{Pauli}) and the (mainly electron-pair) bonding orbital interactions (ΔE_{oi}).^[21] As pointed out in the methodological section, the latter can be symmetry decomposed into contributions from the σ and π orbital interactions: $\Delta E_{\text{oi}} = \Delta E_{\sigma} + \Delta E_{\pi}$.^[14,15] Thus, we have

$$\Delta E_{\text{int}} = \Delta E_{\text{Pauli}} + \Delta E_{\sigma} + \Delta E_{\pi} + \Delta V_{\text{elstat}} \quad (6.4)$$

And because in our construction of **1** and **2** the π electrons contribute no Pauli repulsion (*vide infra*), we can write

$$\Delta E_{\text{int}} = \text{"total } \sigma\text{"} + \text{"total } \pi\text{"} + \Delta V_{\text{elstat}}, \quad (6.5)$$

with "total σ " = $\Delta E_{\text{Pauli}} + \Delta E_{\sigma}$ and "total π " = ΔE_{π} .

The results of our analyses, in Figures 6.1 and 6.2, show that indeed it is the π electrons that determine if an aromatic, delocalized geometry occurs or an antiaromatic one with localized double bonds. In the first place, not unexpectedly, the energy of D_{6h} symmetric benzene (**1**) rises on localization whereas localization of the D_{4h} symmetric arrangement of cyclobutadiene towards **2** goes with a stabilization (black bold curves in Figures 6.1a,b). Now

it appears that the σ electron system always (i.e., in **1** as well as **2**) opposes to this localization whereas the π electron system always promotes the very same localization of double bonds (compare blue "total σ " with red "total π " curves in Figures 6.1a,b).

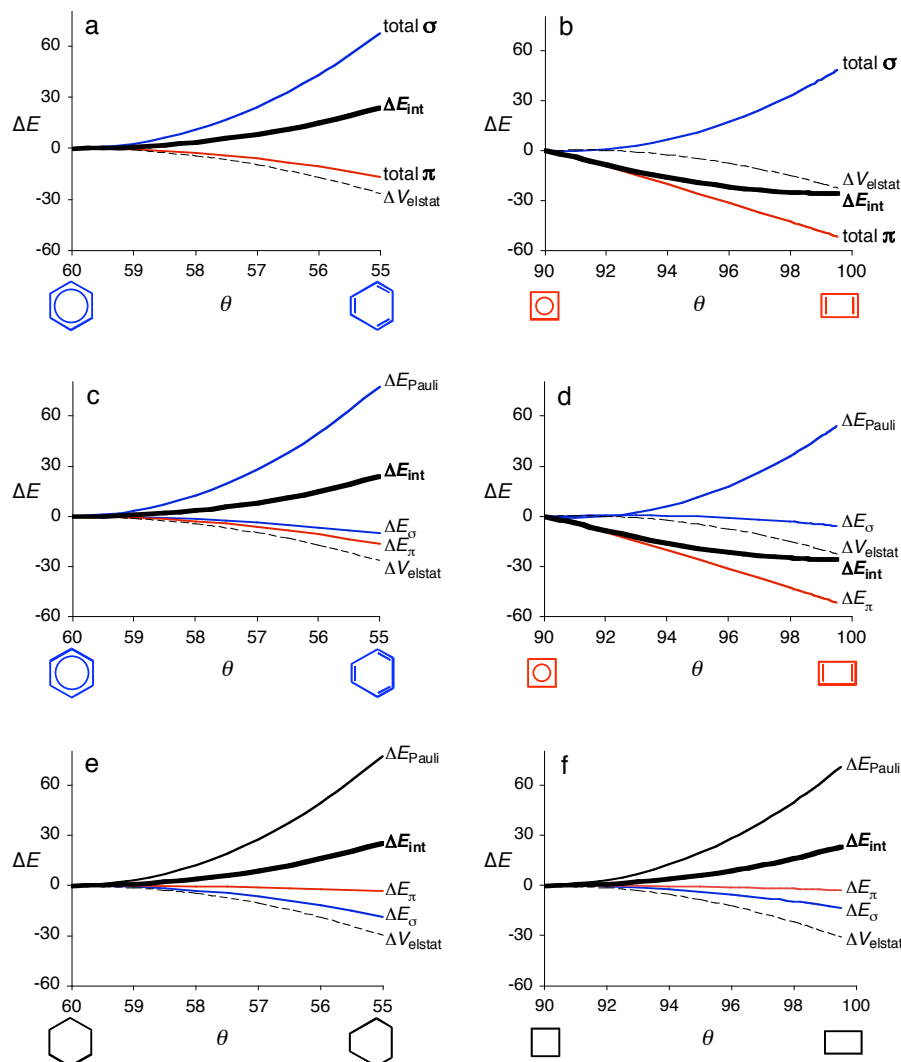


Figure 6.1 Bond energy decomposition (in kcal/mol) of **1**, **2**, **3** and **4**, each constructed from two equivalent rigid fragments, as function of the distortion mode (in deg) from delocalized to localized structure as defined for **1** and **2** in Scheme 6.1. $\Delta E_{\text{int}} = (\Delta E_{\text{Pauli}} + \Delta E_{\sigma}) + [\Delta E_{\pi}] + \Delta V_{\text{elstat}} = (\text{total } \sigma) + [\text{total } \pi] + \Delta V_{\text{elstat}}$ computed at BP86/TZ2P.

Interestingly, there is a marked difference between the localizing force that the respective π electron systems exert on the ring geometry in **1** and **2**. In the antiaromatic ring system, the propensity of the π system to localize the double bonds is dramatically increased as compared to the aromatic ring (compare red "total π " curve in Figure 6.1a with that in Figure 6.1b). This becomes even clearer if we convert ΔE_{int} and its components into energies per C–C bond (or, which is equivalent, per π electron) and superimpose the resulting diagrams of **1** and **2** in Figure 6.2a. Here we can see that the tendency per σ electron to resist localization is

essentially equal in **1** (blue curves) and **2** (red curves). Likewise, the classical electrostatic attraction ΔV_{elstat} , which slightly favors localization, is essentially equal in **1** and **2**. The discriminating factor is the tendency per π electron to localize the geometry which is about three times larger in the antiaromatic species (**2**) than in the aromatic one (**1**). Similar results are obtained for the alternative distortions that were presented earlier in the manuscript.

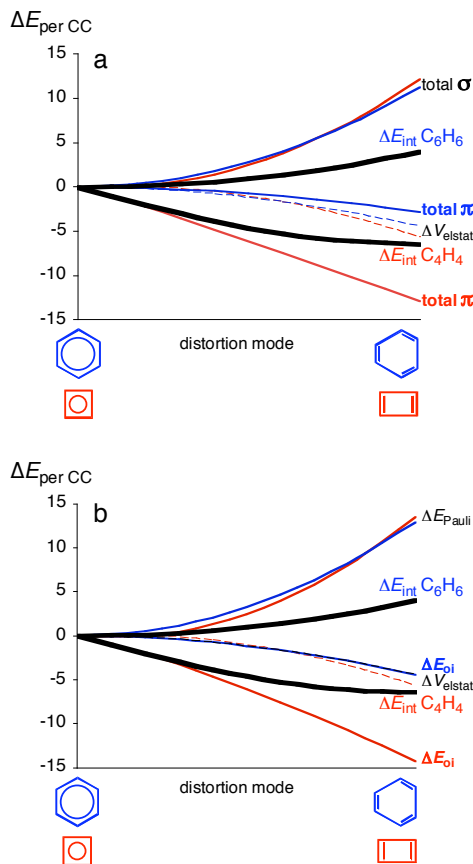


Figure 6.2 Bond energy decomposition (in kcal/mol) divided by the number of C–C bonds of **1** and **2** superimposed, each constructed from two equivalent rigid fragments, as function of the distortion mode from delocalized to localized structure as defined in Scheme 6.1. $\Delta E_{\text{int}} = (\Delta E_{\text{Pauli}} + \Delta E_{\text{o}}) + [\Delta E_{\pi}] + \Delta V_{\text{elstat}} = (\text{total } \sigma) + [\text{total } \pi] + \Delta V_{\text{elstat}}$ computed at BP86/TZ2P.

How can we understand the above? The σ bonds are characterized by an equilibrium distance greater than zero, roughly 1.5 Å for C–C bonds. One reason for this is the early onset of $\langle 2p_{\sigma}|2p_{\sigma} \rangle$ compared to $\langle 2p_{\pi}|2p_{\pi} \rangle$ overlap and the fact that the former achieves an optimum at distances greater than zero whereas the latter is maximal at distance zero (see also Ref. [23]). This is illustrated in Figure 6.3 for two C–H^{***} fragments in benzene approaching each other on localization (see black curves). However, as pointed out before in a different context,^[24] the main reason for σ bonds to feature an optimum distance greater than zero is the repulsive wall provided by Pauli repulsion with the closed shell 2s (and 1s) AOs on carbon and the C–H bonds. In the symmetric, delocalized structures of benzene and

cyclobutadiene, each C–C bond is already forced by partial π bonding below the optimum σ distance, i.e., it is already in the region where the Pauli repulsion ΔE_{Pauli} due to the σ electrons goes up in energy faster than the stabilizing orbital interactions ΔE_{σ} and ΔV_{elstat} together go down. This becomes clear if one separates "total σ ", shown in Figures 6.1a,b and 6.2a, into its component $\Delta E_{\text{Pauli}} + \Delta E_{\sigma}$ as has been done in Figures 6.1c,d and 6.2b.

The π electron systems, on the other hand, only provide electron-pair bonding and *no* Pauli repulsive orbital interactions, as can be seen in Figure 6.4. They achieve an optimum overlap at zero bond distance (see Figure 6.3). But why is the localizing propensity of the π system in **1** so little pronounced whereas it is so prominent in **2**? Essential for understanding this difference is the qualitatively different topology and geometry dependence of the π overlaps in our aromatic and antiaromatic 6 and 4 π -electron systems as compared to a simple 2 π -electron system which is represented by the black $\langle 2p_{\pi}|2p_{\pi}' \rangle$ curve in Figure 6.3. Scheme 6.2 extracts from Figure 6.4 the key features that emerge from our quantitative Kohn-Sham MO analyses.

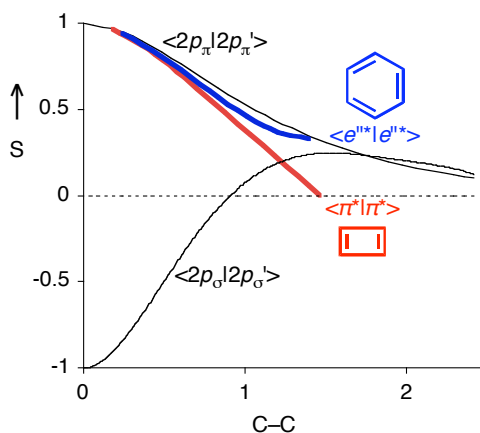


Figure 6.3 Selected overlap integrals between MOs of two $\text{CH}^{''''}$ units in **1** (black curves), between MOs of two $(\text{CH})_3^{''''}$ units in **1** (blue curve), and between two $(\text{CH})_2^{''''}$ units in **2** (red curve) as function of the C–C distance (in Å) along the localization distortion defined in Scheme 6.1.

The main difference between π overlap in **1** and **2** versus that between two simple $\text{CH}^{''''}$ fragments is the occurrence of counteracting effects, on localization, in **1** and amplifying effects in **2**. Whereas the $\langle 2p_{\pi}|2p_{\pi}' \rangle$ overlap between two $\text{CH}^{''''}$ fragments smoothly increases from 0 (at C–C = ∞) towards the value 1 (at C–C = 0), the π bonding a'' MOs in both **1** and **2** gain and loose bonding overlap in the shrinking and expanding C–C bonds, respectively (see Figure 6.3; see also Figure 6.4). Eventually, the net effect is still a gain in bonding but in essence this is not so pronounced anymore (see Scheme 6.2). The same holds for the π bonding set of degenerate e'' MOs in **1** (see Scheme 6.2: stabilizing and destabilizing effects are indicated for one of these e'' MOs with + and – signs, respectively). This makes benzene's π system comparatively indifferent with respect to localizing the double C–C bonds.

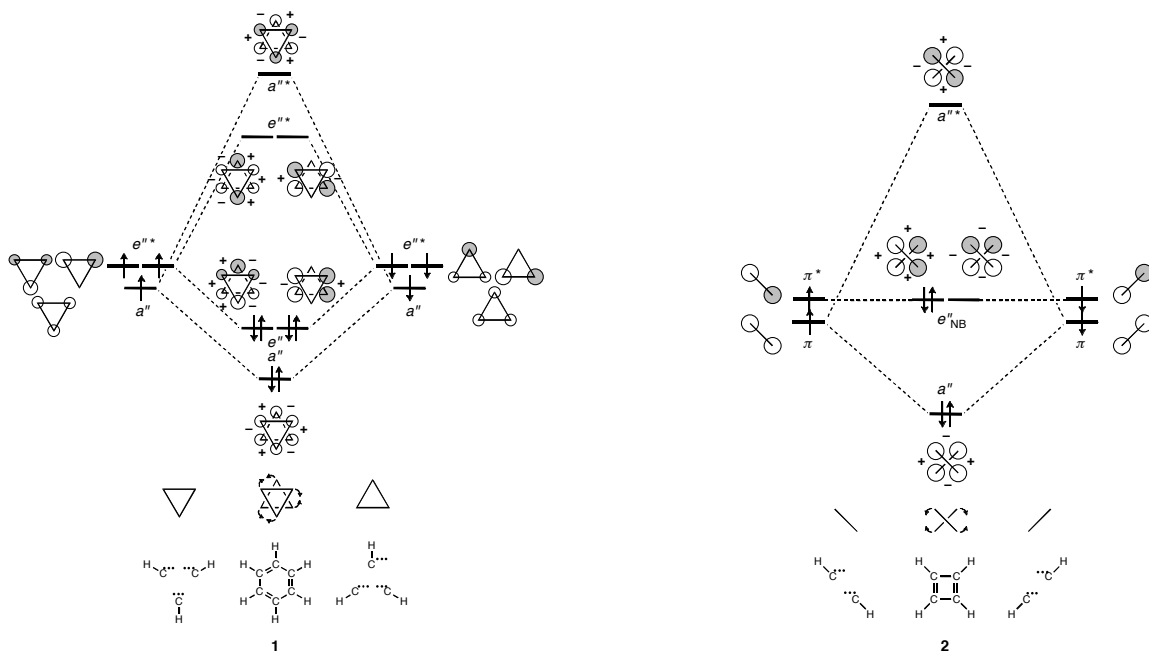
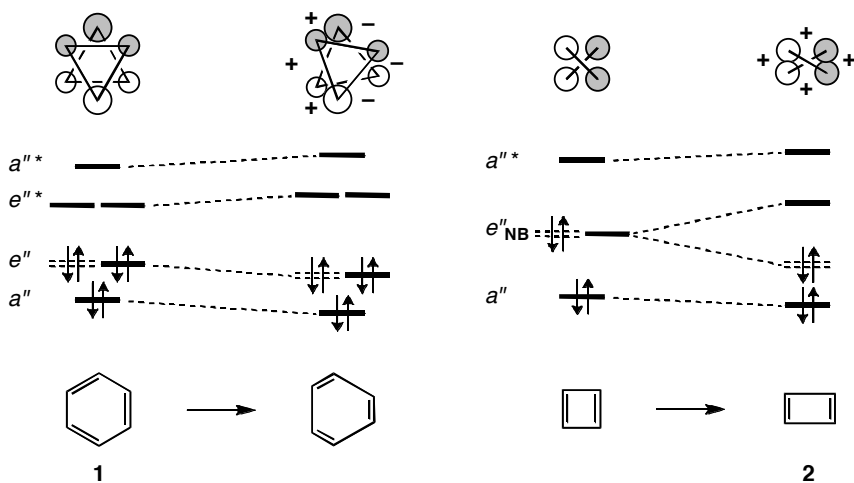


Figure 6.4 Schematic π MO interaction diagram of benzene (**1**, left panel) constructed from two $(CH_3)_3^{9\sigma}$ fragments in their decet valence configuration, and of 1,3-cyclobutadiene (**2**, right panel) constructed from two $(CH_3)_3^{6\sigma}$ fragments in their septet valence configuration based on Kohn-Sham MO analyses at BP86/TZ2P. There are respectively 3 and 2 π electrons in each of the two fragments which have mutually opposite spin. The effect on orbital energies of the localization mode defined in Scheme 6.1 and represented here with curved arrows is indicated by + (stabilization) and - (destabilization).

A completely different situation holds for the nonbonding degenerate e''_{NB} MOs in the second-order Jahn-Teller unstable D_{4h} -symmetric geometry of cyclobutadiene.^[23] One of these π MOs gains, on localization, stabilization in every C–C bond (this is indicated with the + signs in Scheme 6.2). And it does so rapidly. This is because the orbital overlap starts to build up from 0 (i.e., no overlap and no stabilization) at a short C–C distance of 1.465 Å and rises to the value 1 as the C–C distance decreases to 0 (see Figure 6.3). This differs from the distance dependence of the π overlap between two $2p_\pi$ AOs on two simple CH^{***} fragments (or on two carbon atoms) which has its zero point at a C–C distance of ∞ but also goes to 1 as the C–C distance decreases to 0 Å (see $\langle 2p_\pi | 2p_\pi' \rangle$ in Figure 6.3). Along the bond localizing distortion, the gain in overlap between the two π^* $(CH_2)_2^{6\sigma}$ fragment MOs (shown in Figure 6.4) is a sizeable 0.102! (see Figure 6.3). [The corresponding gain in overlap between two e''^* $(CH_3)_3^{9\sigma}$ fragment MOs that form a π bonding e'' MO in benzene shown in Figure 6.4 amounts to only 0.012 (see Figure 6.3).] As a consequence, this cyclobutadiene MO, which is fully occupied in the singlet ground state of **2**, drops markedly in energy along the localization mode. This lends cyclobutadiene's π system its enhanced propensity towards localization of the double C–C bonds.

Scheme 6.2 Effect of localization on π MO levels of **1** and **2**.
Orbital plots at top refer to dashed levels.



Furthermore, it is instructive to compare the aromatic **1** and antiaromatic **2** with the corresponding saturated nonaromatic **3** and **4**. For clarity and comparability, this is done for planar **3** and **4** which are 24.5 and 0.9 kcal/mol above the chair and puckered-ring equilibrium conformations, respectively. The latter are obtained from **1** and **2** by saturating the double bonds with hydrogen which comes down to occupying the antibonding π orbitals. For the six-membered ring, the transformation of **1** to **3** has relatively little effect. Of course, the C–C bonds expand (from 1.398 to 1.557 Å) as the net π bonding vanishes. But the regular, delocalized structure remains as it was anyway determined by the σ system which is practically unchanged. This is illustrated by our quantitative bond energy decomposition of **3** and **4** constructed in analogy to **1** and **2** from two $(\text{CH}_2)_3^{6*}$ or two $(\text{CH}_2)_2^{4*}$ fragments. Indeed there are relatively little changes from **1** to (planar) **3**: the most important one is that the anyway small ΔE_π term of **1** becomes even smaller in **3** (see Figures 6.1c and 6.1e). In the case of the four-membered ring, the changes from **2** to **4** are more drastic. Here, saturation of the double bonds eliminates the strongly localizing π bonding component which, as a consequence, can no longer overrule the delocalizing σ system. Thus, the latter causes **4** to adopt a regular structure with four equal C–C bonds of 1.559 Å. This is clearly seen by comparing Figures 6.1d and 6.1f in which the main change is the collapse of the ΔE_π component.

Finally, these conclusions also stresses an important difference between the issue of (anti)aromaticity, e.g., benzene versus 1,3-cylobutadiene, and the issue of (non)hypervalence, e.g., C versus Si. Both concepts deal with the propensity of a system to localize or delocalize bonds. However, the question whether a species is aromatic or antiaromatic is a purely electronic problem (i.e., determined by bonding orbital interactions) whereas steric factors (i.e., Pauli repulsive orbital interactions) play a key role in the question if an atom has the capability to form stable hypervalent structures with its substituents or not.^[25]

6.4 Conclusions

In conclusion, our MO model of aromaticity augments and confirms the modern VB picture developed by Shaik and Hiberty. This MO model shows that indeed the π electron system never favors a symmetric, delocalized ring, neither in benzene (**1**) nor in cyclobutadiene (**2**). The regular, symmetric structure of benzene has the same cause as that of planar cyclohexane (**3**), namely, the σ electron system. Yet, the π system decides if delocalization occurs by showing qualitatively different geometry-dependence of the π overlap in **1** and **2**. In the aromatic species, the localizing propensity of the π system emerges from a subtle interplay of counteracting overlap effects and is therefore too little pronounced to overcome the delocalizing σ system. At variance, in the antiaromatic ring, all π overlap effects unidirectionally favor localization of the double bonds and can, in this way, overrule the σ system.

References

- [1] (a) A. Kekulé, *Bull. Soc. Chim. Paris* **1865**, 3, 98; (b) Benzene was first isolated by Faraday: M. Faraday, *Phil. Trans. R. Soc. London* **1825**, 440.
- [2] (a) P. J. Garratt, *Aromaticity*, John Wiley & Sons, Inc, New York, **1986**; (b) V. I. Minkin, M. N. Glukhotsev, B. Y. Simkin, *Aromaticity and Antiaromaticity: Electronic and Structural Aspects*, John Wiley & Sons, Inc, New York, **1994**; (c) F. Bickelhaupt, W. H. de Wolf, *Recl. Trav. Chim. Pays-Bas* **1988**, 107, 459; (d) P. A. Kraakman, J.-M. Valk, H. A. G. Niederländer, D. B. E. Brouwer, F. M. Bickelhaupt, W. H. de Wolf, F. Bickelhaupt, C. H. Stam, *J. Am. Chem. Soc.* **1990**, 112, 6638.
- [3] P. v. R. Schleyer, H. J. Jiao, *Pure Appl. Chem.* **1996**, 68, 209.
- [4] F. A. Carey, R. J. Sundberg, *Advanced Organic Chemistry: Structure And Mechanisms (Part A)*, Springer, New York, **2000**.
- [5] Special issue on: *Aromaticity*, ed. P. v. R. Schleyer, *Chem. Rev.* **2001**, 101.
- [6] Special issue on: *Delocalization—pi and sigma*, ed. J. A. Gladysz, *Chem. Rev.* **2005**, 105.
- [7] (a) R. Breslow, *Acc. Chem. Res.* **1973**, 6, 393; (b) T. M. Krygowski, M. K. Cyranski, Z. Czarnocki, G. Hafelinger, A. R. Katritzky, *Tetrahedron* **2000**, 56, 1783; (c) P. v. R. Schleyer, *Chem. Rev.* **2001**, 101, 1115; (d) M. K. Cyranski, T. M. Krygowski, A. R. Katritzky, P. v. R. Schleyer, *J. Org. Chem.* **2002**, 67, 1333.
- [8] (a) L. Pauling, *J. Am. Chem. Soc.* **1926**, 48, 1132; (b) L. Pauling, *The Nature of the Chemical Bond*, 3rd ed., Cornell University Press: Ithaca, New York, **1960**.
- [9] E. Hückel, *Z. Phys.* **1931**, 70, 204.
- [10] M. J. Goldstein, R. Hoffmann, *J. Am. Chem. Soc.* **1971**, 93, 6193.
- [11] (a) P. C. Hiberty, S. S. Shaik, J. M. Lefour, G. Ohanessian, *J. Org. Chem.* **1985**, 50, 4657; (b) S. S. Shaik, P. C. Hiberty, *J. Am. Chem. Soc.* **1985**, 107, 3089; (c) P. C. Hiberty, S. S. Shaik, G. Ohanessian, J. M. Lefour, *J. Org. Chem.* **1986**, 51, 3908; (d) S. S. Shaik, P. C. Hiberty, J. M. Lefour, G. Ohanessian, *J. Am. Chem. Soc.* **1987**, 109, 363; (e) S. S. Shaik, P. C. Hiberty, G. Ohanessian, J. M. Lefour, *J. Phys. Chem.* **1988**, 92, 5086; (f) P. C. Hiberty, D. Danovich, A. Shurki, S. Shaik, *J. Am. Chem. Soc.* **1995**, 117, 7760; (g) A. Shurki, S. Shaik, *Angew. Chem.* **1997**, 109, 2322; *Angew. Chem. Int. Ed. Engl.* **1997**, 36, 2205; (h) S. Shaik, A. Shurki, D. Danovich, P. C. Hiberty, *Chem. Rev.* **2001**, 101, 1501.

- [12] (a) F. Dijkstra, J. H. van Lenthe, R. W. A. Havenith, L. W. Jenneskens, *Int. J. Quantum Chem.* **2003**, *91*, 566; (b) Y. R. Mo, P. v. R. Schleyer, *Chem. Eur. J.* **2006**, *12*, 2009.
- [13] I. Fernández, G. Frenking, *Faraday Discuss.* **2007**, *135*, 403.
- [14] (a) Y. Ooshika, *J. Phys. Soc. Japan* **1957**, *12*, 1238; (b) H. Labhart, *J. Chem. Phys.* **1957**, *27*, 947; (c) H. C. Longuet-Higgins, L. Salem, *Proc. R. Soc. London, A* **1959**, *251*, 172; (d) M. Tsui, S. Huzinaga, T. Hasino, *Rev. Mod. Phys.* **1960**, *32*, 425; (e) R. S. Berry, *J. Chem. Phys.* **1961**, *35*, 2253.
- [15] (a) Y. Haas, S. Zilberg, *J. Am. Chem. Soc.* **1995**, *117*, 5387; (b) E. Heilbronner, *J. Chem. Educ.* **1989**, *66*, 471; (c) A. Stanger, K. P. C. Vollhardt, *J. Org. Chem.* **1988**, *53*, 4889; (d) N. D. Epiotis, *Pure Appl. Chem.* **1983**, *55*, 229.
- [16] W. Kutzelnigg, *Einführung in die Theoretische Chemie, Band 2, Die chemische Bindung*, Verlag Chemie, Weinheim, **1978**, Section 11.11.
- [17] (a) N. C. Baird, *J. Org. Chem.* **1986**, *51*, 3907; (b) E. D. Glendening, R. Faust, A. Streitwieser, K. P. C. Vollhardt, F. Weinhold, *J. Am. Chem. Soc.* **1993**, *115*, 10952.
- [18] (a) K. Jug, A. M. Koster, *J. Am. Chem. Soc.* **1990**, *112*, 6772; (b) A. Gobbi, Y. Yamaguchi, G. Frenking, H. F. Schaefer III, *Chem. Phys. Lett.* **1995**, *244*, 27; (c) B. Kovacevic, D. Baric, Z. B. Maksic, T. Müller, *ChemPhysChem* **2004**, *5*, 1352; (d) A. Rehaman, A. Datta, S. S. Mallajosyula, S. K. Pati, *J. Chem. Theory Comput.* **2006**, *2*, 30.
- [19] (a) R. Hoffmann, *Angew. Chem.* **1982**, *94*, 725; *Angew. Chem. Int. Ed. Engl.* **1982**, *21*, 711; (b) For an instructive discussion on the pros and cons of MO versus VB theory, see: R. Hoffmann, S. Shaik, P. C. Hiberty, *Acc. Chem. Res.* **2003**, *36*, 750.
- [20] (a) G. te Velde, F. M. Bickelhaupt, E. J. Baerends, C. Fonseca Guerra, S. J. A. van Gisbergen, J. G. Snijders, T. Ziegler, *J. Comput. Chem.* **2001**, *22*, 931; (b) C. Fonseca Guerra, O. Visser, J. G. Snijders, G. te Velde, E. J. Baerends, in *Methods and Techniques for Computational Chemistry*, (Eds.: E. Clementi, G. Corongiu), STEF: Cagliari, **1995**, p. 305-395; (c) E. J. Baerends, D. E. Ellis, P. Ros, *Chem. Phys.* **1973**, *2*, 41; (d) E. J. Baerends, P. Ros, *Chem. Phys.* **1975**, *8*, 412; (e) E. J. Baerends, P. Ros, *Int. J. Quantum. Chem. Symp.* **1978**, *12*, 169; (f) C. Fonseca Guerra, J. G. Snijders, G. te Velde, E. J. Baerends, *Theor. Chem. Acc.* **1998**, *99*, 391; (g) P. M. Boerrigter, G. te Velde, E. J. Baerends, *Int. J. Quantum Chem.* **1988**, *33*, 87; (h) G. te Velde, E. J. Baerends, *J. Comp. Phys.* **1992**, *99*, 84; (i) J. G. Snijders, E. J. Baerends, P. Vernooij, *At. Nucl. Data Tables* **1982**, *26*, 483; (j) J. Krijn, E. J. Baerends, *Fit-Functions in the HFS-Method; Internal Report (in Dutch)*, Vrije Universiteit, Amsterdam, **1984**; (k) L. Versluis, T. Ziegler, *J. Chem. Phys.* **1988**, *88*, 322; (l) J. C. Slater, *Quantum Theory of Molecules and Solids, Vol. 4*, McGraw-Hill, New York, **1974**; (m) A. D. Becke, *J. Chem. Phys.* **1986**, *84*, 4524; (n) A. Becke, *Phys. Rev. A* **1988**, *38*, 3098; (o) S. H. Vosko, L. Wilk, M. Nusair, *Can. J. Phys.* **1980**, *58*, 1200; (p) J. P. Perdew, *Phys. Rev. B* **1986**, *33*, 8822 (Erratum: *Phys. Rev. B* **1986**, *34*, 7406); (q) L. Fan, T. Ziegler, *J. Chem. Phys.* **1991**, *94*, 6057.
- [21] (a) F. M. Bickelhaupt, E. J. Baerends, in *Review in Computational Chemistry* Vol. 15, **2000**, pp. 1; (b) F. M. Bickelhaupt, N. M. M. Nibbering, E. M. van Wezenbeek, E. J. Baerends, *J. Phys. Chem.* **1992**, *96*, 4864; (c) T. Ziegler, A. Rauk, *Inorg. Chem.* **1979**, *18*, 1755; (d) T. Ziegler, A. Rauk, *Inorg. Chem.* **1979**, *18*, 1558; (e) T. Ziegler, A. Rauk, *Theor. Chim. Acta* **1977**, *46*, 1.
- [22] K. Morokuma, *Acc. Chem. Res.* **1977**, *10*, 294.
- [23] T. A. Albright, J. K. Burdett, M.-H. Whangbo, *Orbital Interactions in Chemistry*, John Wiley & Sons Inc, New-York, **1985**.
- [24] (a) F. M. Bickelhaupt, E. J. Baerends, *Angew. Chem.* **2003**, *115*, 4315; *Angew. Chem. Int. Ed.* **2003**, *42*, 4183; (b) F. M. Bickelhaupt, R. L. DeKock, E. J. Baerends, *J. Am. Chem. Soc.* **2002**, *124*, 1500.
- [25] S. C. A. H. Pierrefixe, C. Fonseca Guerra, F. M. Bickelhaupt, *Chem. Eur. J.* **2008**, *14*, 819.

7 Aromaticity and Antiaromaticity in 4-, 6-, 8- and 10-Membered Conjugated Hydrocarbon Rings

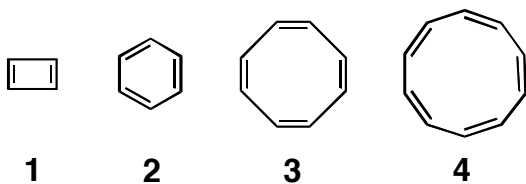
Adapted from S. C. A. H. Pierrefixe and F. M. Bickelhaupt
J. Phys. Chem. A **2008**, Accepted

Abstract

Recently, we presented an MO model of aromaticity that explains, in terms of simple orbital-overlap arguments, *why* benzene (C_6H_6) has a regular structure with delocalized double bonds while the geometry of 1,3-cyclobutadiene (C_4H_4) is distorted with localized double bonds. Here, we show that the same model and the same type of orbital-overlap arguments also account for the irregular and regular structures of 1,3,5,7-cyclooctatetraene (C_8H_8) and 1,3,5,7,9-cyclodecapentaene ($C_{10}H_{10}$), respectively. Our MO model is based on accurate Kohn-Sham DFT analyses of the bonding in C_4H_4 , C_6H_6 , C_8H_8 and $C_{10}H_{10}$, and how the bonding mechanism is affected if these molecules undergo geometrical deformations between regular, delocalized ring structures and distorted ones with localized double bonds. The propensity of the π electrons is always to *localize* the double bonds, against the delocalizing force of the σ electrons. Importantly, we show that the π electrons nevertheless decide about the localization (in C_4H_4 and C_8H_8) or delocalization of the double bonds (in C_6H_6 and $C_{10}H_{10}$).

7.1 Introduction

Aromaticity and antiaromaticity of compounds as well as the very concepts themselves have been the subject in many experimental and theoretical studies.^[1,2] The key characteristics of aromatic compounds are: (i) a regular, delocalized structure involving C–C bonds of equal length, each with partial double-bond character, (ii) enhanced thermodynamic stability, and (iii) reduced reactivity as compared to nonaromatic conjugated hydrocarbons. Antiaromatic compounds show exactly the opposite: (i) an irregular structure with alternating single and localized double C–C bonds, (ii) reduced thermodynamic stability, and (iii) enhanced reactivity.

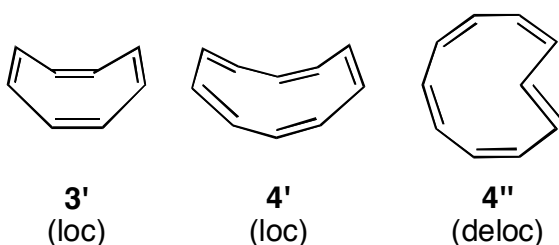


Recently, in a quantitative Kohn-Sham molecular orbital (MO) study, we addressed the question *why* the antiaromatic 1,3-cyclobutadiene (**1**) and aromatic benzene rings (**2**) have localized and delocalized structures, respectively.^[3] Our MO model showed that the π electron system never favors a symmetric, delocalized ring, neither in **1** nor in **2**. The regular, symmetric structure of benzene (**2**) appears to have the same cause as that of planar cyclohexane, namely, the σ electron system. And yet, may be somewhat counterintuitively, at first sight, it is the π system which decides if delocalization occurs or not. The mechanism behind this control is a qualitatively different geometry-dependence of the π overlap in **1** and **2**. In the aromatic species **2**, the localizing propensity of the π system emerges from a subtle interplay of counteracting overlap effects and is therefore too little pronounced to overcome the delocalizing σ system. At variance, in the antiaromatic ring **1**, all π overlap effects unidirectionally favor localization of the double bonds and can, in this way, overrule the σ system.^[3]

Our work echoes with earlier theoretical and experimental studies on aromaticity. Initially, Hückel ascribed the driving force for delocalization in benzene and other circularly conjugated $4n+2$ π -electron species to the π electron system.^[4,5] Note that this disagrees in a subtle, yet essential manner with our findings.^[3] The latter point to a key role for the π electrons in determining whether localization of the double bonds occurs but they do so *rather as a regulating factor, not as the driving force* for this localization. In fact, evidence against the idea that benzene's D_{6h} symmetric structure originates from a delocalizing propensity of its π -electron system, has been reported already since the late 1950's.^[6,7] More recently, Shaik, Hiberty and coworkers^[8] showed in terms of an elegant VB model that it is the σ system that enforces the delocalized, D_{6h} symmetric structure of **2** upon the π system, which intrinsically strives for localized double bonds. These conclusions initiated a debate^[9]

but were eventually reconfirmed by others.^[3,10] this includes our MO model of aromaticity which nicely augments and confirms the modern VB picture developed by Shaik and Hiberty.

The purpose of the present paper is to explore if our MO model developed for 1,3-cyclobutadiene (**1**) and benzene (**2**) also extends to the next larger, formally Hückel-antiaromatic ($4n \pi$ electrons) and Hückel-aromatic ($4n+2 \pi$ electrons) conjugated hydrocarbons rings: 1,3,5,7-cyclooctatetraene (**3'**) and 1,3,5,7,9-cyclodecapentaene (**4'**). Note that **3'** and **4'** are no longer planar species as would be suggested by the qualitative structures **3** and **4**, shown above.^[5,11] Instead, cyclooctatetraene (**3'**) is a tub-shaped molecule with localized double bonds, as shown somewhat more realistically below. And also cyclodecapentaene adopts only nonplanar conformations, such as the boat- or saddle-shaped C_2 symmetric species, shown in **4''** ("twist conformation").^[11]



Interestingly, cyclodecapentaene, as compared to benzene, shows an increased tendency to *localize* its double bonds, despite the fact that it is formally aromatic according to Hückel's $4n+2 \pi$ -electron rule, with $n = 2$. Allen, Schaefer and coworkers^[11] have carried out an extensive exploration of the various conformations of **4**. They found that a C_2 symmetric conformation as shown schematically in **4'** is the lowest in energy at CCSD(T)//MP2. Furthermore, they found that whether the double bonds are delocalized or localized depends critically on the level of theory, but also on which particular conformation was considered. Conformation **4'** was found to *localize* its double bonds. On the other hand, the heart-shaped conformation **4''**, which is only 4.2 kcal/mol higher in energy than **4'**, was found to adopt a more delocalized structure with pronounced partial double-bond character in all C–C bonds.^[11] This behavior contrasts with the pronounced and robust propensity of benzene to adopt a symmetric, delocalized structure (**2**).^[3,5]

Thus, we have quantum chemically investigated the structure and bonding of **1**, **2**, **3**, **3'**, **4** and **4'** at the BP86/TZ2P level of density functional theory (DFT) using the ADF program.^[12] Our analyses show that the MO model developed previously for **1** and **2** is indeed also valid for **3** and **4**. The π -electron system is confirmed to have in all cases a propensity to *localize* double bonds, against the delocalizing force of the σ -electron system. This propensity is however only weakly pronounced in the case of the aromatic species (**2** and **4**). Simple orbital-overlap arguments account for this behavior as well as for the fact that the tendency of the π -electron system to localize the double bonds becomes stronger if one goes from the smaller benzene (**2**) to the larger cyclodecapentaene ring (**4**).

7.2 Theoretical Methods

7.2.1 General Procedure

All calculations were performed using the Amsterdam Density Functional (ADF) program developed by Baerends and others.^[12] The numerical integration was performed using the procedure developed by te Velde et al.^[12g,h] The MOs were expanded in a large uncontracted set of Slater type orbitals (STOs) containing diffuse functions: TZ2P (no Gaussian functions are involved).^[12i] The basis set is of triple- ζ quality for all atoms and has been augmented with two sets of polarization functions, i.e. 3d and 4f on C and 2p and 3d on H. The 1s core shell of carbon were treated by the frozen-core approximation.^[12c] An auxiliary set of s, p, d, f and g STOs was used to fit the molecular density and to represent the Coulomb and exchange potentials accurately in each self-consistent field cycle.^[12j]

Equilibrium structures were optimized using analytical gradient techniques.^[12k] Geometries and energies were calculated at the BP86 level of the generalized gradient approximation (GGA): exchange is described by Slater's X α potential^[12l] with corrections due to Becke^[12m,n] added self-consistently and correlation is treated in the Vosko-Wilk-Nusair (VWN) parameterization^[12o] with nonlocal corrections due to Perdew^[12p] added, again, self-consistently (BP86).^[12q] All stationary points were confirmed to be equilibrium structures (number of imaginary frequencies = NIMAG = 0), transition states (NIMAG = 1) or higher-order saddle points (NIMAG > 1) through vibrational analysis.

7.2.2 Bonding Energy Analysis

To obtain more insight into the nature of the bonding in our antiaromatic (**1** and **3**) and aromatic (**2** and **4**) systems, an energy decomposition analysis has been carried out.^[13] In this analysis, the total binding energy ΔE associated with forming the overall molecular species of interest, say AB, from two (or sometimes more) radical fragments, A' + B', is made up of two major components (Eq. 7.1):

$$\Delta E = \Delta E_{\text{prep}} + \Delta E_{\text{int}} \quad (7.1)$$

In this formula, the preparation energy ΔE_{prep} is the amount of energy required to deform the individual (isolated) radical fragments from their equilibrium structure (A', B') to the geometry that they acquire in the overall molecule (A, B). The interaction energy ΔE_{int} corresponds to the actual energy change when these geometrically deformed fragments A and B are combined to form the combined molecular species AB. It is analyzed in the framework of the Kohn-Sham Molecular Orbital (MO) model using a quantitative decomposition of the bond into electrostatic interaction, Pauli repulsion (or exchange repulsion or overlap repulsion), and (attractive) orbital interactions (Eq. 7.2).^[13]

$$\Delta E_{\text{int}} = \Delta V_{\text{elstat}} + \Delta E_{\text{Pauli}} + \Delta E_{\text{oi}} \quad (7.2)$$

The term ΔV_{elstat} corresponds to the classical electrostatic interaction between the unperturbed charge distributions $\rho_A(r) + \rho_B(r)$ of the prepared or deformed radical fragments A and B (*vide infra* for definition of the fragments) that adopt their positions in the overall molecule AB, and is usually attractive. The Pauli repulsion term, ΔE_{Pauli} , comprises the destabilizing interactions between occupied orbitals and is responsible for the steric repulsion. This repulsion is caused by the fact that two electrons with the same spin cannot occupy the same region in space. It arises as the energy change associated with the transition from the superposition of the unperturbed electron densities $\rho_A(r) + \rho_B(r)$ of the geometrically deformed but isolated radical fragments A and B to the wavefunction $\Psi^0 = N \hat{A} [\Psi_A \Psi_B]$, that properly obeys the Pauli principle through explicit antisymmetrization (\hat{A} operator) and renormalization (N constant) of the product of fragment wavefunctions (see Ref. [13a] for an exhaustive discussion). The orbital interaction ΔE_{oi} in any MO model, and therefore also in Kohn-Sham theory, accounts for electron-pair bonding,^[13a,b] charge transfer (i.e., donor–acceptor interactions between occupied orbitals on one moiety with unoccupied orbitals of the other, including the HOMO–LUMO interactions) and polarization (empty–occupied orbital mixing on one fragment due to the presence of another fragment). In the bond-energy decomposition, open-shell fragments are treated with the spin-unrestricted formalism but, for technical (not fundamental) reasons, spin-polarization is not included. This error causes an electron-pair bond to become in the order of a few kcal/mol too strong. To facilitate a straightforward comparison, the results of the energy decomposition were scaled to match exactly the regular bond energies. Since the Kohn-Sham MO method of density-functional theory (DFT) in principle yields exact energies and, in practice, with the available density functionals for exchange and correlation, rather accurate energies, we have the special situation that a seemingly one-particle model (a MO method) in principle completely accounts for the bonding energy.^[13a]

The orbital interaction energy can be decomposed into the contributions from each irreducible representation Γ of the interacting system (Eq. 7.3) using the extended transition state (ETS) scheme developed by Ziegler and Rauk^[13c-e] (note that our approach differs in this respect from the Morokuma scheme,^[14] which instead attempts a decomposition of the orbital interactions into polarization and charge transfer):

$$\Delta E_{\text{oi}} = \sum_{\Gamma} \Delta E_{\Gamma} = \Delta E_{\sigma} + \Delta E_{\pi} \quad (7.3)$$

In our model systems **1**, **2**, **3'** and **4'**, the irreducible representations can be categorized into symmetric and antisymmetric with respect to the mirror plane provided by the carbon-atom framework, which correspond to what is commonly designated σ and π electron systems, respectively. This gives rise to the orbital-interaction components ΔE_{σ} and ΔE_{π} , as shown in Eq. 7.3 above.

7.3 Results and Discussions

We find that 1,3-cyclobutadiene (**1**) and benzene (**2**) have planar D_{2h} and D_{6h} symmetric equilibrium geometries: **1** has alternating short and long bonds of 1.338 and 1.581 Å whereas **2** has six equivalent C–C bonds of 1.398 Å (see Scheme 7.1, upper). At variance, 1,3,5,7-cyclooctatetraene (**3'**) and 1,3,5,7,9-cyclodecapentaene (**4'**) adopt nonplanar equilibrium structures, in line with previous theoretical and experimental studies (see Section 7.1). We find that **3'** has the well-known tub-shaped conformation of S_4 symmetry with alternating short and long bonds of 1.345 and 1.472 Å. Likewise, **4'** adopts the saddle-shaped conformation with 10 essentially but not exactly equivalent C–C bonds of 1.40 Å. More precisely, the bond-length patterns is two times: four consecutive C–C bonds of 1.402 Å followed by one C–C bond of 1.403 Å. While this differs from the pronounced bond length alternation found by Allen and Schaefer at MP2,^[11] this result correctly indicates that **4'** still shows some aromatic character but the latter is much reduced as compared to benzene.

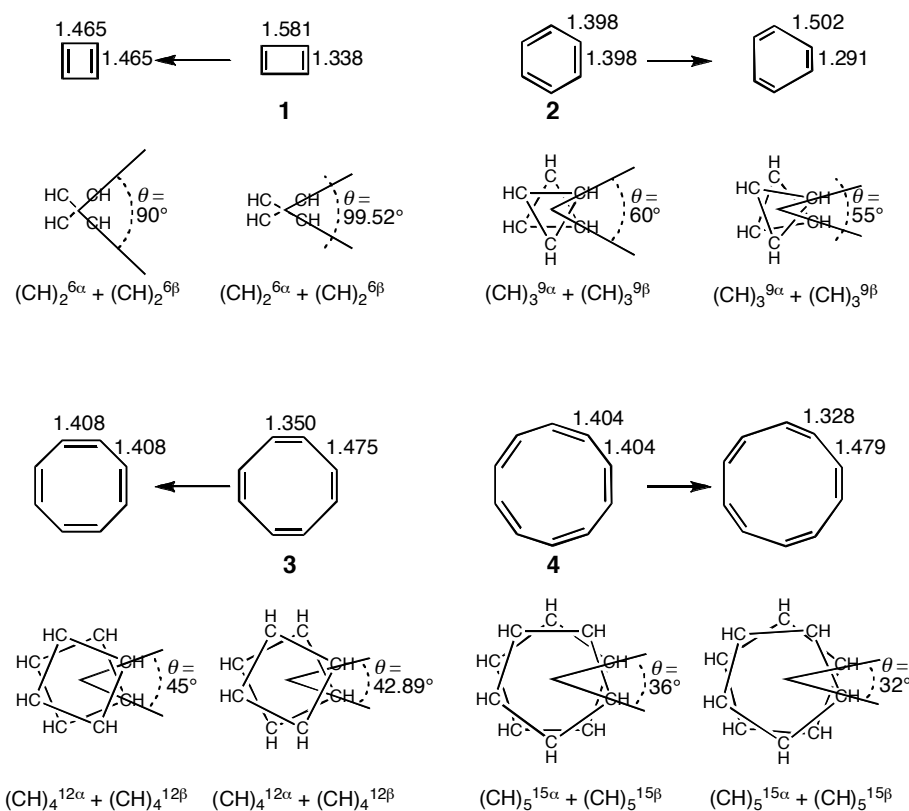
Making **3'** and **4'** planar, that is, going to the corresponding *planar* optimum geometries **3** and **4**, is associated with a destabilization of +9.67 and +3.38 kcal/mol, respectively. However, the characteristic antiaromatic and aromatic bond-length patterns are preserved after this planarization: the planar **3** is of D_{4h} symmetry and still has alternating short and long bonds of 1.350 and 1.475 Å, while the planar **4** adopts D_{10h} symmetry and therefore has 10 exactly equivalent C–C bonds of 1.404 Å. The species **3** and **4** are first- and second-order saddle points, respectively. They connect two equivalent equilibrium structures **3'** and four equivalent equilibrium structures **4'**, respectively. Note also that C–C bonds in the planar **3** and **4** are always somewhat longer than the corresponding C–C bonds in the nonplanar **3'** and **4'**. We come back to this later on in the discussion.

In the following, we analyze and compare the structure and bonding of **1**, **2**, **3** and **4**. The fact that all these species are planar enables us to consistently separate and study the bonding in the σ - and π -electron systems and how they change along the series of 4-, 6-, 8- and 10-membered conjugated hydrocarbon rings. Later on, we will address the question why cyclooctatetraene and cyclodecapentaene eventually undergo bending and adopt nonplanar equilibrium geometries.

To understand why **1** and **3** undergo localization whereas **2** and **4** oppose localization, we have examined the energy and bonding of these species along a distortion mode proceeding from a regular delocalized structure with all C–C bonds equivalent towards a geometry with alternating single and double bonds. A key step in our approach is that this can be done by rotating two equivalent and geometrically frozen fragments relative to each other, as shown in Scheme 7.1. Such an approach was already presented for **1** and **2** in Ref. [3] and is extended here to **3** and **4**. The advantage is that this greatly reduces the complexity of the bond analysis because we go from a multi-fragment to a two-fragment problem. Thus, for cyclobutadiene, we go from a D_{4h} symmetric species with all C–C bonds at 1.465 Å to the D_{2h} symmetric **1**

with alternating C–C bonds of 1.338 and 1.581 Å. In the case of benzene, we go from D_{6h} symmetric **1** with all C–C bonds at 1.398 Å to a D_{3h} symmetric structure with alternating C–C bonds of 1.291 and 1.502 Å. Likewise, for cyclooctatetraene, we go from a D_{8h} symmetric species with all C–C bonds at 1.408 Å to the D_{4h} symmetric **3** with alternating C–C bonds of 1.350 and 1.475 Å (i.e., the optimum geometry under the constraint of planarity). And, finally, in the case of cyclodecapentaene, we go from D_{10h} symmetric **4** with all C–C bonds at 1.404 Å (which is the optimum geometry under the constraint of planarity) to a D_{5h} symmetric structure with alternating C–C bonds of 1.328 and 1.479 Å. Note that along this distortion of cyclobutadiene and cyclooctatetraene, we preserve the singlet electron configuration of the equilibrium structure **1** and **3**, as we wish to understand the behavior of the latter (the D_{4h} and D_{8h} arrangements for **1** and **3** have triplet ground states at 5.19 and 2.33 kcal/mol above **1** and **3**, respectively, with C–C bonds of 1.444 and 1.408 Å).

Scheme 7.1 Construction and distortion of **1**, **2**, **3** and **4** in terms of two rigid fragments.



We wish to point out that, although physically quite plausible, our choice of deformation modes, in particular the nonequilibrium localized benzene and cyclodecapentaene as well as the delocalized cyclobutadiene and cyclooctatetraene geometries, are not unique. However, we have already previously verified for cyclobutadiene and benzene that all trends and conclusions that play a role in the following discussion are not affected if other plausible choices are made.^[3]

In our approach, the change in energy ΔE that goes with localizing our model systems is equal to the change in interaction energy ΔE_{int} between two geometrically frozen $(\text{CH})_2^{6\bullet}$, $(\text{CH})_3^{9\bullet}$, $(\text{CH})_4^{12\bullet}$ and $(\text{CH})_5^{15\bullet}$ fragments in their septet, decet, tredecet and sexdecet valence configuration for **1**, **2**, **3** and **4**, respectively. The preparation energy ΔE_{prep} vanishes in this analysis because it is constant for geometrically frozen fragments. Each pair of fragments has mutually opposite spins (superscripts α and β in Scheme 7.1) to allow for the formation of all σ and π electron-pair bonds. These fragments are weakly (compared to the bonding interactions in **1**, **2**, **3** and **4**) repulsive conglomerates of two, three, four and five $\text{CH}^{\bullet\bullet\bullet}$ radicals, respectively. The changes in interaction can be analyzed within the conceptual framework of the MO model contained in Kohn-Sham DFT by decomposing ΔE_{int} into classical electrostatic attraction (ΔV_{elstat}), Pauli repulsive orbital interactions between same-spin electrons (ΔE_{Pauli}) and the (mainly electron-pair) bonding orbital interactions (ΔE_{oi}).^[13] As pointed out in the methodological section, the latter can be symmetry decomposed into contributions from the σ and π orbital interactions: $\Delta E_{\text{oi}} = \Delta E_{\sigma} + \Delta E_{\pi}$.^[13] Thus, we have

$$\Delta E_{\text{int}} = \Delta E_{\text{Pauli}} + \Delta E_{\sigma} + \Delta E_{\pi} + \Delta V_{\text{elstat}} \quad (7.4)$$

And because in our construction of **1**, **2**, **3** and **4** the π electrons contribute no Pauli repulsion (*vide infra*), we can write

$$\Delta E_{\text{int}} = \text{"total } \sigma\text{"} + \text{"total } \pi\text{"} + \Delta V_{\text{elstat}}, \quad (7.5)$$

with "total σ " = $\Delta E_{\text{Pauli}} + \Delta E_{\sigma}$ and "total π " = ΔE_{π} .

The results of our analyses, in Figure 7.1, show that not only in **1** and **2** (as shown previously)^[3] but also in **3** and **4**, it is the π electrons that determine if an aromatic, delocalized geometry occurs or an antiaromatic one with localized double bonds. In the first place, not unexpectedly, *localization* of the *delocalized* D_{4h} and D_{8h} symmetric arrangements of cyclobutadiene and cyclooctatetraene towards the corresponding D_{2h} and D_{4h} symmetric structures **1** and **3** goes with a stabilization whereas the energy of D_{6h} and D_{10h} symmetric benzene (**2**) and cyclodecapentaene (**4**) rises on localization (black bold curves in Figures 7.1a-d). Now it appears that the σ -electron system always opposes to this localization whereas the π -electron system always promotes the very same localization of double bonds (compare blue "total σ " with red "total π " curves in Figures 7.1a-d).

There is a marked difference between the localizing force that the respective π -electron systems exert on the ring geometry in **1** and **3** as compared to **2** and **4**. In the antiaromatic ring systems **1** and **3**, the propensity of the π system to localize the double bonds is dramatically increased as compared to the aromatic rings **2** and **4** (compare red "total π " curve in Figures 7.1a and 7.1c with those in Figures 7.1b and 7.1d). The classical electrostatic attraction ΔV_{elstat} , which slightly favors localization, differs much less along **1 - 4**.

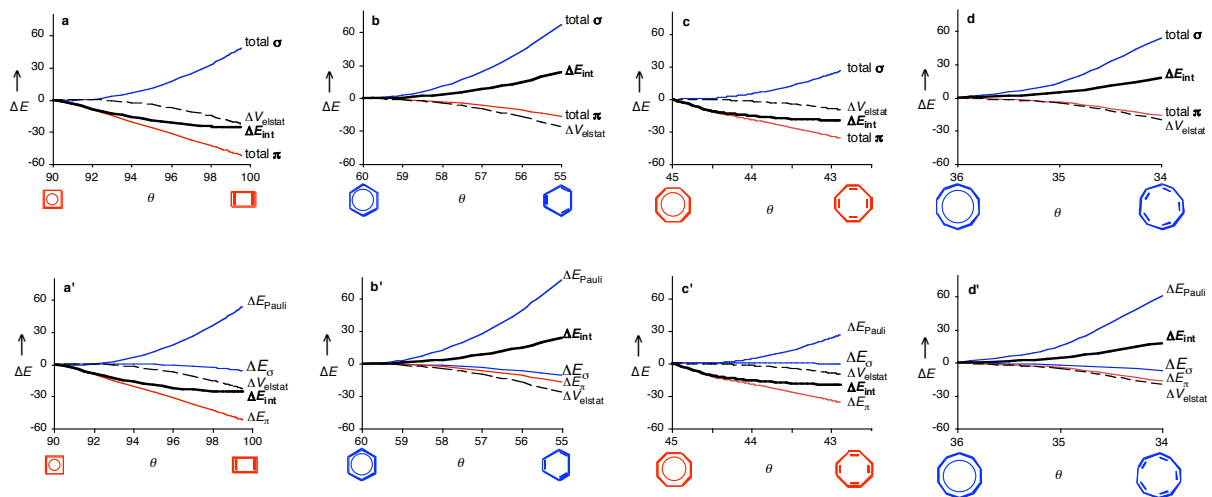


Figure 7.1 Bond energy decomposition (in kcal/mol) of **1**, **2**, **3** and **4**, each constructed from two equivalent rigid fragments, as function of the distortion mode (in deg) from delocalized to localized structure as defined in Scheme 7.1 computed at BP86/TZ2P.

$$\Delta E_{\text{int}} = (\Delta E_{\text{Pauli}} + \Delta E_{\sigma}) + [\Delta E_{\pi}] + \Delta V_{\text{elstat}} = (\text{total } \sigma) + [\text{total } \pi] + \Delta V_{\text{elstat}}$$

How can we understand the above? The σ bonds are characterized by an equilibrium distance greater than zero, roughly 1.5 Å for C–C bonds. One reason for this is the early onset of $\langle 2p_\sigma | 2p_\sigma' \rangle$ compared to $\langle 2p_\pi | 2p_\pi' \rangle$ overlap and the fact that the former achieves an optimum at distances greater than zero whereas the latter is maximal at distance zero (see also Ref. [15]). This is illustrated in Figure 7.2 for two C–H^{'''} fragments in benzene approaching each other on localization (see black curves). However, as pointed out before in a different context,^[16] the main reason for σ bonds to feature an optimum distance greater than zero is the repulsive wall provided by Pauli repulsion with the closed shell 2s (and 1s) AOs on carbon and the C–H bonds. In the symmetric, delocalized structures, each C–C bond is already forced by partial π bonding below the optimum σ distance, i.e., it is already in the region where the Pauli repulsion ΔE_{Pauli} due to the σ electrons goes up in energy faster than the stabilizing orbital interactions ΔE_{σ} and ΔV_{elstat} together go down. This becomes clear if one separates "total σ ", shown in Figures 7.1a-d, into its component $\Delta E_{\text{Pauli}} + \Delta E_{\sigma}$ as has been done in Figures 7.1a'-d'.

The π electron systems, on the other hand, only provide electron-pair bonding and *no* Pauli repulsive orbital interactions, as can be seen for **3** and **4** in Figure 7.3 (for **1** and **2**, see the Figure 6.4 in Chapter 6). They achieve an optimum overlap at zero bond distance (see Figure 7.2). But why is the localizing propensity of the π system in **1** and **3** so prominent whereas it is so little pronounced in **2** and **4**? Essential for understanding this difference is the qualitatively different topology and geometry dependence of the π overlaps in the aromatic or antiaromatic "many π -electron" systems as compared to a simple 2 π -electron system which is

represented by the black $\langle 2p_{\pi}|2p_{\pi} \rangle$ curve in Figure 7.2. Scheme 7.2 extracts from Figures 6.4 and 7.3 the key features that emerge from our quantitative Kohn-Sham MO analyses.

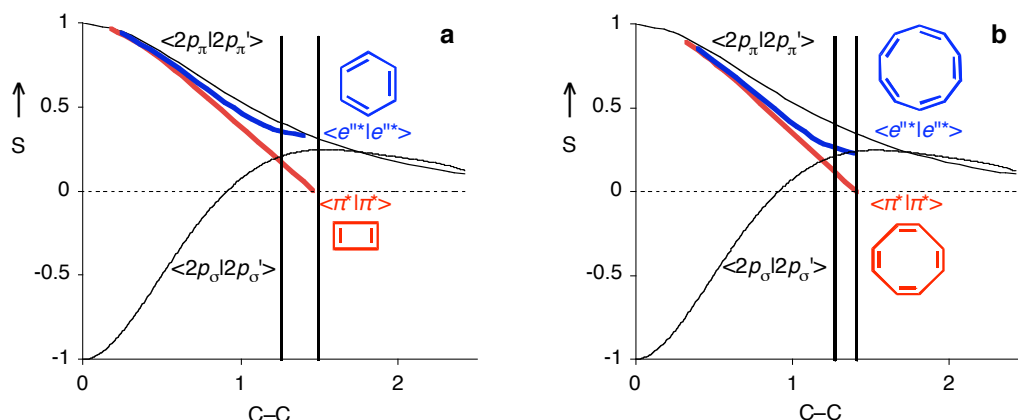


Figure 7.2 Selected overlap integrals between MOs of two CH''' units in **2** (black curves in a, b), between MOs of two $(\text{CH})_2^{6*}$ units in **1** (red curve in a), between two $(\text{CH})_3^{9*}$ units in **2** (blue curve in a), between MOs of two $(\text{CH})_4^{12*}$ units in **3** (red curve in b), and between two $(\text{CH})_5^{15*}$ units in **4** (blue curve in b) as function of the C–C distance (in Å) along the localization distortion defined in Scheme 7.1. The localization intervals for **1** and **2**, **3** and **4** are indicated by vertical lines.

The main difference between π overlap in **1** - **4** versus that between two simple CH''' fragments is the occurrence of amplifying effects, on localization, in the antiaromatic **1** and **3**, and counteracting effects in the aromatic **2** and **4**. Whereas the $\langle 2p_{\pi}|2p_{\pi} \rangle$ overlap between two CH''' fragments smoothly increases from 0 (at $\text{C}-\text{C} = \infty$) towards the value 1 (at $\text{C}-\text{C} = 0$), the π bonding a'' MOs in **1**, **2**, **3** and **4** gain and lose bonding overlap in the shrinking and expanding C–C bonds, respectively (see Scheme 7.2; see also Figure 7.3 as well as Figure 6.4). The net effect is still a gain in bonding but in essence this is not so pronounced anymore (see Figure 7.2). Similar arguments hold for the π bonding set of degenerate e'' MOs in **2** and **4**. This is shown in Scheme 7.2 in which stabilizing and destabilizing effects are indicated for one of these e'' MOs with + and – signs, respectively (see Figure 7.3 for more details of the bonding). This makes the π systems of the aromatic ring systems **2** and **4** comparatively indifferent with respect to localizing the double C–C bonds.

A completely different situation holds for the nonbonding degenerate e''_{NB} MOs in the second-order Jahn-Teller unstable D_{4h} - and D_{8h} -symmetric geometries of cyclobutadiene and cyclooctatetraene.^[15] One of these π MOs in either of the antiaromatic rings gains, on localization, stabilization in every C–C bond (this is indicated with the + signs in Scheme 7.2). And it does so rapidly. This is because the orbital overlap starts to build up from 0 (i.e., no overlap and no stabilization) at a finite C–C distance of 1.465 Å (**1**) or 1.408 Å (**3**) and rises to the value 1 as the C–C distance decreases to 0 (see Figure 7.2). This differs from the distance dependence of the π overlap between two $2p_{\pi}$ AOs on two simple CH''' fragments (or on two carbon atoms) which has its zero point at a C–C distance of ∞ but also goes to 1 as the

C–C distance decreases to 0 Å (see $\langle 2p_{\pi}|2p_{\pi}\rangle$ in Figure 7.2). Along the bond localizing distortion, the gain in overlap in **1** between the two π^* $(\text{CH})_2^{6*}$ fragment MOs (shown in Figure 6.4) is a sizeable 0.102! (see Figure 7.2a). Likewise, although somewhat less pronounced, the gain in overlap in **3** between the two π^* $(\text{CH})_4^{12*}$ fragment MOs amounts to 0.051 (see Figure 7.2b). This has to be compared with a much smaller gain in overlap of only 0.012 and 0.020, respectively, between the two e''^* $(\text{CH})_3^{9*}$ fragment MOs in **2** and the two e'' $(\text{CH})_5^{15*}$ fragment MOs in **4** that form the π bonding e'' HOMOs of the two aromatic rings. Consequently, the aforementioned e''_{NB} MO of cyclobutadiene and that of cyclooctatetraene, which are fully occupied in the singlet ground state of **1** and **3**, drop markedly in energy along the localization mode. This causes the enhanced propensity of the π electron system in cyclobutadiene and cyclooctatetraene towards localization of the double C–C bonds.

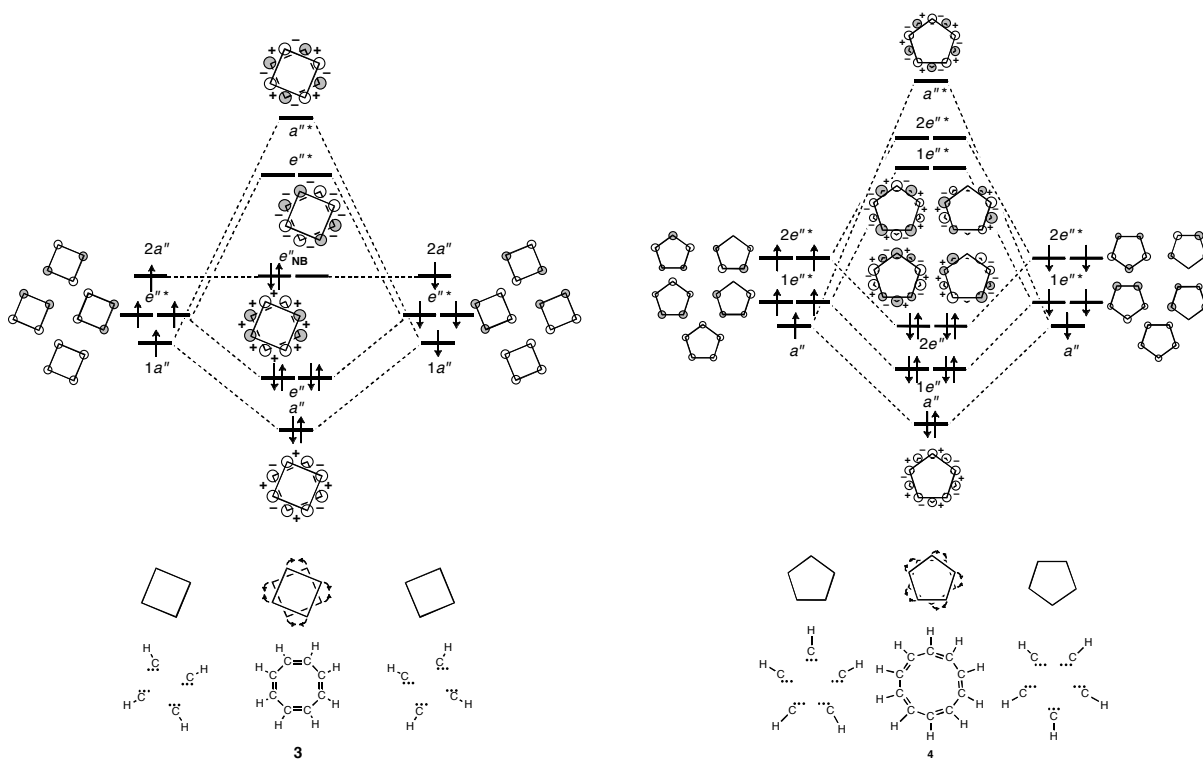
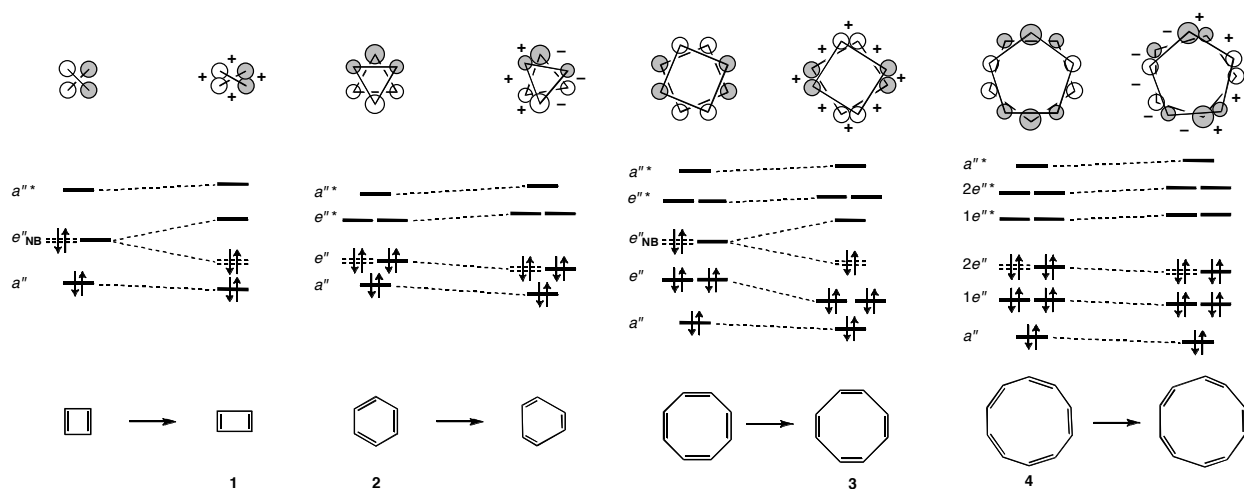


Figure 7.3 Schematic π MO interaction diagram of cyclooctatetraene (**3**, left panel) constructed from two $(\text{CH})_4^{12*}$ fragments in their tredecet valence configuration, and of cyclodecapentaene (**4**, right panel) constructed from two $(\text{CH})_5^{15*}$ fragments in their sexdecet valence configuration based on Kohn-Sham MO analyses at BP86/TZ2P. There are respectively 4 and 5 π electrons in each of the two fragments, which have mutually opposite spin. The effect on orbital energies of the localization mode defined in Scheme 7.1 and represented here with curved arrows is indicated by + (stabilization) and – (destabilization).

Finally, we come back to the question why cyclooctatetraene and cyclodecapentaene eventually undergo bending and adopt nonplanar equilibrium geometries **3'** and **4'**. This

phenomenon can be ascribed to the increased steric repulsion between hydrogens of *vicinal* C–H bonds, very similar to the mechanism that causes ethane to avoid the eclipsed C–H bonds and to adopt a staggered conformation.^[16a,c] Thus, along the series **1**, **2**, **3** and **4**, the longest *vicinal* H–H distance in each of these *planar* species decreases monotonically from 3.115 to 2.488 to 2.271 to 2.080 Å because the C–C–H angle systematically decreases, for simple goniometric reasons, as the size of the carbon ring becomes larger.^[17] The increasing H–H steric repulsion can be relieved in **3** through facile internal rotation of C–H bonds around C–C single bonds ($H-C-C-H = 42.6^\circ$) but not around the localized C–C double bonds ($H-C-C-H = 0^\circ$), yielding the tub-shaped **3'**. Likewise, the further increasing H–H steric repulsion in **4** can again be reduced through internal rotation of C–H bonds around C–C bonds. But at variance with **3**, the C–C bonds all have partial double bond character yielding the saddle-shaped **4'** in which the bending is spread over more –CH–CH– moieties with smaller dihedral angles (two times 14.4° , 12.8° , -6.3° , -17.1° , -3.9°). Note that the diminished H–H repulsion in the nonplanar **3'** and **4'** also translates into the slight contraction of C–C bonds (as compared to planar **3** and **4**, respectively) mentioned in the beginning of the discussion.

Scheme 7.2 Effect of localization on π MO levels of **1**, **2**, **3** and **4**.
Orbital plots at top refer to dashed levels.



7.4 Conclusions

The MO model of (anti)aromaticity that we recently developed^[3] for cyclobutadiene (**1**) and benzene (**2**) extends also to the corresponding next larger analogs, cyclooctatetraene (**3'**) and cyclodecapentaene (**4'**), respectively. Our MO model accounts for the antiaromaticity of **3'** and the only very weakly aromatic nature of **4'**.

Thus, in none of the cases does the π -electron system favor a symmetric, delocalized ring. The regular, symmetric structure of benzene has the same cause as that of cyclohexane,^[3] namely, the σ -electron system. Nevertheless, the π system decides if

delocalization occurs by showing qualitatively different geometry-dependence of the π overlap in the aromatic (**2** and **4'**) versus the antiaromatic rings (**1** and **3'**). In the latter two, all π -overlap effects unidirectionally favor localization of the double bonds and can, in this way, overrule the σ system. The somewhat more pronounced steric repulsion between vicinal C–H bonds in planar **3** causes cyclooctatetraene to adopt the nonplanar, tub-shaped equilibrium conformation **3'** in which this steric repulsion is reduced around C–C single bonds.

In the aromatic species, the localizing propensity of the π system emerges from a subtle interplay of counteracting overlap effects. In benzene (**2**), it is therefore too little pronounced to overcome the delocalizing σ system. In cyclodecapentaene, the π system shows a somewhat increased localizing propensity but, in our BP86 calculations, this is still not strong enough to overcome the delocalizing σ system. Therefore, we arrive at a delocalized structure which, however, adopts a nonplanar, saddle-shaped conformation **4'** to minimized the steric repulsion between vicinal C–H bonds. Note that while our delocalized structure of **4'** differs from the MP2 geometry (with localized double bonds) found by Allen and Schaefer,^[11] our electronic structure analyses nicely confirm that the π -electron system of **4'** causes the aromatic character of this species to be much reduced if compared to **2**.

References

- [1] (a) P. J. Garratt, *Aromaticity*, John Wiley & Sons, Inc, New York, **1986**; (b) V. I. Minkin, M. N. Glukhotsev, B. Y. Simkin, *Aromaticity and Antiaromaticity: Electronic and Structural Aspects*, John Wiley & Sons, Inc, New York, **1994**.
- [2] (a) R. Breslow, *Acc. Chem. Res.* **1973**, *6*, 393; (b) T. M. Krygowski, M. K. Cyranski, Z. Czarnocki, G. Hafelinger, A. R. Katritzky, *Tetrahedron* **2000**, *56*, 1783; (c) P. v. R. Schleyer, H. J. Jiao, *Pure Appl. Chem.* **1996**, *68*, 209; (d) Special issue on: *Aromaticity*, ed. P. v. R. Schleyer, *Chem. Rev.* **2001**, *101*; (e) M. K. Cyranski, T. M. Krygowski, A. R. Katritzky, P. v. R. Schleyer, *J. Org. Chem.* **2002**, *67*, 1333; (f) Special issue on: *Delocalization – pi and sigma*, ed. J. A. Gladysz, *Chem. Rev.* **2005**, *105*. (g) D. Moran, A. C. Simmonett, F. E. Leach III, W. D. Allen, P. v. R. Schleyer, H. F. Schaefer III, *J. Am. Chem. Soc.* **2006**, *128*, 9342.
- [3] S. C. A. H. Pierrefixe, F. M. Bickelhaupt, *Chem. Eur. J.* **2007**, *13*, 6321.
- [4] E. Hückel, *Z. Phys.* **1931**, *70*, 204.
- [5] (a) M. B. Smith, J. March, *March's Advanced Organic Chemistry*, 6th ed., Wiley-Interscience: New York, **2007**; (b) F. A. Carey, R. J. Sundberg, *Advanced Organic Chemistry: Structure And Mechanisms (Part A)*, Springer, New York, **2000**.
- [6] (a) Y. Ooshika, *J. Phys. Soc. Japan* **1957**, *12*, 1238; (b) H. Labhart, *J. Chem. Phys.* **1957**, *27*, 947; (c) H. C. Longuet-Higgins, L. Salem, *Proc. R. Soc. London, A* **1959**, *251*, 172; (d) M. Tsui, S. Huzinaga, T. Hasino, *T. Rev. Mod. Phys.* **1960**, *32*, 425; (e) R. S. Berry, *J. Chem. Phys.* **1961**, *35*, 2253.
- [7] (a) Y. Haas, S. Zilberg, *J. Am. Chem. Soc.* **1995**, *117*, 5387; (b) E. Heilbronner, *J. Chem. Educ.* **1989**, *66*, 471; (c) A. Stanger, K. P. C. Vollhardt, *J. Org. Chem.* **1988**, *53*, 4889; (d) N. D. Epotis, *Pure Appl. Chem.* **1983**, *55*, 229.
- [8] (a) P. C. Hiberty, S. S. Shaik, J. M. Lefour, G. Ohanessian, *J. Org. Chem.* **1985**, *50*, 4657; (b) S. S. Shaik, P. C. Hiberty, *J. Am. Chem. Soc.* **1985**, *107*, 3089; (c) P. C. Hiberty, S. S. Shaik, G. Ohanessian, J. M. Lefour, *J. Org. Chem.* **1986**, *51*, 3908; (d) S. S. Shaik, P. C. Hiberty, J. M.

- Lefour, G. Ohanessian, *J. Am. Chem. Soc.* **1987**, *109*, 363; (e) S. S. Shaik, P. C. Hiberty, G. Ohanessian, J. M. Lefour, *J. Phys. Chem.* **1988**, *92*, 5086; (f) P. C. Hiberty, D. Danovich, A. Shurki, A.; Shaik, S. *J. Am. Chem. Soc.* **1995**, *117*, 7760; (g) A. Shurki, S. Shaik, *Angew. Chem. Int. Ed. Engl.* **1997**, *36*, 2205; (h) S. Shaik, A. Shurki, D. Danovich, P. C. Hiberty, *Chem. Rev.* **2001**, *101*, 1501.
- [9] (a) N. C. Baird, *J. Org. Chem.* **1986**, *51*, 3907; (b) E. D. Glendening, R. Faust, A. Streitwieser, K. P. C. Vollhardt, F. Weinhold, *J. Am. Chem. Soc.* **1993**, *115*, 10952.
- [10] (a) K. Jug, A. M. Koster, *J. Am. Chem. Soc.* **1990**, *112*, 6772; (b) A. Gobbi, Y. Yamaguchi, G. Frenking, H. F. Schaefer III, *Chem. Phys. Lett.* **1995**, *244*, 27; (c) B. Kovacevic, D. Baric, Z. B. Maksic, T. Müller, *ChemPhysChem* **2004**, *5*, 1352; (d) A. Rehaman, A. Datta, S. S. Mallajosyula, S. K. Pati, *J. Chem. Theory Comput.* **2006**, *2*, 30.
- [11] (a) P. B. Karadakov, J. Gerratt, D. L. Cooper, M. Raimondi, *J. Phys. Chem.* **1995**, *99*, 10186; (b) R. A. King, T. D. Crawford, J. F. Stanton, H. F. Schaefer III, *J. Am. Chem. Soc.* **1999**, *121*, 10788.
- [12] (a) G. te Velde, F. M. Bickelhaupt, E. J. Baerends, C. Fonseca Guerra, S. J. A. van Gisbergen, J. G. Snijders, T. Ziegler, *J. Comput. Chem.* **2001**, *22*, 931; (b) C. Fonseca Guerra, O. Visser, J. G. Snijders, G. te Velde, E. J. Baerends, in *Methods and Techniques for Computational Chemistry*, (Eds.: E. Clementi, G. Corongiu), STEF: Cagliari, **1995**, p. 305-395; (c) E. J. Baerends, D. E. Ellis, P. Ros, *Chem. Phys.* **1973**, *2*, 41; (d) E. J. Baerends, P. Ros, *Chem. Phys.* **1975**, *8*, 412; (e) E. J. Baerends, P. Ros, *Int. J. Quantum. Chem. Symp.* **1978**, *12*, 169; (f) C. Fonseca Guerra, J. G. Snijders, G. te Velde, E. J. Baerends, *Theor. Chem. Acc.* **1998**, *99*, 391; (g) P. M. Boerrigter, G. te Velde, E. J. Baerends, *Int. J. Quantum Chem.* **1988**, *33*, 87; (h) G. te Velde, E. J. Baerends, *J. Comp. Phys.* **1992**, *99*, 84; (i) J. G. Snijders, E. J. Baerends, P. Vernooij, *At. Nucl. Data Tables* **1982**, *26*, 483; (j) J. Krijn, E. J. Baerends, *Fit-Functions in the HFS-Method; Internal Report (in Dutch)*, Vrije Universiteit, Amsterdam, **1984**; (k) L. Versluis, T. Ziegler, *J. Chem. Phys.* **1988**, *88*, 322; (l) J. C. Slater, *Quantum Theory of Molecules and Solids*, Vol. 4, McGraw-Hill, New York, **1974**; (m) A. D. Becke, *J. Chem. Phys.* **1986**, *84*, 4524; (n) A. Becke, *Phys. Rev. A* **1988**, *38*, 3098; (o) S. H. Vosko, L. Wilk, M. Nusair, *Can. J. Phys.* **1980**, *58*, 1200; (p) J. P. Perdew, *Phys. Rev. B* **1986**, *33*, 8822 (Erratum: *Phys. Rev. B* **1986**, *34*, 7406); (q) L. Fan, T. Ziegler, *J. Chem. Phys.* **1991**, *94*, 6057.
- [13] (a) F. M. Bickelhaupt, E. J. Baerends, in *Review in Computational Chemistry* Vol. 15, **2000**, pp. 1; (b) F. M. Bickelhaupt, N. M. M. Nibbering, E. M. van Wezenbeek, E. J. Baerends, *J. Phys. Chem.* **1992**, *96*, 4864; (c) F. M. Bickelhaupt, A. Diefenbach, S. P. de Visser, L. J. de Koning, N. M. M. Nibbering, *J. Phys. Chem. A* **1998**, *102*, 9549; (d) T. Ziegler, A. Rauk, *Inorg. Chem.* **1979**, *18*, 1755; (e) T. Ziegler, A. Rauk, *Inorg. Chem.* **1979**, *18*, 1558; (f) T. Ziegler, A. Rauk, *Theor. Chim. Acta* **1977**, *46*, 1.
- [14] K. Morokuma, *Acc. Chem. Res.* **1977**, *10*, 294.
- [15] T. A. Albright, J. K. Burdett, M.-H. Whangbo, *Orbital Interactions in Chemistry*, John Wiley & Sons Inc, New-York, **1985**.
- [16] (a) F. M. Bickelhaupt, E. J. Baerends, *Angew. Chem.* **2003**, *115*, 4315; *Angew. Chem. Int. Ed.* **2003**, *42*, 4183; (b) F. M. Bickelhaupt, R. L. DeKock, E. J. Baerends, *J. Am. Chem. Soc.* **2002**, *124*, 1500; See also (c) Y. Mo, J. Gai, *Acc. Chem. Res.* **2007**, *40*, 113.
- [17] This C–C–H angle is 150° for D_{3h} symmetric C_3H_3 and approaches to the limiting value of 90° if $n \rightarrow \infty$ for D_{nh} symmetric C_nH_n .

8 Aromaticity in Heterocyclic and Inorganic Benzene Analogs

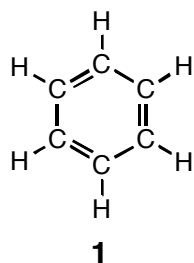
Adapted from S. C. A. H. Pierrefixe and F. M. Bickelhaupt
Aust. J. Chem. **2008**, *61*, 209

Abstract

Recently, we presented an MO model of aromaticity that explains, in terms of simple orbital-overlap arguments, *why* benzene (C_6H_6) has a regular structure with delocalized double bonds. Here, we show that the same model and the same type of orbital-overlap arguments also account for heterocyclic and inorganic benzene analogs, such as, *s*-triazine ($C_3N_3H_3$), hexazine (N_6), borazine ($B_3N_3H_6$), boroxine ($B_3O_3H_3$), hexasilabenzene (Si_6H_6) and hexaphosphabenzene (P_6). Our MO model is based on accurate Kohn-Sham DFT analyses of the bonding in the seven model systems, and how the bonding mechanism is affected if these molecules undergo geometrical deformations between regular, delocalized ring structures and distorted ones with localized double bonds. It turns out that also in the heterocyclic and inorganic benzene analogs, the propensity of the π electrons is always to *localize* the double bonds, against the delocalizing force of the σ electrons. The latter, in general prevails, yielding the regular, delocalized ring structures. Interestingly, we find one exception to this rule: N_6 .

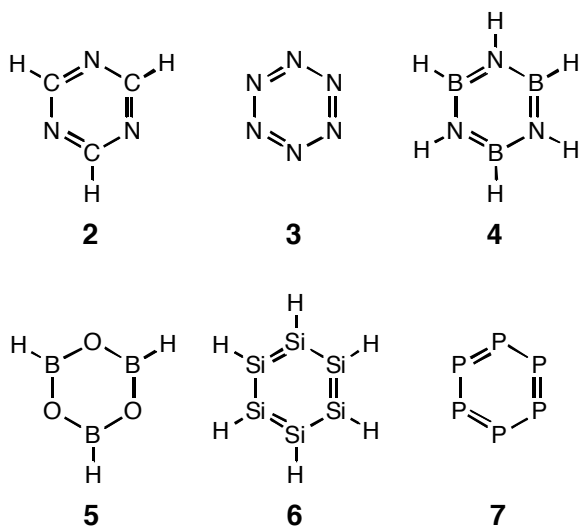
8.1 Introduction

Aromatic compounds as well as the concept of aromaticity itself have been the subject in many experimental and theoretical studies.^[1-9] The key characteristics of organic aromatic compounds are: (i) a regular, delocalized structure involving C–C bonds of equal length, each with partial double-bond character, (ii) enhanced thermodynamic stability, and (iii) reduced reactivity as compared to nonaromatic conjugated hydrocarbons.^[1,2] After the early theoretical investigations of Hückel, the regular symmetric geometry of benzene (**1**) and other aromatic molecules has been attributed to a delocalizing tendency of the π -electron system.^[2-4]



Recently, in a quantitative Kohn-Sham molecular orbital (MO) study, we addressed the question *why* aromatic benzene rings (**1**) have a regular structure with delocalized double bonds.^[5] Our MO model showed that the π electron system never favors a symmetric, delocalized ring, neither in antiaromatic rings, such as 1,3-cyclobutadiene, nor in **1**. The regular, symmetric structure of **1** appears to have the same cause as that of planar cyclohexane, namely, the σ electron system. And yet, it is the π system which decides if delocalization occurs or not.^[5] The mechanism behind this control is a qualitatively different geometry-dependence of the π overlap in **1** and cyclobutadiene. In the aromatic species **1**, the localizing propensity of the π system emerges from a subtle interplay of counteracting overlap effects and is therefore too little pronounced to overcome the delocalizing σ system. At variance, in the antiaromatic cyclobutadiene ring, all π overlap effects unidirectionally favor localization of the double bonds and can, in this way, overrule the σ system. This nicely augments and agrees with earlier work by Shaik, Hiberty^[6] and other pioneers in the field.^[7,8]

Herein, we wish to further explore if our MO model developed for the archetypal, organic benzene (**1**) is also valid for *heterocyclic* and *inorganic* benzene analogs that are isoelectronic to **1**. As representative examples of such compounds, we have chosen *s*-triazine (**2**), hexazine (**3'**), borazine (**4**), boroxine (**5**), hexasilabenzene (**6'**) and hexaphosphabenzene (**7'**). Note that **3'**, **6'** and **7'** have nonplanar equilibrium geometries.^[10] To facilitate a direct comparison and to enable us to separate σ and π electron bonding consistently in all model systems, we have included the planar species **3**, **6** and **7** into our set of model systems. Thus, we have quantum chemically investigated the structure and bonding of **1** - **7**, **3'**, **6'** and **7'** at the BP86/TZ2P level of density functional theory (DFT) using the ADF program.^[11]



Our analyses show that the MO model developed previously for **1** is indeed also valid for **2 - 7**. The π -electron system is confirmed to have in all cases a propensity to *localize* double bonds, against the delocalizing force of the σ -electron system. Simple orbital-overlap arguments account for this behavior. Interestingly, while the delocalizing force of the σ electron system prevails in most cases, this is not the case for planar hexazine (**3**). The latter species is in its D_{6h} symmetric geometry very weakly labile (nearly "undecided") towards localization. However, this localization mode eventually proceeds without barrier towards the formation of 3 nitrogen molecules.

8.2 Theoretical Methods

8.2.1 General Procedure

All calculations were performed using the Amsterdam Density Functional (ADF) program developed by Baerends and others.^[11] The numerical integration was performed using the procedure developed by te Velde et al..^[11g,h] The MOs were expanded in a large uncontracted set of Slater type orbitals (STOs) containing diffuse functions: TZ2P (no Gaussian functions are involved).^[11i] The basis set is of triple- ζ quality for all atoms and has been augmented with two sets of polarization functions, i.e. 3d and 4f on B, C, N, O, Si and P, and 2p and 3d on H. The 1s core shell of B, C, N and O and the 1s2s2p core shell of Si and P were treated by the frozen-core approximation.^[11c] An auxiliary set of s, p, d, f and g STOs was used to fit the molecular density and to represent the Coulomb and exchange potentials accurately in each self-consistent field cycle.^[11j]

Equilibrium structures were optimized using analytical gradient techniques.^[11k] Geometries and energies were calculated at the BP86 level of the generalized gradient approximation (GGA): exchange is described by Slater's X α potential^[11l] with corrections due to Becke^[11m,n] added self-consistently and correlation is treated in the Vosko-Wilk-Nusair (VWN) parameterization^[11o] with nonlocal corrections due to Perdew^[11p] added, again, self-

consistently (BP86).^[11q] All stationary points were confirmed to be equilibrium structures (number of imaginary frequencies: NIMAG = 0), transition states (NIMAG = 1) or higher-order saddle points (NIMAG > 1) through vibrational analyses.

8.2.2 Bonding Energy Analysis

To obtain more insight into the nature of the bonding in our cyclic systems, an energy decomposition analysis has been carried out.^[12] In this analysis, the total binding energy ΔE associated with forming the overall molecular species of interest, say AB, from two (or sometimes more) radical fragments, A' + B', is made up of two major components (Eq. 8.1):

$$\Delta E = \Delta E_{\text{prep}} + \Delta E_{\text{int}} \quad (8.1)$$

In this formula, the preparation energy ΔE_{prep} is the amount of energy required to deform the individual (isolated) radical fragments from their equilibrium structure (A', B') to the geometry that they acquire in the overall molecule (A, B). The interaction energy ΔE_{int} corresponds to the actual energy change when these geometrically deformed fragments A and B are combined to form the combined molecular species AB. It is analyzed in the framework of the Kohn-Sham Molecular Orbital (MO) model using a quantitative decomposition of the bond into electrostatic interaction, Pauli repulsion (or exchange repulsion or overlap repulsion), and (attractive) orbital interactions (Eq. 8.2).^[12]

$$\Delta E_{\text{int}} = \Delta V_{\text{elstat}} + \Delta E_{\text{Pauli}} + \Delta E_{\text{oi}} \quad (8.2)$$

The term ΔV_{elstat} corresponds to the classical electrostatic interaction between the unperturbed charge distributions $\rho_A(r) + \rho_B(r)$ of the prepared or deformed radical fragments A and B (*vide infra* for definition of the fragments) that adopt their positions in the overall molecule AB, and is usually attractive. The Pauli repulsion term, ΔE_{Pauli} , comprises the destabilizing interactions between occupied orbitals and is responsible for the steric repulsion. This repulsion is caused by the fact that two electrons with the same spin cannot occupy the same region in space. It arises as the energy change associated with the transition from the superposition of the unperturbed electron densities $\rho_A(r) + \rho_B(r)$ of the geometrically deformed but isolated radical fragments A and B to the wavefunction $\Psi^0 = N \hat{A} [\Psi_A \Psi_B]$, that properly obeys the Pauli principle through explicit antisymmetrization (\hat{A} operator) and renormalization (N constant) of the product of fragment wavefunctions (see Ref. [13a] for an exhaustive discussion). The orbital interaction ΔE_{oi} in any MO model, and therefore also in Kohn-Sham theory, accounts for electron-pair bonding,^[12a,b] charge transfer (i.e., donor–acceptor interactions between occupied orbitals on one moiety with unoccupied orbitals of the other, including the HOMO–LUMO interactions) and polarization (empty–occupied orbital mixing on one fragment due to the presence of another fragment). In

the bond-energy decomposition, open-shell fragments are treated with the spin-unrestricted formalism but, for technical (not fundamental) reasons, spin-polarization is not included. This error causes an electron-pair bond to become in the order of a few kcal/mol too strong. To facilitate a straightforward comparison, the results of the energy decomposition were scaled to match exactly the regular bond energies. Since the Kohn-Sham MO method of density-functional theory (DFT) in principle yields exact energies and, in practice, with the available density functionals for exchange and correlation, rather accurate energies, we have the special situation that a seemingly one-particle model (an MO method) in principle completely accounts for the bonding energy.^[12a]

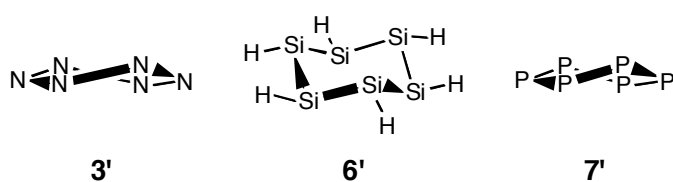
The orbital interaction energy can be decomposed into the contributions from each irreducible representation Γ of the interacting system (Eq. 8.3) using the extended transition state (ETS) scheme developed by Ziegler and Rauk^[12c-e] (note that our approach differs in this respect from the Morokuma scheme,^[13] which instead attempts a decomposition of the orbital interactions into polarization and charge transfer):

$$\Delta E_{\text{oi}} = \sum_{\Gamma} \Delta E_{\Gamma} = \Delta E_{\sigma} + \Delta E_{\pi} \quad (8.3)$$

In our model systems, the irreducible representations can be categorized into symmetric and antisymmetric with respect to the mirror plane provided by the carbon-atom framework, which correspond to what is commonly designated σ and π electron systems, respectively. This gives rise to the orbital-interaction components ΔE_{σ} and ΔE_{π} , as shown in Eq. 8.3 above.

8.3 Results and Discussions

In line with previous studies, we find that benzene and all benzene analogs, except hexazine (**3'**), possess equilibrium geometries with six equivalent element–element bonds in the ring. Four of these species are furthermore planar: benzene (**1**), *s*-triazine (**2**), borazine (**4**) and boroxine (**5**). Hexazine (**3'**) and hexaphosphabenzene (**7'**), on the other hand, adopt twisted D_2 symmetric geometries.



The N–N bond length pattern in **3'** is pronouncedly *nonequivalent* (i.e., 1.36, 1.31, 1.31 Å) whereas the corresponding bond length pattern in **7'** shows a more slight deviation from perfect *equivalence* of the six P–P bonds (i.e., 2.13, 2.12, 2.12 Å). The fact that hexazine twists away from a planar geometry has been previously associated with a mechanism to reduce the repulsion between adjacent lone pairs.^[10a-d] Likewise, the fact that hexasilabenzene (**6'**) adopts a puckered D_{3d} symmetric structure, reminiscent of a chair conformation, is related

to the *trans*-bent structure of disilene which has also been linked to a mechanism for reducing steric (Pauli) repulsion.^[10e]

Making **6'** and **7'** planar, that is, going to the corresponding *planar* optimum geometries **6** and **7**, is associated with a slight destabilization of only +3.02 and +3.66 kcal/mol, respectively. The former is a transition state for the interconversion of 2 equivalent chair conformations **6'** while the latter is a second-order saddle-point that connects 4 equivalent twisted ring structures **7'**. The planarization does not affect the essentially delocalized nature of the partial double bonds in these rings. At the contrary, under the constraint of planarity, not only **6** but now also **7** is *perfectly* D_{6h} symmetric.

The planar, D_{6h} symmetric hexazine ring **3** is +9.02 kcal/mol higher in energy than **3'**. This species is not a second-order saddle point on the potential energy surface (such as **7**) but a third-order saddle-point. Thus, it connects not only 4 equivalent twisted rings **3'** but it also has a labile (i.e., with an imaginary frequency) normal mode of B_{2u} symmetry that is associated with the localization of the partially double N–N bonds. Interestingly, this localization proceeds towards complete dissociation into 3 N₂ molecules. Thus, the propensity of **3'** to localize its N–N bonds becomes even more pronounced if this system is forced to become planar.

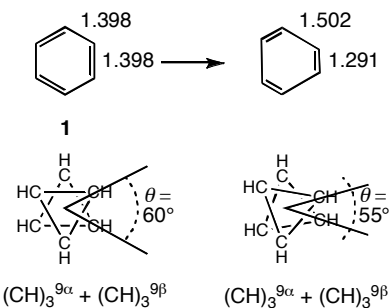
In the following, we analyze and compare the structure and bonding of **1 - 7**. The fact that all these species are planar enables us to consistently separate and study the bonding in the σ- and π-electron systems and how they change along the series of benzene and its heterocyclic and inorganic analogs.

To understand why the formally Hückel-aromatic (i.e., 4n+2 π electrons) model systems **1 - 7**, except **3**, adopt regular ring structures with delocalized double bonds and to understand why **3** localizes its multiple bonds, we have examined the energy and bonding of these species along a distortion mode proceeding from a regular delocalized structure with all bonds in the ring being equivalent towards a geometry with alternating single and double bonds. A key step in our approach is that this can be done by rotating two equivalent and geometrically frozen fragments relative to each other, as shown in Schemes 8.1 and 8.2. Such an approach was already presented for **1** in Ref. [5] (see Scheme 8.1) and is extended here to **2 - 7** (see Scheme 8.2). The advantage is that this greatly reduces the complexity of the bond analysis because we go from a multi-fragment to a two-fragment problem.

Thus, for benzene we go from D_{6h} symmetric **1** with all C–C bonds at 1.398 Å to a D_{3h} symmetric structure with alternating C–C bonds of 1.291 and 1.502 Å. This corresponds to a relative rotation of the two fragments in which the angle θ in Scheme 8.1 goes from 60° to 55°. We wish to point out that, although physically quite plausible, our choice of deformation mode, in particular the nonequilibrium *delocalized* geometry of our model system, is not unique. However, we have already previously verified for benzene that all

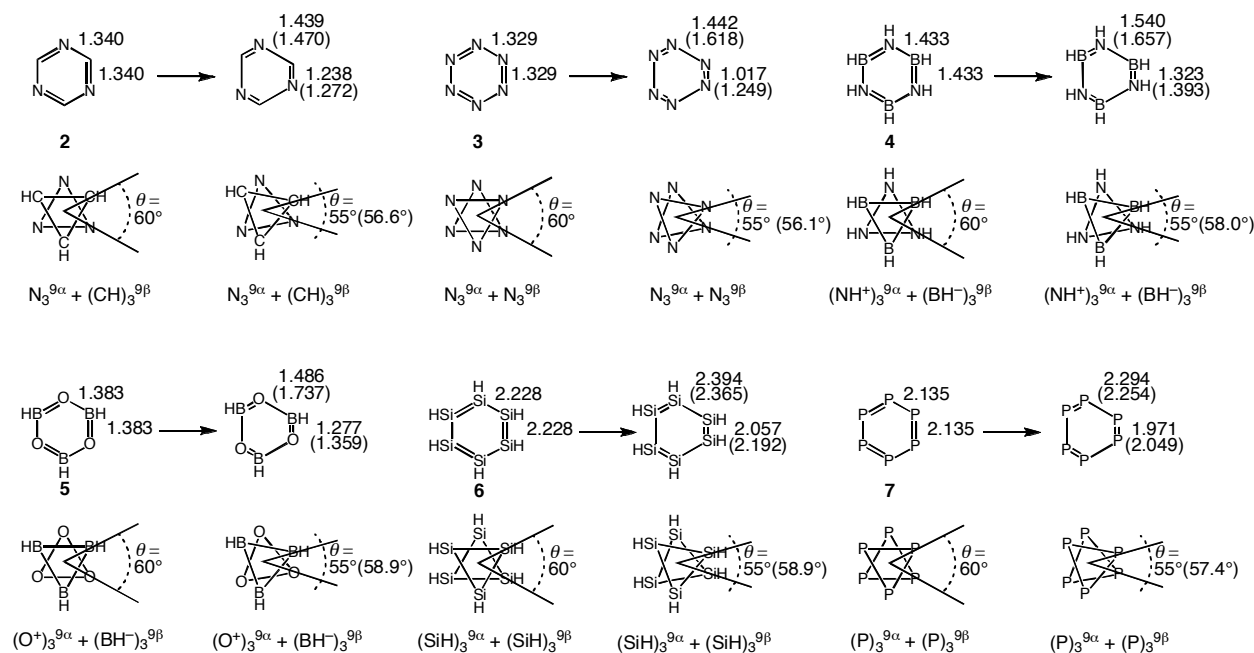
trends and conclusions that play a role in the following discussion are not affected if other plausible choices are made.^[5]

Scheme 8.1 Construction and distortion of **1** in terms of two rigid fragments.



In the present study, we have to consider an additional issue that is related to the problem of defining a consistent deformation mode. In analogy to the benzene (**1**) analysis, we have also localized all other model systems (**2 - 7**) using the localization mode in which θ in Scheme 8.2 goes from 60° to 55° . However, while this localization interval leads for benzene to a reasonable single- and double-bond length pattern, it yields in some of the other model systems to bond distances that do not well approximate regular single- and double bond lengths of the respective bonds in the ring, that is, the resulting long bonds are longer than a regular single bond and/or the short bonds are shorter than a regular double bond. The bond distances that correspond to the situation of $\theta = 55^\circ$ are shown in Scheme 8.2 without parentheses whereas the regular single- and double-bond distances (computed using a set of simple model systems)^[14] are specified *in parentheses*.

Scheme 8.2 Construction and distortion of **2 - 7** in terms of two rigid fragments.



In Figure 8.2, we have indicated the point along our localization mode at which the contracting bond reaches the regular double-bond distance with a green, dotted vertical line. The numerical value of θ at this point as well as the regular double-bond distance are shown in parentheses in Scheme 8.2. Note that we do use the full " $\theta = 60^\circ \rightarrow 55^\circ$ " localization mode in all our analyses displayed in Figures 8.1 and 8.2. One reason is the convenience of having standardized scales along the x-axes in our diagrams. A second reason is that, as can be seen in Figure 8.2, the energy effects at the point of reaching the regular double-bond distances are in some cases quite small which would require to also use different scales for the y-axes in order to make the effects graphically clear. Instead, we "amplify" the energy effects by following the full localization mode in all cases. Thus, we preserve the same x- and y-scales in all subdiagrams.

In this approach, the change in energy ΔE that goes with localizing our model systems is equal to the change in interaction energy ΔE_{int} between two geometrically frozen fragments, each in their decet valence configuration, that interpenetrate in the overall molecule. In the case of **1**, we have the fragments $(\text{CH})_3^{9\bullet} + (\text{CH})_3^{9\bullet}$ as has been described previously (see Scheme 8.1).^[5] In the other planar model systems, these fragments are $(\text{CH})_3^{9\bullet} + (\text{N})_3^{9\bullet}$ for **2**, $(\text{N})_3^{9\bullet} + (\text{N})_3^{9\bullet}$ for **3**, $(\text{BH}^-)_3^{9\bullet} + (\text{NH}^+)_3^{9\bullet}$ for **4**, $(\text{BH}^-)_3^{9\bullet} + (\text{O}^+)_3^{9\bullet}$ for **5**, $(\text{SiH})_3^{9\bullet} + (\text{SiH})_3^{9\bullet}$ for **6** and, finally, $(\text{P})_3^{9\bullet} + (\text{P})_3^{9\bullet}$ for **7** (see Scheme 8.2). The preparation energy ΔE_{prep} vanishes in this analysis because it is constant for geometrically frozen fragments. Each pair of fragments has mutually opposite spins (superscripts α and β in Schemes 8.1 and 8.2) to allow for the formation of all σ and π electron-pair bonds. Each of these fragments is a weakly (compared to the bonding interactions in **1 - 7**) repulsive conglomerate of three $\text{CH}^{9\bullet}$, $\text{N}^{9\bullet}$, $\text{BH}^{-9\bullet}$, $\text{NH}^{+9\bullet}$, $\text{O}^{+9\bullet}$, $\text{SiH}^{9\bullet}$ or $\text{P}^{9\bullet}$ radicals. The changes in interaction can be analyzed within the conceptual framework of the MO model contained in Kohn-Sham DFT by decomposing ΔE_{int} into classical electrostatic attraction (ΔV_{elstat}), Pauli repulsive orbital interactions between same-spin electrons (ΔE_{Pauli}) and the (mainly electron-pair) bonding orbital interactions (ΔE_{oi}).^[12] As pointed out in the methodological section, the latter can be symmetry decomposed into contributions from the σ and π orbital interactions: $\Delta E_{\text{oi}} = \Delta E_\sigma + \Delta E_\pi$.^[12] Thus, we have

$$\Delta E_{\text{int}} = \Delta E_{\text{Pauli}} + \Delta E_\sigma + \Delta E_\pi + \Delta V_{\text{elstat}} \quad (8.4)$$

And because in our construction of **1 - 7** the π electrons contribute no Pauli repulsion (*vide infra*), we can write

$$\Delta E_{\text{int}} = \text{"total } \sigma\text{"} + \text{"total } \pi\text{"} + \Delta V_{\text{elstat}} \quad (8.5)$$

with "total σ " = $\Delta E_{\text{Pauli}} + \Delta E_\sigma$ and "total π " = ΔE_π .

The results of our analyses, in Figures 8.1 and 8.2, show that not only in **1** (as shown previously)^[5] but also in **2 - 7**, it is the σ electrons that strive for a regular, delocalized ring structure, against the localizing propensity of the π electrons (compare blue "total σ " with red "total π " curves in Figures 8.1a and 8.2a-f). In benzene and all heterocyclic and inorganic analogs examined here, except hexazine (**3**), the σ -electron system dominates and *localization* of the *delocalized* D_{6h} and D_{3h} symmetric arrangements of **1 - 2** and **4 - 7** goes with an overall destabilization of the model system (black bold curves in Figures 8.1 - 8.2). Interestingly, the energy of D_{6h} symmetric hexazine appears to be nearly indifferent to delocalization or localization of the N–N bonds with a slight preference for the latter (see black bold curves in Figures 8.2b). In line with this result, optimization of the labile species **3** in D_{3h} symmetry, *under the constraint that the radius of the ring is kept frozen* (i.e., to 1.329 Å), yields a localized structures at −0.35 kcal/mol below **3** with alternating short and long bonds of 1.254 and 1.403 Å (we recall that without the constraint of a frozen radius, planar **3** dissociates into three N_2 molecules).

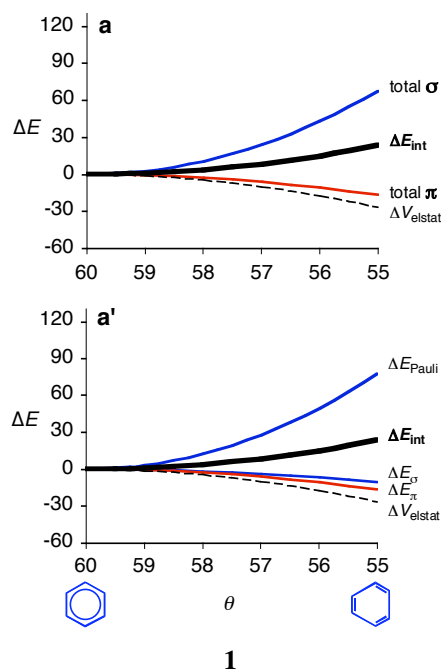


Figure 8.1 Bond energy decomposition (in kcal/mol) of **1**, constructed from two rigid fragments, as function of the distortion mode (in deg) from delocalized to localized structure as defined in Scheme 8.1.
 $\Delta E_{\text{int}} = (\Delta E_{\text{Pauli}} + \Delta E_{\sigma}) + [\Delta E_{\pi}] + \Delta V_{\text{elstat}} = (\text{total } \sigma) + [\text{total } \pi] + \Delta V_{\text{elstat}}$ computed at BP86/TZ2P.

The different propensity of the σ and π electron systems has been recently explained within the Kohn-Sham MO framework using model system **1**. The σ bonds are characterized by an equilibrium distance greater than zero, roughly 1.5 Å for C–C bonds. One reason for this is the early onset of $\langle 2p_{\sigma}|2p_{\sigma} \rangle$ compared to $\langle 2p_{\pi}|2p_{\pi} \rangle$ overlap and the fact that the

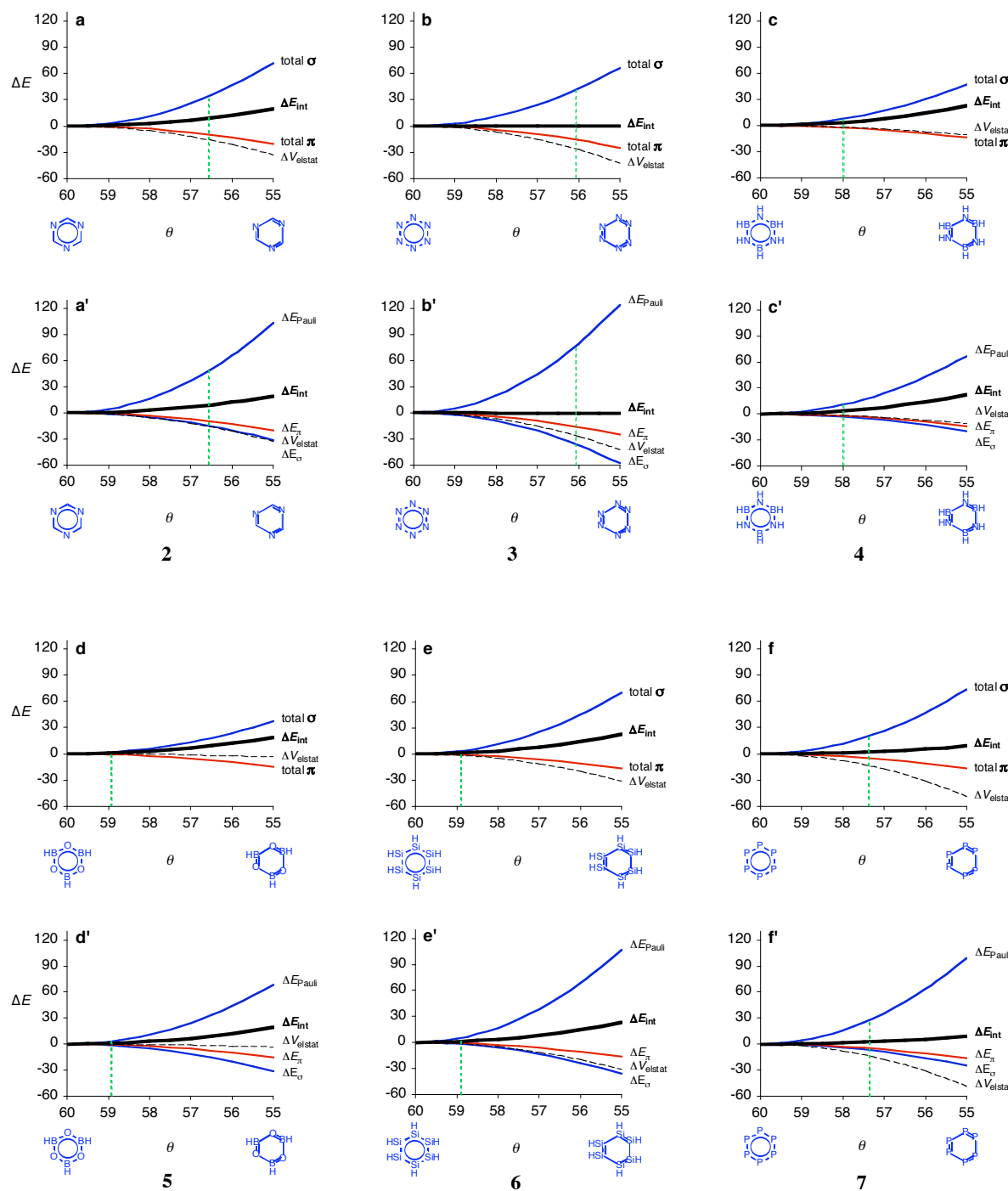
former achieves an optimum at distances greater than zero whereas the latter is maximal at distance zero (see Ref. [5] and also [15]). However, as pointed out before in a different context,^[16] the main reason for σ bonds to feature an optimum distance greater than zero is the repulsive wall provided by Pauli repulsion with the closed shell 2s (and 1s) AOs on carbon and the C–H bonds. In the symmetric, delocalized benzene, each C–C bond is already forced by partial π bonding below the optimum σ distance, i.e., it is already in the region where the Pauli repulsion ΔE_{Pauli} due to the σ electrons goes up in energy faster than the stabilizing orbital interactions ΔE_{σ} and ΔV_{elstat} together go down. This becomes clear if one separates "total σ ", shown in Figure 8.1a into its component $\Delta E_{\text{Pauli}} + \Delta E_{\sigma}$ as has been done in Figure 8.1a'.

The π -electron system, on the other hand, only provides electron-pair bonding and *no* Pauli repulsive orbital interactions. (see Ref. [5] and also Figure 6.4 in Chapter 6, left panel). Thus, at variance to the σ -electron system, it achieves an optimum overlap at zero bond distance and strives for a localization of the C–C bonds.

Here, we find that the same situation holds true also for all the heterocyclic and inorganic benzene analogs **2 - 7** studied in this work. In all cases, the delocalizing propensity of the σ electrons is more pronounced than (and thus dominates) the localizing propensity of the π electrons (compare blue "total σ " with red "total π " curves in Figures 8.1a and 8.2a-f). The fact, on the other hand, that **3** has eventually a slight bias towards localization is due to a more subtle mechanism that originates from a steep σ -orbital interaction term ΔE_{σ} , which both favor localization (compare Figure 8.2b' with Figures 8.1a' and 8.2a'-f). The steep ΔE_{σ} term can be ascribed to a later (i.e. at shorter bond distance) onset of the overlap between the more compact nitrogen orbitals. A similar behavior has also been observed for the central bond in the series of CN dimmers, which becomes both weaker (due to increasing repulsion with the nitrogen lone-pair electrons) and shorter (due to an increasingly steep σ - and π -orbital interaction term) if one goes from C–C via C–N to N–N coupling.^[12b]

Finally, one may wonder in how far the charge separation that occurs in our fragmentation of **4** into $(\text{BH}^-)_3{}^9\bullet^+$ + $(\text{NH}^+)_3{}^9\bullet^-$ and of **5** into $(\text{BH}^-)_3{}^9\bullet^+$ + $(\text{O}^+)_3{}^9\bullet^-$ affects trends and conclusions. This choice is physically inspired by the fact that it yields fragments in exactly the same valence configuration as in all the other species. Yet, to assess the robustness of our conclusions regarding this issue, we have also carried out an alternative decomposition involving the neutral fragments $(\text{BH})_3{}^6\bullet^+$ + $(\text{NH})_3{}^6\bullet^-$ for **4** and $(\text{BH})_3{}^6\bullet^+$ + $(\text{O})_3{}^6\bullet^-$ for **5**. Note that in this alternative decomposition, the three π electrons that were originally in the negatively charged fragment $(\text{BH}^-)_3{}^9\bullet^+$ have been transferred into the π orbitals that were originally singly occupied in the positively charges fragments $(\text{NH}^+)_3{}^9\bullet^-$ and $(\text{O}^+)_3{}^9\bullet^-$, respectively. Thus, the π -orbital interactions change in character from electron-pair bonding to donor-acceptor bonding. It appears that both the "regular" and "alternative" analyses yield the same trends

and that our conclusions (*vide infra*) therefore are not affected by the fact that we choose, for consistency, the "regular" decomposition (see Figure 8.2).



8.4 Conclusions

We have shown here that the MO model of aromaticity, recently developed for the archetypal aromatic molecule of benzene (**1**),^[5] is also valid for *heterocyclic* and *inorganic* benzene analogs, such as *s*-triazine (**2**), hexazine (**3'**), borazine (**4**), boroxine (**5**), hexasilabenzene (**6'**) and hexaphosphabenzene (**7'**). At variance to the other model systems studied here, **3'**, **6'** and **7'** adopt nonplanar equilibrium structures.

To facilitate a direct comparison and to enable us to separate σ and π electron bonding consistently along all species, we have included the planar species **3**, **6** and **7** into our set of model systems. In none of the cases **1** - **7** does the π -electron system favor a symmetric, delocalized ring. Instead, the regular, symmetric structure that results for all planar model systems, except **3**, is caused by the delocalizing force of the σ -electron system. Simple orbital-overlap arguments account for this behavior.

In planar hexazine (**3**), the delocalizing force of the σ -electron system is less pronounced and is therefore slightly overruled by the localizing orbital interaction in the π system. This causes D_{6h} symmetric **3** to be nearly "undecided" but yet with a slight bias towards bond localization which eventually results in barrierless formation of 3 N_2 molecules.

References

- [1] (a) P. J. Garratt, *Aromaticity*, John Wiley & Sons, Inc: New York, **1986**; (b) V. I. Minkin, M. N. Glukhotsev, B. Y. Simkin, *Aromaticity and Antiaromaticity: Electronic and Structural Aspects*, John Wiley & Sons, Inc: New York, **1994**.
- [2] (a) M. B. Smith, J. March, *March's Advanced Organic Chemistry*, 6th ed., Wiley-Interscience: New York, **2007**; (b) F. A. Carey, R. J. Sundberg, *Advanced Organic Chemistry: Structure And Mechanisms (Part A)*, Springer, New York, **2000**.
- [3] E. Hückel, *Z. Phys.* **1931**, *70*, 204.
- [4] (a) N. C. Baird, *J. Org. Chem.* **1986**, *51*, 3907; (b) E. D. Glendening, R. Faust, A. Streitwieser, K. P. C. Vollhardt, F. Weinhold, *J. Am. Chem. Soc.* **1993**, *115*, 10952.
- [5] S. C. A. H. Pierrefixe, F. M. Bickelhaupt, *Chem. Eur. J.* **2007**, *13*, 6321.
- [6] (a) P. C. Hiberty, S. S. Shaik, J. M. Lefour, G. Ohanessian, *J. Org. Chem.* **1985**, *50*, 4657; (b) S. S. Shaik, P. C. Hiberty, *J. Am. Chem. Soc.* **1985**, *107*, 3089; (c) P. C. Hiberty, S. S. Shaik, G. Ohanessian, J. M. Lefour, *J. Org. Chem.* **1986**, *51*, 3908; (d) S. S. Shaik, P. C. Hiberty, J. M. Lefour, G. Ohanessian, *J. Am. Chem. Soc.* **1987**, *109*, 363; (e) S. S. Shaik, P. C. Hiberty, G. Ohanessian, J. M. Lefour, *J. Phys. Chem.* **1988**, *92*, 5086; (f) P. C. Hiberty, D. Danovich, A. Shurki, S. Shaik, *J. Am. Chem. Soc.* **1995**, *117*, 7760; (g) A. Shurki, S. Shaik, *Angew. Chem. Int. Ed. Engl.* **1997**, *36*, 2205; (h) S. Shaik, A. Shurki, D. Danovich, P. C. Hiberty, *Chem. Rev.* **2001**, *101*, 1501.
- [7] (a) Y. Ooshika, *J. Phys. Soc. Japan* **1957**, *12*, 1238; (b) H. Labhart, *J. Chem. Phys.* **1957**, *27*, 947; (c) H. C. Longuet-Higgins, L. Salem, *Proc. R. Soc. London, A* **1959**, *251*, 172; (d) M. Tsui, S. Huzinaga, T. Hasino, *Rev. Mod. Phys.* **1960**, *32*, 425; (e) R. S. Berry, *J. Chem. Phys.* **1961**, *35*, 2253.
- [8] (a) Y. Haas, S. Zilberg, *J. Am. Chem. Soc.* **1995**, *117*, 5387; (b) E. Heilbronner, *J. Chem. Educ.* **1989**, *66*, 471; (c) A. Stanger, K. P. C. Vollhardt, *J. Org. Chem.* **1988**, *53*, 4889; (d) N. D.

- Epiotis, *Pure Appl. Chem.* **1983**, *55*, 229.; (d) F. Bickelhaupt, W. H. de Wolf, *Recl. Trav. Chim. Pays-Bas* **1988**, *107*, 459; (e) P. A. Kraakman, J.-M. Valk, H. A. G. Niederländer, D. B. E. Brouwer, F. M. Bickelhaupt, W. H. de Wolf, F. Bickelhaupt, C. H. Stam, *J. Am. Chem. Soc.* **1990**, *112*, 6638; (f) K. Jug, A. M. Koster, *J. Am. Chem. Soc.* **1990**, *112*, 6772; (g) A. Gobbi, Y. Yamaguchi, G. Frenking, H. F. Schaefer III, *Chem. Phys. Lett.* **1995**, *244*, 27; (h) P. v. R. Schleyer, H. J. Jiao, *Pure Appl. Chem.* **1996**, *68*, 209; (i) B. Kovacevic, D. Baric, Z. B. Maksic, T. Müller, *ChemPhysChem* **2004**, *5*, 1352; (j) A. Rehaman, A. Datta, S. S. Mallajosyula, S. K. Pati, *J. Chem. Theory Comput.* **2006**, *2*, 30; see also (k) A. Soncini, C. Domene, J. J. Engelberts, P. W. Fowler, A. Rassat, J. H. van Lenthe, R. W. A. Havenith, L. W. Jenneskens, *Chem. Eur. J.* **2005**, *11*, 1257; (l) J. J. Engelberts, R. W. A. Havenith, J. H. van Lenthe, L. W. Jenneskens, P. W. Fowler, *Inorg. Chem.* **2005**, *44*, 5266.
- [9] (a) Special issue on: *Aromaticity*, ed. P. v. R. Schleyer, *Chem. Rev.* **2001**, 101; (b) Special issue on: *Delocalization—pi and sigma*, ed. J. A. Gladysz, *Chem. Rev.* **2005**, 105.
- [10] (a) M. N. Glukhovtsev, H. Jiao, P. v. R. Schleyer, *Inorg. Chem.* **1996**, *35*, 7124; (b) K. K. Baldridge, O. Uzan, J. M. L. Martin, *Organometallics* **2000**, *19*, 1477; (c) J. Fabian, E. Lewars, *Can. J. Chem.* **2004**, *82*, 50; (d) P. C. Hiberty, F. Volatron, *Heteroat. Chem.* **2007**, *18*, 129; See also: (e) H. Jacobsen, T. Ziegler, *J. Am. Chem. Soc.* **1994**, *116*, 3667.
- [11] (a) G. te Velde, F. M. Bickelhaupt, E. J. Baerends, C. Fonseca Guerra, S. J. A. van Gisbergen, J. G. Snijders, T. Ziegler, *J. Comput. Chem.* **2001**, *22*, 931; (b) C. Fonseca Guerra, O. Visser, J. G. Snijders, G. te Velde, E. J. Baerends, in *Methods and Techniques for Computational Chemistry*, (Eds.: E. Clementi, G. Corongiu) STEF: Cagliari, **1995** p. 305 ; (c) E. J. Baerends, D. E. Ellis, P. Ros, *Chem. Phys.* **1973**, *2*, 41; (d) E. J. Baerends, P. Ros, *Chem. Phys.* **1975**, *8*, 412; (e) E. J. Baerends, P. Ros, *Int. J. Quantum. Chem. Symp.* **1978**, *12*, 169; (f) C. Fonseca Guerra, J. G. Snijders, G. te Velde, E. J. Baerends, *Theor. Chem. Acc.* **1998**, *99*, 391; (g) P. M. Boerrigter, G. te Velde, E. J. Baerends, *Int. J. Quantum Chem.* **1988**, *33*, 87; (h) G. te Velde, E. J. Baerends, *J. Comp. Phys.* **1992**, *99*, 84; (i) J. G. Snijders, E. J. Baerends, P. Vernooij, *At. Nucl. Data Tables* **1982**, *26*, 483; (j) J. Krijn, E. J. Baerends, *Fit-Functions in the HFS-Method; Internal Report (in Dutch)* Vrije Universiteit: Amsterdam 1984); (k) L. Versluis, T. Ziegler, *J. Chem. Phys.* **1988**, *88*, 322; (l) J. C. Slater, *Quantum Theory of Molecules and Solids*, Vol. 4, McGraw-Hill: New York, **1974** ; (m) A. D. Becke, *J. Chem. Phys.* **1986**, *84*, 4524; (n) A. Becke, *Phys. Rev. A* **1988**, *38*, 3098; (o) S. H. Vosko, L. Wilk, M. Nusair, *Can. J. Phys.* **1980**, *58*, 1200; (p) J. P. Perdew, *Phys. Rev. B* **1986**, *33*, 8822 (Erratum: *Phys. Rev. B* **1986**, *34*, 7406); (q) L. Fan, T. Ziegler, *J. Chem. Phys.* **1991**, *94*, 6057.
- [12] (a) F. M. Bickelhaupt, E. J. Baerends, in *Review in Computational Chemistry* (K. B. Lipkowitz, D. B. Boyd, Eds.), Wiley-VCH: New York, **2000**, Vol. 15, pp. 1-86. ; (b) F. M. Bickelhaupt, N. M. M. Nibbering, E. M. van Wezenbeek, E. J. Baerends, *J. Phys. Chem.* **1992**, *96*, 4864; (c) F. M. Bickelhaupt, A. Diefenbach, S. P. de Visser, L. J. de Koning, N. M. M. Nibbering, *J. Phys. Chem. A* **1998**, *102*, 9549; (d) T. Ziegler, A. Rauk, *Inorg. Chem.* **1979**, *18*, 1755; (e) T. Ziegler, A. Rauk, *Inorg. Chem.* **1979**, *18*, 1558; (f) T. Ziegler, A. Rauk, *Theor. Chim. Acta* **1977**, *46*, 1.
- [13] K. Morokuma, *Acc. Chem. Res.* **1977**, *10*, 294.
- [14] Our model systems for regular single and double bonds are: $\text{H}_3\text{C}-\text{NH}_2$ (1.470 Å), $\text{H}_2\text{C}=\text{NH}$ (1.272 Å), $\text{H}_2\text{N}-\text{NH}_2$ (1.442 Å), $\text{HN}=\text{NH}$ (1.249 Å), $\text{H}_3\text{B}-\text{NH}_3$ (1.657 Å), $\text{H}_2\text{B}=\text{NH}_2$ (1.393 Å), $\text{H}_3\text{B}-\text{OH}_2$ (1.737 Å), $\text{H}_2\text{B}=\text{OH}$ (1.395 Å), $\text{H}_3\text{Si}-\text{SiH}_3$ (2.365 Å), $\text{H}_2\text{Si}=\text{SiH}_2$ (2.192 Å), $\text{H}_2\text{P}-\text{PH}_2$ (2.254 Å) and $\text{HP}=\text{PH}$ (2.049 Å).
- [15] T. A. Albright, J. K. Burdett, M.-H. Whangbo, *Orbital Interactions in Chemistry*, John Wiley & Sons Inc: New York, **1985**.
- [16] (a) F. M. Bickelhaupt, E. J. Baerends, *Angew. Chem.* **2003**, *115*, 4315; *Angew. Chem. Int. Ed.* **2003**, *42*, 4183; (b) F. M. Bickelhaupt, R. L. DeKock, E. J. Baerends, *J. Am. Chem. Soc.* **2002**, *124*, 1500.

9 Summary

In this thesis, the fundamental chemical concepts of hypervalence and aromaticity have been investigated theoretically by means of Density Functional Theory (DFT) calculations. These two important notions deal with the propensity of a system to localize or delocalize bonds. More precisely, hypervalent and aromatic molecules usually present highly symmetrical structures with equal bonds while the geometries of non-hypervalent and antiaromatic species are asymmetric with alternating short and long bonds. The objective of the work described herein is to develop a transparent physical model that enables us to understand the nature of (non)hypervalence and (non)aromaticity. In other words, we want to understand which feature in the bonding mechanism is essential for determining whether an atom can form a hypervalent structure (or not) or whether a π -conjugated ring adopts an aromatic geometry with delocalized double bonds (or not).

This understanding is obtained from electronic structure theory by developing qualitative physical models based on Molecular Orbital (MO) theory as contained in the Kohn-Sham approach to DFT, which we employ in our DFT computations with the Amsterdam Density Functional (ADF) program.

The first two chapters of this thesis provide an introduction to the concepts of hypervalence and aromaticity and an overview of the theoretical background and DFT as well as *ab initio* methods used in this thesis. The thesis will be further separated into two parts dedicated to hypervalence and aromaticity, respectively.

Part I of this thesis deals with the concept of hypervalence. First, in Chapter 3, the capability of lithium and silicon to form hypervalent structures and the absence of such

capability for hydrogen and carbon have been investigated at the BP86/TZ2P level of density functional theory. The model systems used here to understand this issue are Li_3^- and SiH_5^- versus H_3^- and CH_5^- which, although isoelectronic to the former two species, have a distortive, bond-localizing propensity. At first we showed that the hypervalence of Li and Si does not originate from the availability of low-energy $2p$ and $3d$ AOs, respectively. Furthermore we showed that all bonding patterns of the valence molecular orbitals present 3-center-4-electron bonds in the axial X–A–X unit and are, therefore, not the key to understand the (non)hypervalence of the various central atoms studied here. Instead, we find that the discriminating factor between carbon and silicon is the smaller effective size of the former atom and the resulting lack of space around it compared to the latter. Interestingly, a similar steric mechanism is responsible for the difference in bonding capabilities between H and the effectively larger Li atom. This is so, despite the fact that the substituents in the corresponding symmetric and linear dicoordinate H_3^- and Li_3^- are on opposite sides of the central atom.

In Chapter 4, the insights on the (non)hypervalence of carbon and silicon obtained in Chapter 3 have been further developed into the Ball-in-a-Box model that accounts for the (non)hypervalence of $[\text{Cl}-\text{AH}_3-\text{Cl}]^-$ systems with A = C and Si. Similarly to CH_5^- and SiH_5^- respectively, $[\text{Cl}-\text{CH}_3-\text{Cl}]^-$ is labile, with a tendency to localize one of its axial C–Cl bonds and to largely break the other one, while the isostructural and isoelectronic $[\text{Cl}-\text{SiH}_3-\text{Cl}]^-$ forms a stable pentavalent species, with a delocalized structure featuring two equivalent Si–Cl bonds. The Ball-in-a-Box model, based on MO theory and supported by DFT calculations at the BP86/TZ2P level of theory, reveals the key role of steric factors. It further provides a simple way of understanding the above phenomena in terms of different atom sizes. In this model, the five substituents form a cage or "box" ClH_3Cl^- in which they are in mutual steric contact. The central atom A can be viewed as a "ball" in that box. Silicon fits nearly exactly into the box and can bind simultaneously to the top and the bottom. This yields the hypervalent $\text{ClSiH}_3\text{Cl}^-$ with a trigonal-bipyramidal structure. In opposition, the carbon atom is too small to touch both the top and the bottom and it can thus only bind to one of them. Consequently the carbon-atom ball "drops" onto the bottom of the box leading to a species $\text{Cl}^- \cdots \text{H}_3\text{CCl}$ with one localized C–Cl bond and one long C–Cl contact. The ball-in-a-box model is furthermore supported by the fact that the $S_{\text{N}}2$ central barrier for nucleophilic attack by Cl^- decreases monotonically along the substrates CH_3Cl , $^1\text{CH}_2\text{Cl}$, $^2\text{CHCl}$ and ^3CCl . Our findings for ClCH_3Cl^- and $\text{ClSiH}_3\text{Cl}^-$ are generalized to other group-14 central atoms (Ge, Sn and Pb) and axial substituents (F).

In Chapter 5, we have studied species that violate this ball-in-a-box behavior: although isostructural and isoelectronic with the above $[\text{X}-\text{CH}_3-\text{X}]^-$ systems, the noble gas–methyl cation complexes $[\text{Ng}-\text{CH}_3-\text{Ng}]^+$ adopt, for Ng = helium and neon, a perfectly D_{3h} symmetric structure featuring a stable hypervalent carbon atom with two equivalent C–Ng bonds. Our

analyses show that the carbon atom in $[\text{Ng}-\text{CH}_3-\text{Ng}]^+$ can no longer be considered as a ball in a box of the five substituents because it is much more tightly bound to the equatorial H atoms than to the axial noble-gas substituents. Thus, the $[\text{Ng}-\text{CH}_3-\text{Ng}]^+$ species are better conceived as a "disk between balls". Here, the "disk" is CH_3^+ and the "balls" are constituted by the two noble-gas atoms.

Finally, we propose to classify the nature of five-coordinate carbon species in terms of a spectrum between the ball-in-a-box situation (nonhypervalent C in Chapter 4) and the disk-between-balls model (hypervalent C in Chapter 5). The position along this spectrum is determined by the ratio (i.e., the relative magnitudes) of the strengths of the carbon–equatorial substituent bond ($\text{C}-\text{H}^{\text{eq}}$) versus that of the carbon–axial substituent bond ($\text{C}-\text{X}^{\text{ax}}$). Hypervalent species (like $[\text{He}-\text{CH}_3-\text{He}]^+$) have large $\text{C}-\text{H}^{\text{eq}}/\text{C}-\text{X}^{\text{ax}}$ ratios whereas truly nonhypervalent species (such as $[\text{Cl}-\text{CH}_3-\text{Cl}]^-$) have small $\text{C}-\text{H}^{\text{eq}}/\text{C}-\text{X}^{\text{ax}}$ ratios. Intermediate or "weakly nonhypervalent" cases (i.e., species with a weak tendency to localize one and to partly break the other axial carbon–substituent bond), such as $[\text{Ng}-\text{CH}_3-\text{Ng}]^+$ complexes with heavy noble-gas atoms, correspond to situations with intermediate $\text{C}-\text{H}^{\text{eq}}/\text{C}-\text{X}^{\text{ax}}$ ratios.

Part II of this thesis deals with the concept of aromaticity. First, in Chapter 6, the origin of the regular geometry of benzene as opposed to the localized geometry of 1,3-cyclobutadiene is investigated at the BP86/TZ2P level of density functional theory. Geometry is indeed one of the most direct indicators of aromaticity and antiaromaticity: a regular structure with delocalized double bonds (e.g., benzene) is symptomatic of aromaticity, whereas a distorted geometry with localized double bonds (e.g., 1,3-cyclobutadiene) is characteristic of antiaromaticity. Here, we present a molecular-orbital (MO) model of aromaticity that explains, in terms of simple orbital-overlap arguments, why this is so. Our MO model is based on accurate Kohn–Sham DFT analyses of the bonding in benzene, 1,3-cyclobutadiene and how the bonding mechanism is affected if these molecules undergo geometrical deformations between regular, delocalized ring structures, and distorted ones with localized double bonds. We show that the propensity of the π electrons is always, that is, in both the aromatic and antiaromatic molecules, to localize the double bonds, against the delocalizing force of the σ electrons. More importantly, we show that the π electrons nevertheless decide about the localization or delocalization of the double bonds by showing qualitatively different geometry dependence of the π overlap in benzene and cyclobutadiene. In the aromatic species, the localizing propensity of the π system emerges from a subtle interplay of counteracting overlap effects and is, therefore, too little pronounced to overcome the delocalizing σ system. At variance, in the antiaromatic ring, all π -overlap effects unidirectionally favor localization of the double bonds and can, in this way, overrule the σ system.

In Chapter 7, we show that the MO model of (anti)aromaticity that we presented for cyclobutadiene and benzene in Chapter 6 extends also to the corresponding next larger analogs, cyclooctatetraene (C_8H_8) and cyclodecapentaene ($C_{10}H_{10}$), respectively. Our MO model accounts for the antiaromaticity of C_8H_8 and the only very weakly aromatic nature of $C_{10}H_{10}$. Thus, in none of the cases does the π -electron system favor a symmetric, delocalized ring. The regular, symmetric structure of benzene has the same cause as that of cyclohexane, namely, the σ -electron system. Nevertheless, the π system decides if delocalization occurs by showing qualitatively different geometry-dependence of the π overlap in the aromatic (C_6H_6 and $C_{10}H_{10}$) versus the antiaromatic rings (C_4H_4 and C_8H_8). In the latter two, all π -overlap effects unidirectionally favor localization of the double bonds and can, in this way, overrule the σ system. The somewhat more pronounced steric repulsion between vicinal C–H bonds in planar C_8H_8 causes cyclooctatetraene to adopt the nonplanar, tub-shaped equilibrium conformation in which this steric repulsion is reduced around C–C single bonds. In the aromatic species, the localizing propensity of the π system emerges from a subtle interplay of counteracting overlap effects. In benzene, it is therefore too little pronounced to overcome the delocalizing σ system. In cyclodecapentaene, the π system shows a somewhat increased localizing propensity but, in our BP86 calculations, this is still not strong enough to overcome the delocalizing σ system. Therefore, we arrive at a delocalized structure which, however, adopts a nonplanar, saddle-shaped conformation to minimize the steric repulsion between vicinal C–H bonds. Our electronic structure analyses nicely confirm that the π -electron system of cyclodecapentaene causes the aromatic character of this species to be much reduced if compared to benzene.

Finally, we have shown in Chapter 8 that the MO model of aromaticity, recently developed for the archetypal aromatic molecule of benzene, is also valid for *heterocyclic* and *inorganic* benzene analogs, such as *s*-triazine, hexazine, borazine, boroxine, hexasilabenzene and hexaphosphabenzene. At variance to the other model systems studied here, hexazine, hexasilabenzene and hexaphosphabenzene adopt nonplanar equilibrium structures. To facilitate a direct comparison and to enable us to separate σ and π electron bonding consistently along all species, we have included the planar species hexazine, hexasilabenzene and hexaphosphabenzene into our set of model systems. In none of the cases does the π -electron system favor a symmetric, delocalized ring. Instead, the regular, symmetric structure that results for all planar model systems, except hexazine, is caused by the delocalizing force of the σ -electron system. Simple orbital-overlap arguments account for this behavior.

In planar hexazine, the delocalizing force of the σ -electron system is less pronounced and is therefore slightly overruled by the localizing orbital interaction in the π system. This causes D_{6h} symmetric hexazine to be nearly "undecided" but yet with a slight bias towards bond localization which eventually results in barrierless formation of 3 N_2 molecules.

As a concluding remark, the work carried out in this thesis allows Molecular Orbital (MO) theory to catch up with Valence Bond (VB) theory regarding the treatment and understanding of the phenomenon of hypervalence and aromaticity. It also nicely shows how the interplay of electronic and steric factors plays a role in the question if an atom has the capability to form stable hypervalent structures with its substituents while the question of whether a species is aromatic or antiaromatic is a purely electronic problem.

10 Samenvatting

In dit proefschrift wordt verslag gedaan van theoretisch chemisch onderzoek aan de fundamentele concepten van hypervalentie en aromaticiteit, onder gebruikmaking van de dichtheidsfunctionaal-theorie (DFT). Deze beide concepten hebben betrekking op de neiging van een systeem om zijn bindingen te localiseren dan wel te delocaliseren. Hypervalente en aromatische moleculen hebben in het algemeen een hoogsymmetrische structuur met equivalente bindingen terwijl niet-hypervalente en anti-aromatische moleculen asymmetrisch zijn met elkaar afwisselend, korte en lange bindingen. Het doel van dit promotie-onderzoek is het ontwikkelen van een helder fysisch model, dat ons in staat stelt om de aard en oorsprong van (niet-)hypervalentie en (anti-)aromaticiteit te *begrijpen*. Met andere woorden, wij willen begrijpen welk fenomeen er in het bindingsmechanisme verantwoordelijk voor is, of een atoom al dan niet een hypervalente structuur kan vormen en of een π -geconjugeerde ring wel of niet een aromatische structuur aanneemt met gedelocaliseerde dubbele bindingen.

Het gewenste inzicht wordt hier, uitgaande van het Kohn-Sham molecuul-orbitaal (MO) model, verkregen door analyses van de electronische structuur op basis van DFT-berekeningen met het Amsterdam-Density-Functional (ADF) programma.

De eerste twee hoofdstukken van dit proefschrift omvatten een algemene inleiding in het onderzoeksgebied van hypervalentie en aromaticiteit alsmede een overzicht van gebruikte theoretische methoden en technieken (DFT en ab-initio). Het proefschrift is voorts opgesplitst in twee delen die gewijd zijn aan respectievelijk hypervalentie en aromaticiteit.

Deel I van het proefschrift behandelt hypervalentie. Eerst wordt in hoofdstuk 3 op het BP86/TZ2P-niveau onderzocht waarom lithium en silicium hypervalente structuren kunnen vormen terwijl waterstof en koolstof deze eigenschap missen. De hiervoor gebruikte

modelsystemen zijn de hypervalente Li_3^- en SiH_5^- versus de isoelectronische maar niet-hypervalente H_3^- respectievelijk CH_5^- . De hypervalentie van Li en Si blijkt geen verband te houden met beschikbaar zijn van laag-energetische AO's, $2p$ en $3d$ respectievelijk. Verder is er geen verschil tussen de vier modelsystemen aangaande hun voornaamste bindingsmechanisme langs de X–A–X hoofdas. Dit wordt in alle gevallen verzorgd door een 3-center-4-electron-binding en bevat dus niet de sleutel voor een verklaring van het verschil in bindingsmogelijkheden tussen Li en Si versus H en C. Het onderscheid tussen koolstof en silicium, zo blijkt uit onze analyses, wordt daarentegen veroorzaakt door de kleinere effectieve grootte van eerst genoemde en het daarmee gepaard gaande gebrek aan ruimte daaromheen in vergelijking met silicium. Interessant genoeg is een soortgelijk sterisch mechanisme verantwoordelijk voor het verschil in bindingsgedrag tussen H en het effectief grotere Li-atoom. Dit is zo ondanks het feit dat zich de beide substituenten in de overeenkomstige symmetrische en lineaire, tweevoudig gecoördineerde H_3^- en Li_3^- aan weerszijden van het centrale atoom bevinden.

In hoofdstuk 4 worden de hierboven beschreven inzichten in het wel of niet hypervalent zijn van koolstof en silicium verder ontwikkeld tot het "Ball-in-a-Box" ("bol-in-een-doos") model dat de (niet-)hypervalentie van $[\text{Cl}-\text{AH}_3-\text{Cl}]^-$ systemen met A = C en Si beschrijft en verklaart. Analoog aan CH_5^- en SiH_5^- is $[\text{Cl}-\text{CH}_3-\text{Cl}]^-$ labiel met de neiging om één van zijn axiale C–Cl-bindingen te verkorten en de andere grotendeels te verbreken, terwijl het isostructurale en isoelectronische $[\text{Cl}-\text{SiH}_3-\text{Cl}]^-$ een stabiel, pentavalent systeem vormt met een gedelocaliseerde structuur die door twee equivalenten Si–Cl-bindingen gekarakteriseerd wordt. Het Ball-in-a-Box model stoelt op MO-theorie en BP86/TZ2P DFT-berekeningen en onthult de sleutelrol van sterische factoren. Het stelt ons in staat bovenstaande fenomenen gemakkelijk te begrijpen in termen van de verschillen in grootte tussen de atomen. In dit model vormen de vijf substituenten een kooi of "doos" ClH_3Cl^- waarin zij onderling in sterisch contact zijn. Het centrale atoom A kan nu opgevat worden als een "bol" in deze doos. Silicium past vrijwel exact in de doos en kan tegelijkertijd met het "deksel" en de "bodem" wisselwerken. Dit levert het hypervalente $\text{ClSiH}_3\text{Cl}^-$ op met een trigonaal-bipiramidale structuur. In tegenstelling hiertoe is koolstof te klein om tegelijkertijd tegen de bodem en het deksel aan te zitten: koolstof kan dus alleen aan één van beide binden. Dientengevolge "valt" het koolstofatoom op de bodem van de doos hetgeen tot het asymmetrische $\text{Cl}^- \cdots \text{H}_3\text{CCl}$ leidt met één gelocaliseerde C–Cl-binding en een lang C–Cl-contact. Het ball-in-a-box model wordt ook ondersteund door het feit dat de centrale barrière voor de $\text{S}_{\text{N}}2$ -reactie van het nucleofiel Cl^- daalt langs de reeks van substraten CH_3Cl , $^1\text{CH}_2\text{Cl}$, $^2\text{CHCl}$ en ^3CCl . We hebben onze resultaten voor ClCH_3Cl^- en $\text{ClSiH}_3\text{Cl}^-$ verder gegeneraliseerd naar andere centrale atomen uit groep 14 (Ge, Sn en Pb) en naar andere axiale substituenten (F).

In hoofdstuk 5 hebben wij systemen bestudeerd die de door het ball-in-a-box-model voorspelde "gedragsregels" overtreden: hoewel zij isostructuureel en isoelectronisch met

bovenstaande $[X-CH_3-X]^-$ systemen zijn, nemen de edelgas-methylkation-complexen $[Ng-CH_3-Ng]^+$ voor Ng = helium en neon een volmaakt D_{3h} -symmetrische structuur aan met daarin een stabiel, hypervalent koolstofatoom dat twee gelijkwaardige C–Ng-bindingen vormt. Onze analyses tonen aan dat het koolstofatoom in $[Ng-CH_3-Ng]^+$ niet langer als een bol in een doos bestaande uit vijf substituenten beschouwd kan worden, omdat het veel sterker aan de equatoriale H-atomen bindt dan aan de axiale edelgas-substituenten. Het $[Ng-CH_3-Ng]^+$ systeem kan in wezen beter opgevat worden als een "disk between balls" ("schijf-tussen-bollen"). Hierbij wordt de schijf gegeven door CH_3^+ en stellen de twee edelgas-atomen de twee bollen voor.

Tenslotte stellen wij voor om systemen met vijfvoudig gecoördineerd koolstof te classificeren aan de hand van een spectrum dat van de ball-in-a-box-situatie aan het ene uiteinde (niet-hypervalente C in hoofdstuk 4) naar het disk-between-balls-model aan het andere uiteinde loopt (hypervalente C in hoofdstuk 5). De positie van een systeem in dit spectrum wordt bepaald door de verhouding tussen (d.w.z., de relatieve grootte van) de sterkte van de koolstof-equatoriale-substituent binding ($C-H^{eq}$) versus die van de koolstof-axiale-substituent binding ($C-X^{ax}$). Hypervalente systemen (zoals $[He-CH_3-He]^+$) hebben grote $C-H^{eq}/C-X^{ax}$ -verhoudingen terwijl echte niet-hypervalente systemen (zoals $[Cl-CH_3-Cl]^-$) kleine $C-H^{eq}/C-X^{ax}$ -verhoudingen hebben. Tussenliggende "zwak niet-hypervalente" gevallen (d.w.z., systemen met een zwakken neiging om één van de axiale koolstof-substituent bindingen te localiseren en de andere gedeeltelijk te verbreken), zoals de $[Ng-CH_3-Ng]^+$ -complexen met de zwaardere edelgasatomen, komen overeen met moderate $C-H^{eq}/C-X^{ax}$ -verhoudingen.

Deel II van dit proefschrift gaat over het concept aromaticiteit. In hoofdstuk 6 wordt eerst de oorsprong van de regelmatige geometrie van benzeen en de gelocaliseerde geometrie van 1,3-cyclobutadiëen onderzocht op het BP86/TZ2P-niveau van DFT. De structuur is één van de hoofdindicatoren voor aromaticiteit en anti-aromaticiteit: een regelmatige structuur met gedelocaliseerde dubbele bindingen (bijv. benzeen) is typerend voor aromaticiteit, terwijl een vervormde geometrie met gelocaliseerde dubbele bindingen (bijv. 1,3-cyclobutadiëen) karakteristiek is voor anti-aromaticiteit. Hier wordt een MO-model van aromaticiteit voorgesteld, dat in termen van eenvoudige overlap-argumenten verklaart, waarom dit zo is. Ons MO-model is gebaseerd op nauwkeurige Kohn-Sham-DFT-analyses van de bindingsmechanismen in benzeen en 1,3-cyclobutadiëen en hoe deze afhangen van een geometrische vervorming van deze moleculen van een regelmatige, gedelocaliseerde ringstructuur naar ringen met gelocaliseerde dubbele bindingen. Wij tonen aan dat de π -electronen altijd, dus zowel in aromatische als anti-aromatische systemen, de neiging hebben om dubbele bindingen te *localiseren*, tegen de delocaliserende kracht van de σ -electronen in.

Een cruciaal punt is dat de π -electronen desondanks de beslissende factor zijn met betrekking tot de vraag of een structuur haar dubbele bindingen wel of niet localiseert. Dit volgt uit een kwalitatief verschillende geometrie-afhankelijkheid van de π -overlap in benzeen en cyclobutadiëen. In aromatische moleculen komt de localiserende neiging van het π -systeem voort uit een subtiel samenspel van elkaar tegenwerkende overlap-effecten. De localiserende kracht van het π -systeem is hierdoor te zwak om het delocaliserende σ -systeem te overheersen. Daarentegen werken in de anti-aromatische ring alle π -overlap-effecten in dezelfde richting, waardoor een sterke tendens tot localisatie van de dubbele bindingen ontstaat. Hierdoor is de localiserende kracht van het π -systeem in een anti-aromatische ring sterk genoeg om het σ -systeem te overheersen.

In hoofdstuk 7 laten wij zien dat het in hoofdstuk 6 voor cyclobutadiëen en benzeen ontwikkelde MO-model ook van toepassing is op de grotere analoga, het anti-aromatische cyclooctatetraëen (C_8H_8) respectievelijk het zwak aromatische cyclodecapentaëen ($C_{10}H_{10}$). In geen van de gevallen streeft het π -systeem naar een regelmatige, gedelocaliseerde ringstructuur. Zo'n symmetrische structuur met equivalentie C–C bindingen heeft dezelfde oorzaak als in het geval van cyclohexaan, namelijk het σ -electronen-systeem. Desondanks bepaalt het π -systeem of er sprake is van delocalisatie door het al eerder genoemde kwalitatieve verschil in geometrie-afhankelijkheid van de π -overlap in de aromatische (C_6H_6 and $C_{10}H_{10}$) versus de anti-aromatische ringen (C_4H_4 and C_8H_8). In de twee laatst genoemde gevallen, werken alle π -overlap-effecten in dezelfde richting en zijn sterk genoeg om het delocaliserende σ -systeem te overheersen. De gebogen, niet-vlakke geometrie van cyclooctatetraëen is het gevolg van een iets sterkere sterische repulsie tussen aangrenzende C–H bindingen. In de aromatische ringen, komt de localiserende werking van het π -systeem weer voort uit een subtiel samenspel van elkaar tegenwerkende overlap-effecten en is hierdoor te zwak om het delocaliserende σ -systeem te overheersen. In cyclodecapentaëen is de localiserende kracht van het π -systeem iets groter dan in benzeen maar deze is, in onze BP86-berekeningen, nog niet toereikend om het delocaliserende σ -systeem te overheersen. Het resultaat is een gedelocaliseerde structuur die echter een niet-vlakke, zadelvormige conformatie aanneemt om sterische repulsie tussen aangrenzende C–H-bindingen te minimaliseren. Onze analyses van de electronische structuur bevestigen dus de afname van het aromatische karakter van het π -systeem in cyclodecapentaëen vergeleken met benzeen.

In hoofdstuk 8 laten wij verder zien dat ons MO-model voor aromaticiteit niet alleen voor het archetypische, organische benzeen molecuul geldt, maar ook voor *heterocyclische* en *anorganische* benzeen-analogen, zoals *s*-triazine, hexazine, borazine, boroxine, hexasilabenzeen en hexafosfabenzeen. Hexazine, hexasilabenzeen en hexafosfabenzeen nemen hierbij, anders dan de overige modelsystemen, een niet-vlakke evenwichtsstructuur aan. We hebben in onze studie ook de vlakke conformaties van hexazine, hexasilabenzeen en hexafosfabenzeen opgenomen om zodoende een directe vergelijking alsmede een consistente

scheiding van σ - en π -bindingsmechanismen voor alle modelsystemen mogelijk te maken. Het π -electronen-systeem begunstigt in geen van de gevallen een symmetrische, gedelocaliseerde ring. De regelmatige, symmetrische structuur die wij voor alle modelsystemen behalve hexazine vinden wordt daarentegen veroorzaakt door de delocaliserende kracht van het σ -electronen-system. In vlak hexazine is de delocaliserende werking van het σ -systeem minder uitgesproken, waardoor deze door het localiserende π -systeem overheerst kan worden. Hierdoor is D_{6h} -symmetrisch hexazine praktisch "onbeslist" maar met een lichte voorkeur voor localisatie, welke uiteindelijk in barrièreloze vorming van 3 N₂ moleculen resulteert.

Tenslotte zorgt het hier beschreven promotie-onderzoek ervoor dat de molecuul-orbitaal (MO) theorie een voorheen ten opzichte van de valence-bond (VB) theorie bestaande achterstand inhaalt met betrekking tot de beschrijving en verklaring van de fenomenen hypervalentie en aromaticiteit. Dit onderzoek beklemtoont ook hoe het samenspel van electronische en sterische factoren bepalend is voor de vraag of een atoom stabiele, hypervalente structuren kan vormen, terwijl de vraag of een molecuul aromatisch dan wel anti-aromatisch is in eerste aanleg een electronisch probleem is.

Acknowledgements / Dankwoord / Remerciements

Alleerst wil ik mijn co-supervisor, Matthias Bickelhaupt, bedanken. It was such a great opportunity for me to do my PhD under your supervision. The last four years have been positive in many ways and the resulting thesis is a big achievement for me. Thanks for your help and for sharing your experience and knowledge with me. Further thanks for spending time with me whenever I had questions or problems. Hartelijk dank!

I also want to thank Prof. Baerends for the nice way he leads the theoretical chemistry group at the Vrije Universiteit. Your kindness, experience and availability have been greatly appreciated in the last four years. Furthermore, your influence has augmented the clarity of the message in some chapters of my thesis.

Moreover, I would like to thank everybody from the TC group who spends some time at the VU while I was doing my PhD. First Marc and Marcello, my “crew” from the room R-130 from the beginning on until the end. We had great conversations together and it was really good to share the office with you for four years. Special dedication to Marc for the music, the concerts, the discussions, New York, the cultural and political Dutch lessons, the bowling and so many others things... I am glad I met you. We often shared similar problems during our PhD and it was somehow easier to face them together. Hartelijk dank en groeten aan Floor en Tammi. En weet je: Better Must Come! Special thanks to Marcello for the cover, for the music as well, and many other things. Greeting to Cristina and Matteo Martino as well.

Then I would like to thank Willem-Jan for sharing his experience of the alternative music scene of Amsterdam and of the Netherlands. Thanks also for the parties in Uilenstede, for dropping by in our office every now and then to play with our cardboard tube and for your help as well. Hail to Dr. Peanut Butter and to the Juggling Chemist. Patricia, it was really nice to get to know you and to have you in the group. You always helped a lot with every event we organized at my place. I will miss you at my next poster session. I also want to thank Matthias’ subgroup (past and present) for help and interesting (and sometimes vigorous) discussions: Marcel, Jordi, Theodoor, Célia and Tushar. Marcel helped me quite a lot with issues regarding ADF, the shell environment and computers in general. Thanks a lot for this. Regarding computer staff, I also have to thank actual and past members of the TC group.

Drew McCormack, Peter Vassilev and Johannes Neugebauer helped me whenever they could and I am grateful for this. The SCM people (Stan, Olivier, Erik and Alexei) helped me as well regarding ADF issues and I hope they will be as efficient as they used to be with my ADF problems when I leave the TC group.

There are still a lot of people to thank. For example, I like to thank Ivan and the van Stralen brothers for the good time we had together in the group. I was really nice to meet you guys! Next time you guys come to Spain, give me a call. The same holds for Andre and Klass. It was really nice to discuss with you about everything and nothing at the same time. Daniel also has to be thanked for being more than a colleague, a neighbor or a roommate during the last four years. We did quite a lot of things together like going to Germany (Berlin, Kassel, Regensburg, Marburg) or to my parents' place in Brittany. And many more in The Netherlands. Finally I would like to thank all the people that were at the VU during my PhD: Paul (keep drumming!), Filippo (France will beat Italy this time, you know!), Pier (and the Jazz or No orchestra), Oleg (for the polar lights), Kasia and Tomack (for the nice evenings we had together), Paola (for sharing a while our office), Lisette (pour son sourire le matin) and Kitty (nice party in Scheveningen). I also thank Luuk and his sub-group: Andreas, Rosa (nice Boston experience), Maya (Wax Tailor), Christoph (nice advices on the thesis) and Jetze (alias Robbie). A word for the guests of the group: David (Girona), Carlos (Barcelona), Paola (Perrugia), Marcin (Poland), Emmanuel (Toulouse) and the many more I forgot to mention here. At last, I would like to thank the secretaries of the TC group: Paula, Nanda and Manuel. You helped me a lot during the last four years and were always available when needed. Special thanks to Paula who organized almost everything when I started my PhD in the Netherlands.

Pour la fin, le meilleur évidemment! D'abord Soizic qui m'a soutenu tout au long de ces, parfois longues, quatre années. Merci de m'avoir supporté, même quand j'étais ronchon! Il y aurait tellement d'autres choses pour lesquelles je pourrais te remercier... Maintenant cap sur l'Espagne et on passe à autre chose. Il est temps! Merci aussi à mes parents et à Rosy qui ont le plus ressenti les périodes les moins drôles. Merci pour votre soutien dans cette expérience. Merci bien sûr à tout le reste de ma famille: mémé et Jean-Luc, Tristan, Mylou, Sophie qui est maman maintenant, et à tous les autres en Charente, Creuse ou du côté de Toulouse. Une pensée aussi pour la famille Grimault. Merci aux nombreux amis bretons, de France ou d'ailleurs d'être venus donner des coups de niacque. Ca m'a fait vraiment plaisir de vous voir ici et de pouvoir vous montrer où j'ai habité pendant quatre ans. Un gros bisous à Arnaud, notre coloc préféré (merci pour tout, la liste est trop longue, tu dois encore l'avoir en mail) et à Daphné. Dikke kusje aan Job en Martine, Michiel en Paulina voor de borrels, de avondeten en de feestjes. Tenslotte hail to Snars: keep rocking. Rendez-vous à tous en Espagne.

List of Publications

1) S. C. A. H. Pierrefixe, F. M. Bickelhaupt

Hypervalence and the Delocalizing versus Localizing Propensities of H_3^- , Li_3^- , CH_5^- and SiH_5^-

Struct. Chem. **2007**, *18*, 813.

2) S. C. A. H. Pierrefixe, C. Fonseca Guerra, F. M. Bickelhaupt

Hypervalent Carbon versus Silicon: Ball-in-a-Box Model

Chem. Eur. J. **2007**, *14*, 819.

3) S. C. A. H. Pierrefixe, J. Poater, C. Im, F. M. Bickelhaupt

Hypervalent versus Nonhypervalent Carbon in Noble-Gas Complexes

Chem. Eur. J. **2008**, Accepted

4) S. C. A. H. Pierrefixe, F. M. Bickelhaupt

Aromaticity. Molecular Orbital Picture of an Intuitive Concept

Chem. Eur. J. **2007**, *13*, 6321.

5) S. C. A. H. Pierrefixe, F. M. Bickelhaupt

Aromaticity and Antiaromaticity in 4-, 6-, 8- and 10-Membered Conjugated Hydrocarbon Rings

J. Phys. Chem. A. **2008**, Accepted

6) S. C. A. H. Pierrefixe, F. M. Bickelhaupt

Aromaticity in Heterocyclic and Inorganic Benzene Analogs

Aust. J. Chem. **2008**, *61*, 209